DISS. ETH NO. 24650

SPATIAL PROPAGATION OF LANDSLIDE GENERATED IMPULSE WAVES

A thesis submitted to attain the degree of

DOCTOR OF SCIENCES of ETH ZURICH

(Dr. sc. ETH Zurich)

presented by:

FREDERIC MARTIN EVERS

Dipl.-Ing., Karlsruhe Institute of Technology

born on 31.10.1983

citizen of Germany

accepted on the recommendation of

Prof. Dr. Robert M. Boes

Em. Prof. Dr. Willi H. Hager

Prof. Dr. Valentin Heller

Prof. Dr. Marcello Di Risio

2017

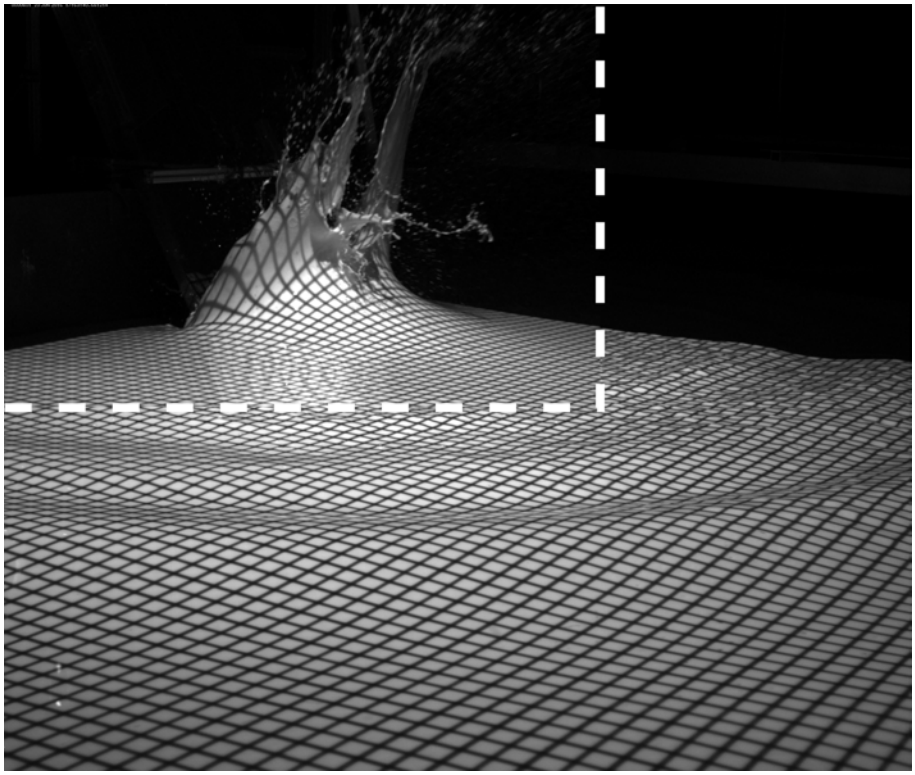

Spatial impulse wave (Evers 2017)

Acknowledgements

This doctoral thesis was written at the Laboratory of Hydraulics, Hydrology and Glaciology (VAW) at ETH Zurich. The project was funded by the Swiss National Science Foundation (No. 200021-143657). I owe personal thanks to:

- Em. Prof. Dr. Willi H. Hager, ETH Zurich, for his constant support and for allowing me latitude in the realization of this work as well as for sharing with me his profound knowledge on hydraulics, hydraulicians and various other topics.
- Prof. Dr. Robert M. Boes, ETH Zurich, for prominently promoting impulse wave research at VAW, his keen interest in putting theory into practice, and his detailed review of this work.
- Prof. Dr. Valentin Heller, University of Nottingham, whose research on impulse waves is an invaluable foundation of this work, for acting as an external reviewer.
- Prof. Dr. Marcello Di Risio, Università degli Studi dell'Aquila, for acting as an external reviewer.
- Dr. Helge Fuchs, ETH Zurich, for his share in the preparatory arrangements of this work and for being a sparring partner in terms of impulse waves and beyond.
- My fellow colleagues at VAW for the agreeable cooperation, their craftsmanship, the *Znüni* sharing, their cooking skills, the *Apéros*, and the great time so far.
- Dr. Pierre-Jacques Frank not only for introducing me to videometry but also for his good spirits, his friendship and the privilege of having mastered another phase of life together with him.
- My family, my friends and especially Natascha for providing me with very welcome distraction.

Zürich, December 2017 Frederic M. Evers

Abstract

Extremely rapid subaerial mass movements such as landslides or avalanches may generate large waves in inland waters including lakes and reservoirs as well as in coastal areas. These waves are referred to as impulse waves and feature characteristics similar to tsunamis upon reaching the shore or a dam structure. One of the most prominent events occurred in 1958 at Lituya Bay, USA, where an earthquake-triggered rockslide generated an impulse wave train reaching runup heights of more than 500 m. But also smaller events pose a hazard to adjacent settlements and infrastructure. For assessing hazards related to impulse waves, it is important to predict key wave characteristics, e.g. wave amplitudes, based on the slide impact parameters.

The main focus of this study is on the spatial impulse wave propagation, i.e. the waves spread omni-directionally from the slide impact location. Hydraulic experiments were conducted according to the Froude similitude in a 4.5 m by 8 m wave basin (3D) equipped with a videometric measurement system for tracking the free water surface. Mesh-packed granular slides were applied for generating the impulse waves. This simplified approach to reproduce impulse wave characteristics similar to those generated by free granular slides was previously confirmed in 42 wave channel (2D) experiments. The parameters varied for the subsequent 74 3D experiments include the slide impact velocity, the slide mass, the slide thickness, the slide width, the slide impact angle, and the still water depth. Except for the slide width, all of these parameters are also included in the impulse product parameter P introduced by Heller (2008) as the governing parameter for 2D impulse wave generation.

The videometric measurement technique yields a quasi-continuous representation of the free water surface allowing for the adaptive detection of the slide impact zone extent represented by the impact radius r_0. At the impact radius and beyond, the wave characteristics are governed by the impulse product parameter P, including the slide impact velocity, thickness, mass, and impact angle, as a quantity for the 2D momentum transfer to the water column per unit slide width, as well as the slide width b and again the slide impact angle α as additional 3D slide parameters. Empirical fit equations are presented for the first wave crest and trough amplitudes, the second wave crest amplitude, the first wave height, the first wave period, and the first and second wave crest celerities. The equation layout allows for a comprehensive description of the spatial wave amplitude evolution, integrating the maximum wave amplitude at the impact radius, an exponential function for the wave decay process, and a hyperbolic secant function for the crest and trough shapes for wave propagation angles between 0° and 90°.

A computational example demonstrates the applicability of the novel equations for hazard assessment. In combination with existing runup equations, the equations were further applied to the impulse wave event in 2007 at Chehalis Lake. This case study reveals a good agreement with the measured field data and provides a first validation of the experimental results at prototype scale.

Kurzfassung

Subaerische Massenbewegungen mit hohen Geschwindigkeiten wie Bergstürze oder Lawinen können sowohl in Binnengewässern wie Seen und Speicherbecken als auch in Küstengebieten hohe Wellen erzeugen. Diese Wellen werden als Impulswellen bezeichnet und weisen ähnliche Eigenschaften wie Tsunamis auf, wenn sie das Ufer oder eine Dammstruktur erreichen. Eines der bekanntesten Ereignisse ereignete sich 1958 in Lituya Bay, USA, wo ein durch ein Erdbeben ausgelöster Bergsturz einen Impulswellenzug mit einer Auflaufhöhe von mehr als 500 m erzeugte. Aber auch kleinere Ereignisse stellen eine Gefahr für angrenzende Siedlungen und Infrastrukturen dar. Für die Beurteilung von Gefahren im Zusammenhang mit Impulswellen ist es entscheidend, wichtige Welleneigenschaften, wie z.B. Wellenamplituden, auf der Grundlage der Rutscheintauchparameter vorherzusagen.

Das Hauptaugenmerk dieser Arbeit liegt auf der räumlichen Ausbreitung von Impulswellen, d.h. die Wellen breiten sich omnidirektional von der Rutscheintauchstelle aus. Hydraulische Laborversuche wurden entsprechend der Froude-Ähnlichkeit in einem 4.5 m $\times$ 8 m grossen Wellenbecken (3D) durchgeführt, welches mit einem videometrischen Messsystem zur Erfassung der freien Wasseroberfläche ausgestattet ist. Zur Erzeugung der Impulswellen wurden im Netzbeutel gebundene granulare Rutsche eingesetzt. Dieser vereinfachte Ansatz zur Nachbildung von Impulswelleneigenschaften, ähnlich denen, die von freien granularen Rutschen erzeugt werden, wurde zuvor in 42 Wellenkanalexperimenten (2D) bestätigt. Die Parameter, die für die daran anschliessenden 74 3D-Experimente variiert wurden, umfassen die Rutscheintauchgeschwindigkeit, die Rutschmasse, die Rutschmächtigkeit, die Rutschbreite, den Rutscheintauchwinkel und die Ruhewassertiefe. Mit Ausnahme der Rutschbreite sind alle diese Parameter auch in dem von Heller (2008) eingeführten, für die 2D-Impulswellengenerierung massgeblichen Impulsproduktparameter P enthalten.

Das videometrische Messverfahren liefert ein quasi-kontinuierliches Abbild der freien Wasseroberfläche und ermöglichte damit eine adaptive Erfassung der Ausdehnung der Rutscheintauchzone, die durch den Eintauchradius r_0 definiert wird. Dort und darüber hinaus werden die Welleneigenschaften durch den Impulsproduktparameter P, welcher die Eintauchgeschwindigkeit, Mächtigkeit, Masse und Eintauchwinkel des Rutsches einschliesst und den 2D-Impulstransfer auf die Wassersäule pro Rutschbreiteneinheit beschreibt, sowie die Rutschbreite b und nochmals den Rutscheintauchwinkel α als zusätzliche 3D-Rutschparameter bestimmt. Empirische Anpassungsgleichungen werden für die Amplituden des ersten Wellenbergs und -tals, die Amplituden des zweiten Wellenbergs, die erste Wellenhöhe, die erste Wellenperiode und die Ausbreitungsgeschwindigkeiten des ersten und zweiten Wellenbergs vorgestellt. Der Gleichungsaufbau ermöglicht eine umfassende Beschreibung der räumlichen Entwicklung der Wellenamplituden, wobei die maximale Wellenamplitude am Eintauchradius, eine Exponentialfunktion für den Wellenabnahmeprozess und eine *Sekans hyperbolicus* Funktion für die Wellenberg- und

Wellentalformen bei Ausbreitungswinkeln zwischen 0° und 90° miteinander verbunden werden.

Ein Rechenbeispiel veranschaulicht die Anwendung dieser Gleichungen zur Gefährdungsbeurteilung. In Kombination mit bestehenden Wellenauflaufgleichungen wurden die Gleichungen des Weiteren auf das Impulswellenereignis in 2007 am Chehalis Lake angewendet. Diese Fallstudie weist eine gute Übereinstimmung mit den gemessenen Felddaten auf und bietet eine erste Validierung der experimentellen Ergebnisse im Prototypenmassstab.

Contents

1 Introduction

1.1 General context and delimitations

Massive water waves may be generated if a gravity-driven mass movement, e.g. a landslide, glacier calving, or an avalanche, interacts with a large body of water. The generation mechanism of these waves is characterized by a momentum transfer from the slide mass to the water column. Figure 1.1 shows three wave generation processes depending on the initial position of the slide mass. While subaerial mass movements accelerate before entering the water body at a certain impact velocity, submerged or submarine slide masses are initially at rest and the momentum transfer occurs simultaneously to the acceleration process after failure. Partially submerged slide masses constitute an intermediate state depending on the initial position of the slide centroid relative to the still water surface. This study focuses on waves generated by subaerial mass movements geotechnically classified as extremely rapid landslides (Hungr *et al.* 2013). These waves are commonly referred to as impulse waves (Heller *et al.* 2009). In the past, notable impulse wave events were observed both in inland waters (e.g. Roberts *et al.* 2013) as well as in coastal areas (e.g. Miller 1960). In their preliminary global catalogue, Roberts *et al.* (2014) registered 254 events involving waves generated by subaerial landslides between the 14th century and 2012.

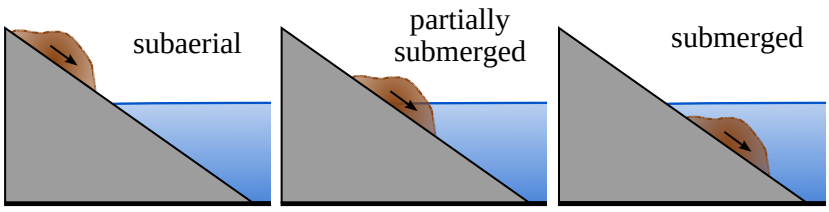

Fig. 1.1 Initial slide mass positions in relation to the still water surface (adapted from Heller 2008)

Three stages constitute an impulse wave event as shown in Figure 1.2. First, in the wave generation stage, the subaerial slide displaces the water and generates a wave train with several crests and troughs. Second, the amplitudes and the shape of the wave train are subject to transformation in the wave propagation stage. These transformation effects include frequency and amplitude dispersion (Heller and Hager 2010) as well as refraction, diffraction, and shoaling depending on the bathymetry (Heller *et al.* 2009). Third, the impulse wave train features impact characteristics similar to tsunami waves upon reaching the shoreline or a dam. The wave-shore or wave-structure interaction processes include wave runup (e.g. Synolakis 1987, Fuchs and Hager 2015, and Hafsteinsson *et al.* 2017), dam overtopping (e.g. Müller 1995, Kobel *et al.* 2017, and Huber *et al.* 2017), or overland flow (e.g. Fuchs and Hager 2015). In addition, the incoming waves are reflected. The

first two stages, namely wave generation and propagation, are accounted for the outgoing impulse wave train within the scope of this study.

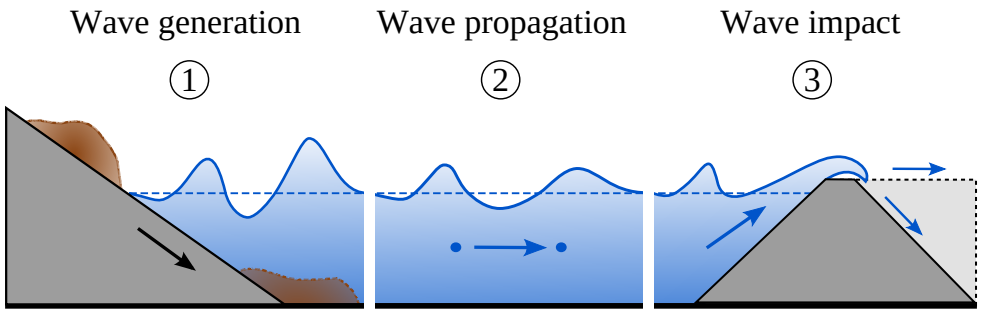

Fig. 1.2 Stages of landslide generated impulse wave event: (1) wave generation, (2) wave propagation, and (3) wave impact including wave runup, dam overtopping, overland flow (adapted from Heller 2008)

Depending on the geometry of the water body, two particular wave propagation patterns may be distinguished as shown in Figure 1.3. Unidirectional wave propagation results, if the slide mass width is larger or equal to the width of an elongated water body. Due to the confinement, lateral wave propagation is prevented and the wave characteristics are identical across the water body width. Therefore, this type of wave propagation is also referred to as two-dimensional (2D). In the case of omnidirectional wave propagation, the slide mass width is substantially smaller than the external dimensions of the water body. The outgoing wave train is not confined and propagates radially from the slide impact location. Omnidirectional wave propagation is therefore referred to as spatial or three-dimensional (3D). In hydraulic experimentation, 2D wave propagation is investigated in wave channels (e.g. Kamphuis and Bowering 1970, Fritz 2002), whereas spatial or 3D, respectively, wave propagation requires wave basins (e.g. Huber 1980, Panizzo *et al.* 2005, Mohammed and Fritz 2012, Heller and Spinneken 2015). The main focus of this study is placed on spatial impulse wave propagation.

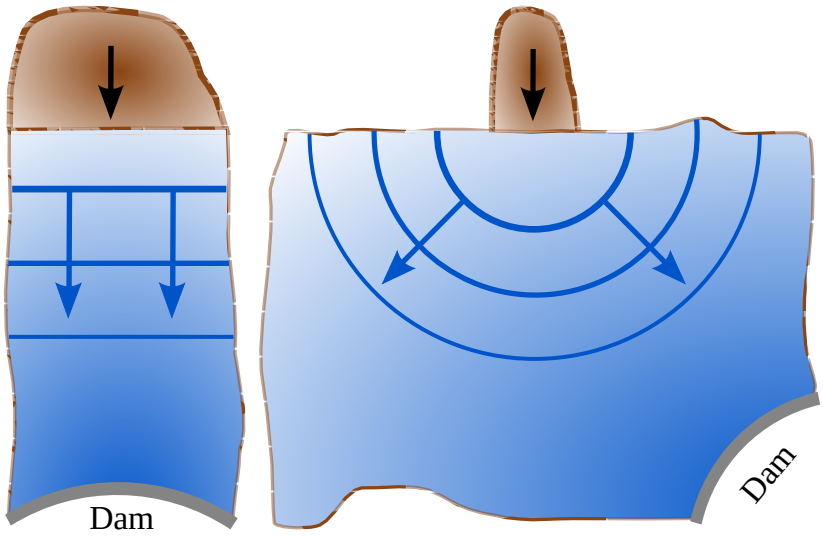

Fig. 1.3 Unidirectional (left) and omnidirectional (right) impulse wave propagation patterns (adapted from Heller *et al.* 2009)

From a hydraulic point of view, the generation of impulse waves is a complex process encompassing the turbulent interaction of three phases, namely slide material, water, and air. Therefore, past hydraulic experimentation has been applied for gaining an insight into these processes and is still an important method besides numerical models to date. The study of Russell (1844) may be regarded as the first impulse wave experiment. One of the different wave generation mechanisms investigated involved a box filled with weights. The box spanned over the whole width on one side of a rectangular wave channel (Figure 1.4). In its initial position, the box is suspended with its bottom slightly submerged. On releasing the box, the water volume beneath the box is displaced and a solitary wave is formed. Russell (1844) found that the water volume displaced by the box is equal to the wave volume. Johnson and Bermel (1949) conducted experiments involving discs falling into a wave basin and referred to the generated waves as “Impulsive Waves”. However, their wave generation mechanism was supposed to replicate the effect of an atomic bomb explosion in shallow water at the Bikini Atoll, Marshall Islands. Miller (1970) and Kamphuis and Bowering (1970) both introduced the term “Impulse Wave”. While the first focused on laboratory wave generation in general, the latter specifically investigated the generation of impulse waves by subaerial landslides.

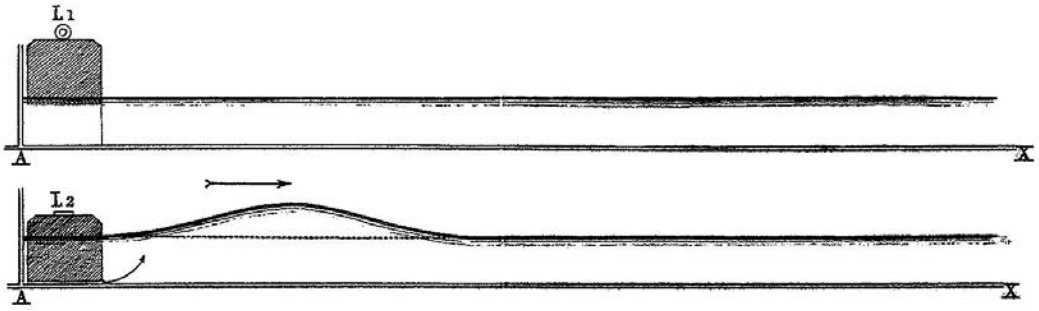

Fig. 1.4 "Genesis by protrusion of a solid" (Russell 1844)

1.2 Previous research at VAW

There is a long-standing history of impulse wave research at the Laboratory of Hydraulics, Hydrology and Glaciology (VAW - Versuchsanstalt für Wasserbau, Hydrologie und Glaziologie) at ETH Zurich both in fundamental and applied investigations. Figure 1.5 shows three different scale models of prototype sites in Switzerland operated in the beginning of the 1970s. The objective of these model studies was the assessment of the impulse wave hazard for predefined scenarios. Following these site-specific model tests, several major studies focusing on the fundamental physical processes related to impulse wave generation, propagation, and impact were initiated, including:

- Huber, Andreas (1980). Schwallwellen in Seen als Folge von Felsstürzen [Impulse waves in lakes resulting from rockfalls]. (in German)
- Sander, Johannes (1990). Weakly nonlinear unidirectional shallow water waves generated by a moving boundary.
- Müller, Dieter R. (1995). Auflaufen und Überschwappen von Impulswellen an Talsperren [Runup and overtopping of impulse waves at dams]. (in German)
- Fritz, Hermann M. (2002). Initial phase of landslide generated impulse waves.
- Zweifel, Andreas (2004). Impulswellen: Effekte der Rutschdichte und der Wassertiefe [Impulse waves: Effects of slide density and water depth]. (in German)
- Heller, Valentin (2007). Landslide generated impulse waves: Prediction of near field characteristics.
- Fuchs, Helge (2013). Solitary impulse wave run-up and overland flow.

The first systematic experiments in a 2D wave channel as well as a 3D wave basin involving free granular slides were conducted by Huber (1980). Sander (1990) focused on the impulse wave generation and propagation in a 2D wave channel applying both an experimental and a numerical approach. Müller (1995) investigated the impulse wave impact and conducted experiments on wave runup and overtopping in 2D and 3D. A pneumatic landslide generator and a purpose-built 2D impulse wave channel were designed and constructed by Fritz (2002) to allow for an independent variation of the governing slide parameters and the application of a Particle Image Velocimetry (PIV) system. Zweifel (2004) extended the

parameter range of Fritz (2002) to slide material featuring a lower density than water on the same experimental setup. Heller (2008) additionally varied the slide impact angle, assessed potential scale effects, and included the measurement data of Fritz (2002) and Zweifel (2004) into a comprehensive analysis. Fuchs (2013) replaced the pneumatic landslide generator with a piston-type wave generator and conducted experiments focusing again on impulse wave impact, more specifically solitary wave runup and overland flow. Applied impulse wave research studies at VAW were presented by Volkart (1974) and Fuchs *et al.* (2011), amongst others.

Fig. 1.5 Applied impulse wave research at VAW with scale models of prototype sites in Switzerland: Lac de Mauvoisin (VAW 1972, left), Ferden compensating reservoir (VAW 1973, center), and Lake Walen (VAW 1974, right)

1.3 Study outline

Following the introduction (Chapter 1), the literature review in Chapter 2 highlights the hazards related to impulse waves by presenting past events and gives an overview of relevant laboratory studies with a particular focus on spatial wave propagation. Existing research gaps and the objectives of this study are stated at the end of the chapter. The concept of similitude is introduced as the basic theory behind the research method of hydraulic experimentation in Chapter 3, in which the experimental setups of the 2D wave channel and 3D wave basin including their instrumentation are also presented. The experimental results presented in Chapter 4 allow for an insight into the spatial impulse wave generation and propagation, identify the governing parameters, and provide empirical equations for the prediction of key wave characteristics. Chapter 5 discusses the results, demonstrates the applicability of the present equations with a computational example, and validates the equations against an impulse wave event at prototype scale. The final Chapter 6 summarizes the major findings of this study, highlights the associated parameter limitations, and gives an outlook for future research.

2 Literature review

2.1 Overview

This chapter provides a general overview of literature on impulse waves generated by subaerial landslides. First, accounts of past events are presented. The Öskjuvatn landslide in 2014 and the Taan Fjord landslide in 2015 are highlighted in particular. Second, the acquisition of required input slide parameters and existing methods for the assessment of impulse wave hazards are discussed. The third part presents studies based on hydraulic experimentation. While the subsection on 2D experiments focuses mainly on previous VAW research, the subsection on 3D experiments includes the equations by Panizzo *et al.* (2005), Heller *et al.* (2009), Mohammed and Fritz (2012), and Heller and Spinneken (2015), which are applied in a comparative study in Section 4.3.3. Thereafter, conventional measurement techniques for tracking spatial wave propagation are presented and the prospects of applying a videometric measurement technique are pointed out. Based on this literature review, existing research gaps are identified and the objectives of this study are formulated. Literature concerning the concept of model similitude and scale effects are presented in Chapter 3.

2.2 Impulse wave hazard

2.2.1 Past events

A multitude of accounts of impulse wave events with spatial propagation patterns generated by subaerial landslides has been reported. The impulse wave event in Lituya Bay, USA, which was triggered by a rockslide after an earthquake in 1958 is one of the most prominent cases (Miller 1960, Slingerland and Voight 1979). A historical example is given by Bornhold *et al.* (2007): In the sixteenth century, impulse waves generated by a rockslide at Knight Inlet, Canada, presumably destroyed an indigenous settlement. In coastal areas, further example include Paatuut, Greenland, in 2000 (Dahl-Jensen *et al.* 2004) as well as impulse waves generated by several earthquake-triggered landslides into Aysén Fjord, Chile, in 2007 (Sepúlveda *et al.* 2010). However, also inland waters such as natural lakes in mountainous regions were subject to landslide generated impulse waves: Reportedly 400 to 600 fatalities were caused in 1971 after a rock avalanche entered Lake Yanahuin, Peru (Plafker and Eyzaguirre 1979); in 1946, a rock avalanche into Landslide Lake, Canada, led to an overspill and destructive downstream flash flood (Evans 1989); and in 2007, Chehalis Lake and River, Canada, were both affected by far-reaching damage along their shoreline (Roberts *et al.* 2013). The event at Chehalis Lake is discussed in detail in Section 5.6. Regarding reservoirs, Walters (1971) describes an event at Pontesei Dam, Italy, in 1959, where a 3 million m^3 landslide generated an impulse wave overtopping the dam crest by a “few meters” despite the water level of the reservoir being 13 m beneath its

maximum capacity level. At nearby Vaiont Dam, Italy, the most fatal impulse wave event at a reservoir happened 4 years later in 1963, when a 270 million m^3 partially submerged landslide displaced the reservoir´s stored water and generated a subsequent flash flood, which destroyed the village of Longarone causing almost 2,000 fatalities (Genevois and Ghirotti 2005). However, there was no distinct wave propagation phase in Vaiont Reservoir as the slide volume almost completely filled the designed reservoir volume of 169 million m^3. A more recent impulse wave event occurred in 2008 in the Wu Gorge of the Three Gorges Reservoir, China, when a slope collapsed on the bank of Yangtze River (Huang *et al.* 2012). Even comparatively small volumes displaced by a slide causing no direct damage might act as a trigger for outburst floods: In 1985, an ice avalanche generated an impulse wave, which overtopped and substantially eroded the moraine dam of Dig Tsho, Nepal, and 5 million m^3 drained subsequently through an eventually 60 m high and 200 m wide breach over 4 to 5 hours at an estimated peak discharge of 1,600 m^3/s (Vuichard and Zimmermann 1987). Further outburst floods triggered by impulse wave overtopping at natural dams include Lake Palcacocha upstream of the city of Huaraz, Peru, in 1941 with some 5,000 fatalities (Carey 2008) as well as Nostetuko Lake in 1983 (Blown and Church 1985, Clague and Evans 2000) and Queen Bess Lake in 1997 (Clague and Evans 2000), both Canada.

A global overview of impulse waves generated by subaerial landslides with 254 events in total was compiled by Roberts *et al.* (2014). Further compilations including also partially submerged slides were presented by Fritz (2002) and Heller (2008). Huber (1982) describes more than 40 events in Switzerland. Two impulse wave events, which took place during the realization of this study, are described in the following.

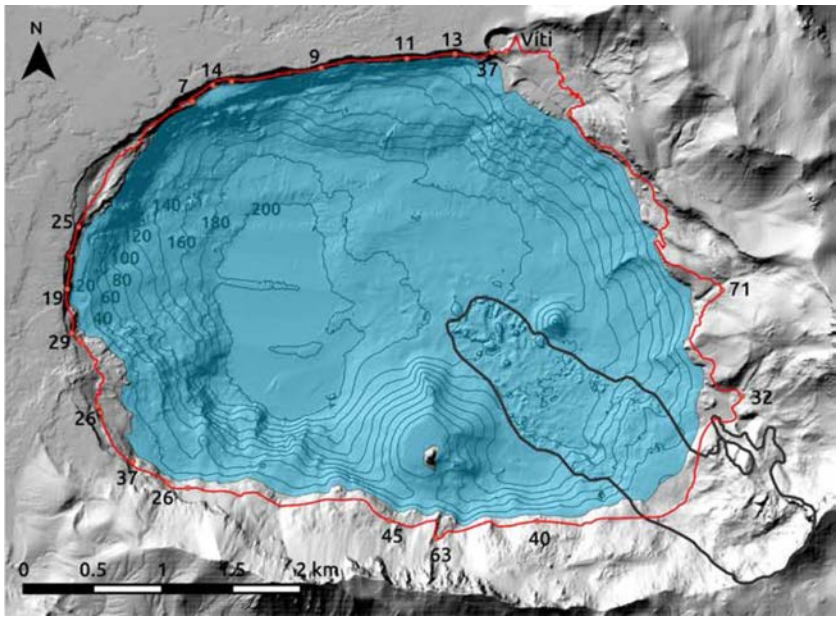

Fig. 2.1 Bathymetry of Öskjuvatn with deposited slide outline (—) and measured runup heights [m] (—) (Gylfadóttir *et al.* 2017)

Fig. 2.2 Photo of Öskjuvatn showing runup traces along shoreline (Gylfadóttir *et al.* 2017)

Öskjuvatn (Lake Askja) landslide, 21 July 2014

Öskjuvatn is located in the inner caldera of Askja, Iceland. On 21 July 2014 a landslide was released from the south-east caldera wall and and entered Öskjuvatn (Gylfadóttir *et al.* 2017). Figure 2.1 shows measured runup heights along the lake shoreline. Its maximum was 71 m above the lake level north of the slide impact location. The wave runup elevations were traceable due to black sand deposits on the surrounding snow patches as shown in Figure 2.2. Gylfadóttir *et al.* (2017) estimated the landslide volume to 10 million m^3 based on an increase of the lake level of 0.65 m after the event.

Taan Fjord landslide, 17 October 2015

Taan Fjord is an arm of Icy Bay in south-east Alaska, USA. On 17 October 2015, a lateral landslide at the terminus of Tyndall Glacier triggered a local megatsunami, which propagated through Taan Fjord and eventually entered Icy Bay (Lynett *et al.* 2016). Figure 2.3 shows a Landsat 8 satellite image of Taan Fjord taken on 15 June 2015, i.e. four months before the event. Almost one year after the event, the Sentinel-2 satellite image shown in Figure 2.4 was taken on 29 September 2016. A comparison of the two images reveals the wave impact along the shoreline of Taan Fjord. Opposite to the landslide source area the vegetation, visible in Figure 2.3, has been washed away as noted from Figure 2.4. Lynett *et al.* (2016) estimate the maximum runup height in this area to 190 m. The river deltas, which are 8 km away from the slide impact location, show extensive traces of the abrasive force of the overland flow induced by the impulse waves. Also Kageet Point, which is located at a distance of 16 km, shows a reduced vegetation cover. Lynett *et al.* (2016) conducted an extensive field campaign and measured the runup heights along Taan Fjord. They found runup heights exceeding 100 m in widespread areas and at least 90% of the approximately 50 km long shoreline had runup traces above 20 m.

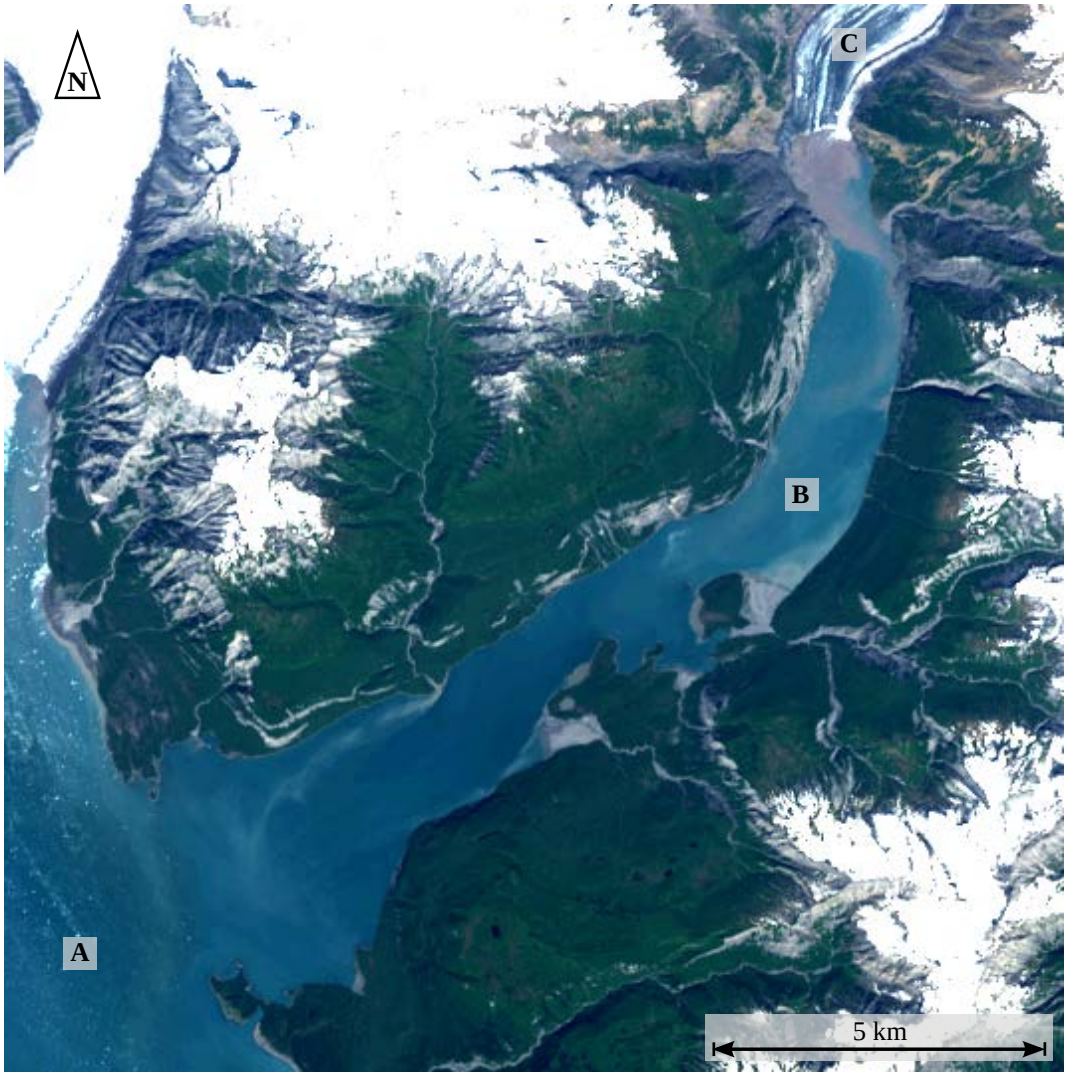

Fig. 2.3 Satellite image of Taan Fjord, USA, with (A) Icy Bay, (B) Taan Fjord, and (C) Tyndall Glacier (Imagery: Landsat 8, 15 June 2015)

2.2.2 Landslide hazard

The assessment of potential impulse waves at endangered water bodies is an integral hazard control measure. At reservoirs, such an assessment is made compulsory by official regulations (Achterberg *et al.* 1998, Pougatsch *et al.* 2002). A comprehensive hazard assessment of the triggering mechanisms of landslide generated impulse waves requires a multidisciplinary approach. Regarding input parameters, expertise by geologists, experts on snow avalanches, and glaciologists, respectively, is needed to identify unstable slopes and the quantification of key slide parameters of landslide or ice and snow avalanches. After the earthquake in Nepal on 25 April 2015, Collins and Jibson (2015) conducted a field survey, including the hazard assessment of potential landslides at the proglacial lake Tsho Rolpa (Figure 2.5). However, the method of visual inspection from a helicopter yielded only limited findings for this specific setting:

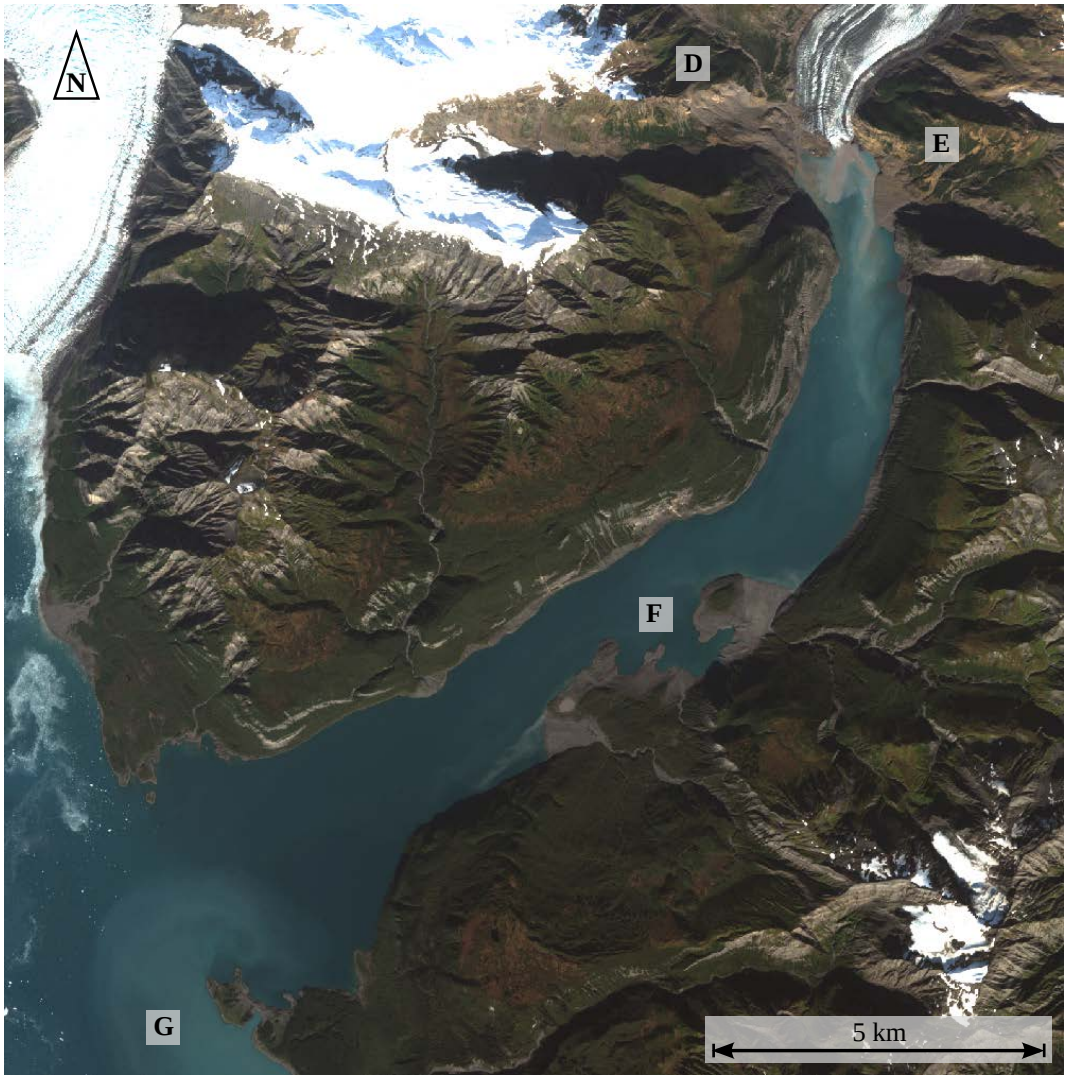

Fig. 2.4 Satellite image of Taan Fjord, USA, with (D) landslide source area, (E) maximum runup, (F) overland flow at river deltas, and (G) Kageet Point (Imagery: Copernicus Sentinel-2, 29 September 2016)

> "Due to the high altitude and abundance of steep rock cliffs adjacent to the lake, we were not able to ascertain whether incipient landslides formed on these slopes as a result of the earthquakes or whether any landslides could pose additional hazards to lake-tsunami generation." Collins and Jibson 2015

Klimeš *et al.* (2016) combined detailed geomorphological, geophysical, and satellite radar interferometric investigations together with laboratory tests on site samples to assess the stability of potential landslide source areas around Lake Palcacocha, Peru. For instable areas, the slide properties at impact onto the still water surface may then be quantified by empirical equations or numerical models (Crosta *et al.* 2003). Besides the slide properties, the point in time when an instable slope will fail is an important information. Active temporary mitigation measures including evacuation or, in case of reservoirs, a draw down

of the water level may be initiated on time. Loew *et al.* (2017) present a monitoring and early warning system for an instable rock slope and evaluate its performance during an actual failure event in Preonzo, Switzerland. The system triggered an alarm with a lead time of several days before the event. The alarm threshold was based on the displacement velocity of the instable rock slope. A system for signalizing ice avalanches into the proglacial Trift lake, Switzerland, is presented by Canassy *et al.* (2011). However, they conclude that the early warning signs of glaciers involve high uncertainties.

Fig. 2.5 Glacial Lake Tsho Rolpa and surrounding Himalayan mountains, Nepal (Photo: Brian D. Collins, USGS)

2.2.3 Impulse wave prediction methods

Based on the slide properties, an assessment of the impulse wave generation and propagation processes may be conducted. Heller *et al.* (2009) differentiate five methods for the prediction of landslide generated impulse waves:

1. Generally applicable equations developed from model tests
2. Prototype-specific model tests
3. Numerical simulations
4. Empirical equations derived from field data
5. Analytical investigations.

Within the context of hazard assessment, Heller *et al.* (2009) consider the first three methods most suitable for practical applications. Item (1) developed from hydraulic experimentation in a wave channel or basin are a method with a comparatively low entry threshold. Its results yield an estimation of the magnitude of an impulse wave event and provide a decision support for the initiation of further more precise assessment methods. However, the underlying model tests may be affected by scale effects (see Section 3.2.3) and the hydraulic processes in water bodies with complex bathymetries may not be sufficiently

resolved. Complex bathymetries are reproducible in detail with Item (2) (e.g. Davidson and McCartney 1975, Chaudhry *et al.* 1983, Fuchs *et al.* 2011, Huang *et al.* 2014, Lindstrøm *et al.* 2014). But scale effects also need to be considered carefully depending on the model dimensions. Item (3) allows for both complex geometries as well as model dimensions at prototype scale not affected by scale effects. Yavari-Ramshe and Ataie-Ashtiani (2016) provide a review of numerical approaches for modelling landslide generated impulse waves. The application of numerical models allows for simulating the physical processes related to the generation and propagation of impulse waves at various levels of abstraction. The choice of these levels may have a significant effect on the quality of the results. Yavari-Ramshe and Ataie-Ashtiani (2016) state that the majority their discussed models approximate either the Navier-Stokes equations for multi-phase flows (air, water, slide material) or the shallow water equations for two-phase flows (slide material beneath water). The Navier-Stokes equations allow for a more comprehensive reproduction of the physical processes, while depth-averaged models based on the shallow water equations are more robust. To take into account dispersive effects in two-layer models, higher order Boussinesq-type equations are applied. Yavari-Ramshe and Ataie-Ashtiani (2016) found the flow field in the majority of numerical models to be specified with an Eulerian (mesh-based) approach and only few models implemented a Lagrangian (mesh-free, e.g. SPH) approach. Although various numerical methods are available, shortcomings in the availability of measurement data from laboratory experiments for validation purposes were identified. Therefore, a particular method calibrated for an individual case yields satisfactory results, but lacks validation against measurement data with a broad parameter range (Heller *et al.* 2009).

2.3 Hydraulic experimentation

2.3.1 Slide type

The generation of landslide generated impulse waves involves the interaction of the phases slide material, water, and air. This complex three-phase hydraulic process within a hydraulic scale model has so far been represented by either a free granular slide or a rigid slide body (Heller and Spinneken 2013). Granular slides were used e.g. by Fritz (2002), Heller (2008), Mohammed and Fritz (2012), Viroulet *et al.* (2014), Lindstrøm *et al.* (2014), and Miller *et al.* (2017); while e.g. Kamphuis and Bowering (1970), Noda (1970), Panizzo *et al.* (2005), Sælevik *et al.* (2009), Di Risio *et al.* (2009), Heller and Spinneken (2013), Viroulet *et al.* (2014) conducted experiments with block models (Evers and Hager 2015a). Zweifel (2004) and Ataie-Ashtiani and Nik-Khah (2008) presented results based on both approaches. While granular slides are deformable before and after impact onto the water surface, the shape of rigid slide bodies remains unaltered. Besides the effect on the wave generation process (Zweifel 2004), the slide type influences the measurement of the slide velocity and consequently its definition. The velocity of the slide front shortly before

impact is directly measurable with high-speed cameras or light barriers for both granular and rigid slides. While the slide centroid velocity is equal to slide front velocity for rigid slides, the mass flux has to be taken into account for granular slides (Fritz 2002). Volkart (1974) found that the slide centroid velocity accounts for only 45% to 63% of slide front velocity for avalanche-like granular flows. Heller (2008) and Di Risio *et al.* (2011) review hydraulic model tests for both granular and rigid slides.

2.3.2 2D experimentation

In 2D experiments impulse wave characteristics are measured along the length and depth axes of a wave channel, while constant conditions are considered across the channel width. Figure 2.6 shows a definition plot of the governing slide parameters. These include the slide centroid velocity V_s or the slide front velocity V_f, respectively, the bulk slide mass m_s, the slide thickness s, the slide width b, the slide length l_s, the slide impact angle α, and the still water depth h. The slide parameters allow for the quantification of wave characteristics along the channel's length axis $r = x$ limited to a single wave propagation angle $\gamma = 0°$. The wave characteristics include the wave crest (subscript c) and trough (subscript t) amplitudes a_c and a_t as well as the wave height H, which are referenced to their location within in the wave train (subscript 1 and 2).

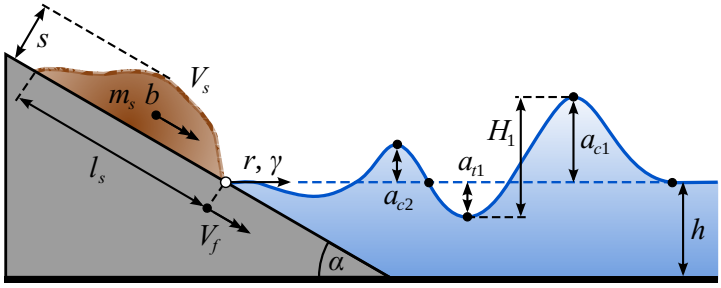

Fig. 2.6 Definition plot for spatial impulse wave generation with 2D parameters and target wave characteristics

According to Di Risio *et al.* (2011), most empirical equations for the prediction of wave characteristics include the slide Froude number F, the relative slide thickness S, and the relative slide mass M, which are defined as

$$\mathsf{F} = \frac{V_s}{\sqrt{gh}} \tag{2.1}$$

$$S = \frac{s}{h} \tag{2.2}$$

$$M = \frac{m_s}{(\rho_w b h^2)}. \tag{2.3}$$

Heller (2008) integrated original wave channel experiments with a reanalysis of the data of Fritz (2002) and Zweifel (2004). A total of 434 experiments involving free granular slides were evaluated. The slide characteristics were combined into a single dimensionless parameter, the impulse product parameter

$$\mathsf{P} = \mathsf{F} S^{0.5} M^{0.25} \left\{\cos\left([6/7]\,\alpha\right)\right\}^{0.5}. \tag{2.4}$$

Eq. (2.4) includes the slide Froude number F , which in turn contains the slide centroid velocity V_s. The maximum (subscript M) wave amplitude a_M, its location x_M, and the maximum wave height H_M were directly derived from P as (Heller 2008)

$$A_M = a_M/h = (4/9)\mathsf{P}^{0.8} \tag{2.5}$$

$$X_M = x_M/h = (11/2)\mathsf{P}^{0.5} \tag{2.6}$$

$$Y_M = H_M/h = (5/9)\mathsf{P}^{0.8}. \tag{2.7}$$

In contrast to the representation in Figure 2.6, Eqs. (2.5), (2.6), and (2.7) do not distinguish the position of the maximum wave feature within the wave train, i.e. a_M may occur at the first wave crest as well as the second wave crest. To describe the wave decay process, a relative propagation distance $X = x/h$ is introduced, equal to r/h for a single wave propagation angle $\gamma = 0°$. The 2D wave amplitudes $a_{2\mathrm{D}}$ and the wave heights $H_{2\mathrm{D}}$ were fitted as (Heller 2008)

$$A_{2\mathrm{D}}(X) = a_{2\mathrm{D}}(x)/h = (3/5)\left(\mathsf{P}X^{-1/3}\right)^{0.8} \tag{2.8}$$

$$Y_{2\mathrm{D}}(X) = H_{2\mathrm{D}}(x)/h = (3/4)\left(\mathsf{P}X^{-1/3}\right)^{0.8}. \tag{2.9}$$

The mean wave celerity c_{am} was derived from the mean wave amplitude a_m as (Heller 2008)

$$\frac{c_{am}}{(gh)^{0.5}} = \left(1 + 2\left(\frac{a_m}{h}\right)^2\right)^{0.5}. \tag{2.10}$$

The mean wave amplitude a_m is defined as the averaged value of the wave amplitude along its propagation distance.

2.3.3 3D experimentation

While a single propagation direction is considered in 2D experiments, omni-directional propagation patterns are accounted for in 3D experiments. By approximation, impulse waves generated by landslides propagate radially from a spatially confined impact location. Polar coordinates are used for describing the relevant wave features (Figure 2.7). The pole thereby represents the slide impact location center and the angular and radial coordinates equal the wave propagation angle γ and distance r, respectively. All equations presented hereafter relate to free and undisturbed wave propagation, i.e. edge waves along the shore are excluded.

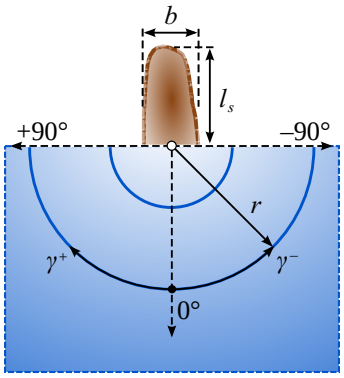

Fig. 2.7 Definition plot of polar coordinates for spatial impulse wave propagation; for additional 2D slide parameters see Figure 2.6

Rigid slide bodies were applied by Panizzo *et al.* (2005) for their wave basin experiments with slide impact angles α between 16° and 36°. The slide body was released on an inclined rack with a spring system at its bottom, which stopped the sliding motion and partially absorbed the momentum, therefore. By analogy with Walder *et al.* (2003), the dimensionless time of the landslide underwater motion

$$t_s^* = t_s \sqrt{g/h} = 0.43 \, (A_w^*)^{-0.27} \, \mathsf{F}^{-0.66} \, (\sin \alpha)^{-1.32} \tag{2.11}$$

was identified as a relevant quantity to characterize the generated impulse waves based on the slide Froude number F, the slide impact angle α, and the dimensionless slide front surface $A_w^* = bs/h^2$. As a rigid slide was applied, the slide centroid velocity equalled the slide front velocity. The relative wave height decay was then fitted with

$$Y_1 = \frac{H_1}{h} = 0.07 \, (t_s^*)^{-0.3} \, (A_w^*)^{0.88} \, (\sin \alpha)^{-0.8} \exp(1.37 \cos \gamma) \left(\frac{r}{h}\right)^{-0.81} . \tag{2.12}$$

Information on the slide mass m_s is included neither in Eq. (2.11) nor in Eq. (2.12). Therefore, an impulse wave assessment for slides with the same geometrical dimensions but different slide bulk densities ρ_s would yield the same results. Eqs. (2.11) and (2.12)

include $A_w^* = bs/h^2$ representing the slide thickness s and the slide width b as slide geometry parameters. Consequently, doubling s would have the same effect on the wave height as doubling b.

Heller *et al.* (2009) merged the equation of spatial wave height decay by Huber and Hager (1997) with the impulse product parameter P (Eq. 2.4). The relative first wave height generated by granular slides is given as

$$Y_1 = \frac{H_1}{h} = (3/2)\,\mathsf{P}^{0.8}\cos^2\left(\frac{2\gamma}{3}\right)\left(\frac{r}{h}\right)^{-2/3}. \tag{2.13}$$

The combination of a generation term and propagation term was theoretically deduced and lacks a common empirical basis. Since Eq. (2.13) includes P, the slide centroid velocity of the granular slide has to be accounted for in the slide Froude number F. The lower limit of applicability of Eq. (2.13) is $r/h = 5$.

Mohammed and Fritz (2012) presented a detailed study of the wave amplitudes within the wave train for a fixed slide impact angle $\alpha = 27.1°$. The first wave crest amplitude a_{c1}, first wave trough amplitude a_{t1}, and the second wave crest amplitude a_{c2} were fitted separately. The experiments were conducted with free granular slides. However, the slide front velocity V_f (Figure 2.6) was included as a governing parameter yielding the slide front Froude number $\mathsf{F}_f = V_f/\sqrt{gh}$. The relative wave amplitudes were given as

$$A_{c1} = \frac{a_{c1}}{h} = k_{ac1}\left(\frac{r}{h}\right)^{n_{ac1}}\cos\gamma \tag{2.14}$$

$$A_{t1} = \frac{a_{t1}}{h} = k_{at1}\left(\frac{r}{h}\right)^{n_{at1}}\cos\gamma \tag{2.15}$$

$$A_{c2} = \frac{a_{c2}}{h} = k_{ac2}\left(\frac{r}{h}\right)^{n_{ac2}}\cos^2\gamma. \tag{2.16}$$

Similar to Panizzo *et al.* (2005) and Heller *et al.* (2009), Eqs. (2.14), (2.15), and (2.16) feature a cosine function to represent the wave shape as a function of the wave propagation angle γ. However, all amplitudes then equal zero for $\gamma = 90°$. Wave generation and decay terms are included as variables, which are based on dimensionless slide properties. These terms are

$$k_{ac1} = 0.31\mathsf{F}_f^{2.1}S^{0.6} \tag{2.17}$$

$$k_{at1} = 0.7\mathsf{F}_f^{0.96}S^{0.43}\left(l_s/h\right)^{-0.5} \tag{2.18}$$

$$k_{ac2} = \mathsf{F}_f S^{0.8}B^{-0.4}\left(l_s/h\right)^{-0.5} \tag{2.19}$$

$$n_{ac1} = -1.2\mathsf{F}_f^{0.25} S^{-0.02} B^{-0.33} \tag{2.20}$$

$$n_{at1} = -1.6\mathsf{F}_f^{-0.41} B^{-0.02} \left(l_s/h\right)^{-0.14} \tag{2.21}$$

$$n_{ac2} = -1.5\mathsf{F}_f^{-0.5} B^{-0.07} \left(l_s/h\right)^{-0.3} \tag{2.22}$$

In addition to the slide front Froude number F_f, the relative slide thickness S, and the relative slide width $B = b/h$, the relative slide length l_s/h are also accounted for. Note, that the slide mass m_s is not included, however. The first wave height is given by

$$Y_1 = \frac{H_1}{h} = A_{c1} + A_{t1}. \tag{2.23}$$

Heller and Spinneken (2015) conducted experiments with wedge shaped rigid bodies. The slide impact angle was fixed at $\alpha = 45°$. In contrast to Panizzo *et al.* (2005), the rigid slides were not stopped at the base point of the sliding plane but underwent a transition of its moving direction parallel to the basin bottom. The transition was induced through a circularly bent metal sheet. As a rigid slide was applied, the slide centroid velocity equalled the slide front velocity. The wave height decay was determined as

$$Y_1 = \frac{H_1}{h} = 2.75\mathsf{F}^{0.67} S M^{0.6} \left(\frac{r}{h}\right)^{-1} f_\gamma. \tag{2.24}$$

The relative slide thickness S is the dimensionless quantity with the highest exponent and therefore also the strongest effect on the initial wave height generation. The decay rate for $\gamma = 0°$ has a fixed exponent of -1. The wave crest shape for different wave propagation angles γ is defined as

$$f_\gamma = \left[\cos\left(\frac{2\gamma}{3}\right)\right]^{2\{1+\exp[-0.2(r/h)]\}}. \tag{2.25}$$

While the wave crest shape remains constant in Eqs. (2.13) and (2.14), Eq. (2.25) features an exponent including the relative wave propagation distance r/h as a parameter.

Table 2.1 Overview of dimensionless slide parameter ranges of (a) Panizzo *et al.* (2005), (b) Heller *et al.* (2009), (c) Mohammed and Fritz (2012), and (d) Heller and Spinneken (2015)

Study	F [-]	S [-]	M [-]	B [-]	l_s/h	α [°]	P [-]
(a)	1 - 2.2	0.11 - 0.45	-	0.38 - 1.5	-	16 - 36	-
(b)	0.86 - 6.83	0.09 - 1.64	0.11 - 10.02	0.74 - 3.33	-	30 - 90	0.17 - 8.13
(c)	1 - 4	0.1 - 0.9	-	1 - 7	2.5 - 6.8	27.1	-
(d)	0.54 - 2.47	0.2 - 0.5	0.25 - 2.49	1.2 - 2.4	0.73 - 3.66	45	0.16 - 1.56

The experimental parameter ranges of the above equations are given in Table 2.1. Further experimental studies with an omni-directional wave propagation pattern were presented by Ataie-Ashtiani and Nik-Khah (2008), Huang *et al.* (2013), and Bregoli *et al.* (2017). However, all three studies only account for a single wave propagation angle $\gamma = 0°$ so that they are not presented in detail.

2.3.4 Prototype parameters

To provide a comparison to the experimental parameters presented in the preceding sections, the dimensionless slide parameters at four selected prototype locations are listed in Table 2.2 ordered by the impulse product parameter P. While the parameters at Kühtai Reservoir (Fuchs *et al.* 2011) and Lake Lucerne (Fuchs and Boes 2010) are taken from scenarios of potential impulse wave events in the future, Chehalis Lake (Roberts *et al.* 2013, Wang *et al.* 2015, Bregoli *et al.* 2017) and Lituya Bay (Heller 2008) are past events (see Section 2.2.1). Hazard assessments were conducted based on slide parameters predicted with geotechnical methods for the scenarios at Kühtai Reservoir and Lake Lucerne. In comparison to the events at Chehalis Lake and Lituya Bay, these slide scenarios generate only small waves. Nevertheless, adjacent infrastructure and settlements bear a high vulnerability. As is apparent from Table 2.1, all experimental parameters are within the order of magnitude of the selected prototype locations. However, note that some of the prototype parameters in Table 2.2 already range over two orders of magnitude, highlighting the extensive parameter range of relevant impulse wave events.

Table 2.2 Overview of dimensionless slide parameter ranges at Kühtai Reservoir (Fuchs *et al.* 2011), Lake Lucerne (Fuchs and Boes 2010), Chehalis Lake (Roberts *et al.* 2013, Wang *et al.* 2015, Bregoli *et al.* 2017), and Lituya Bay (Heller 2008)

Location	F [-]	S [-]	M [-]	B [-]	α [°]	P [-]
Kühtai Reservoir (AT)	0.32	0.06	0.02	0.30	36	0.03
Lake Lucerne (CH)	1.11	0.36	0.10	0.37	70	0.27
Chehalis Lake (CA)	1.75	0.33	1.63	1.75	30	1.08
Lituya Bay (US)	2.66	0.75	6.74	6.75	40	3.37

2.4 Water surface tracking

Impulse waves in a 2D wave channel are directly traceable through a glass sidewall with a camera. In addition to point measurements with e.g. capacitance wave gauges (intrusive) or ultrasonic distance sensors (non-intrusive), an image of the continuous water surface profile allows for the identification of wave features independent from fixed measurement locations. Given a sufficient frame rate, the detection of maximum wave amplitudes as well as their location may be carried out adaptively with reasonable accuracy. This technique is well established and was applied in the past to study various hydraulic phenomena

including runup and overtopping in wave channels (e.g. Fuchs and Hager 2015, Kobel *et al.* 2017, Hafsteinsson *et al.* 2017, and Huber *et al.* 2017). Omni-directional impulse wave propagation in a 3D wave basin is not directly traceable. Several wave gauges are needed to cover 3D wave propagation with a sufficient spatial resolution. Mohammed and Fritz (2012) installed 4 wave gauges for $\gamma = 0°$ and 5°, 3 wave gauges for $\gamma = 13°$, 21° and 30°, and 2 wave gauges $\gamma = 45°$ and 60°. Heller and Spinneken (2015) and Romano *et al.* (2016) applied a pivoting rack, which was moved between repetitive experiments with an identical parameter set. While the number of wave gauges was reduced with this method, the number of repetitive experiments was substantially increased. However, none of these approaches allows for adaptively tracking wave features in the near field of the slide impact location as in 2D with a side camera. To overcome this limitation, Bregoli *et al.* (2017) developed a videometric measurement system which applies laser sheet projections on water dyed with 5 kaolin, allowing for a continuous tracking of the water surface along the laser sheets. In their experimental setup, one green laser sheet was aligned along the wave propagation angle $\gamma = 0°$, while six red laser sheets were equally distributed over a maximum propagation distance of 4.1 m perpendicular to the first. Therefore, a continuous water surface profile was only tracked for $\gamma = 0°$. Nevertheless, the application of a videometric measurement approach for tracking spatial impulse waves has the potential to overcome the limitations of standard wave gauges.

Videometric measurement techniques for continuously tracking free water surface profiles in arbitrary directions were applied by e.g. Tsubaki and Fujita (2005) and Cobelli *et al.* (2009). Both approaches are based on projections onto the water surface and are non-intrusive, e.g. no tracer particles are applied. Tsubaki and Fujita (2005) tracked a hydraulic jump in a flume. They projected a rasterized grey scale pattern onto a measuring field of 0.02 m^2. Cobelli *et al.* (2009) created waves as well as a vortex in a small wave tank of 1.5 m length and 0.5 m width. Their measuring field amounted to 0.135 m^2 and a fringe projection was applied. Compared to the wave basin dimensions of e.g. Huber and Hager (1997) with 60 m^2 or Panizzo *et al.* (2005) with 72 m^2, these measuring fields cover only small areas of the total water surface. It was necessary for both videometric applications to attain an opaque water surface for the projection. Przadka *et al.* (2012) tested different white dyes and found a content of 4 kg/m^3 of the anatase (TiO_2) pigment KRONOS 1002 (KRONOS Worldwide, Inc., Dallas, USA) in deionized water to be suited best for this task, as a high opacity is achieved while maintaining the damping properties of water.

2.5 Summary

2.5.1 Research gaps

The research gaps identified within the literature review are:

- Existing 3D prediction equations feature serious limitations regarding slide parameter ranges, slide type, or lack of experimental proof (Section 2.3.3).

- These limitations may affect their general applicability for impulse wave hazard assessment studies (Section 2.2.3).
- Conventional wave gauges at fixed measurement points offer only limited capabilities for tracking spatial wave propagation patterns especially in the near field of the slide impact location (Section 2.4).
- While side cameras are suitable for continuously tracking wave profiles in the slide impact zone for the 2D wave channel setup with a single wave propagation angle, this approach is not directly applicable to the 3D wave basin setup involving multiple wave propagation angles (Section 2.4).
- Videometric measurement techniques have been successfully applied for tracking arbitrary water surfaces within measuring fields up to 0.135 m^2, which is insufficient in comparison to previous experimental setups for investigating spatial impulse wave propagation (Section 2.4).
- The development of numerical methods requires validation against 3D measurement data sets incorporating a broad range of slide parameters (Section 2.2.3).

2.5.2 Objectives

The objectives of this study are:

- Advancing the understanding of the physical features related to 3D impulse wave generation and propagation.
- Providing a proof-of-concept that the hybrid approach with mesh-packed slides generates wave features similar to free granular slides, while offering the advantages of rigid slide bodies in terms of simplified handling and efficiently collecting the slide material.
- Application of a non-intrusive videometric measurement technique for quasi-continuously tracking arbitrary water surfaces at laboratory scales suitable for the efficient investigation of spatial impulse wave propagation.
- Development of empirical equations to predict the spatial impulse wave features for wave propagation angles $0° \leq \gamma \leq 90°$ for an extended slide parameter range including a systematic variation of the slide width b.
- Validation of the empirical equations against a prototype impulse wave event to demonstrate their applicability in the context of hazard assessment.
- Providing measurement data with a high spatial and temporal resolution to validate existing and future numerical schemes.

3 Physical models

3.1 Overview

The generation and spatial propagation processes of landslide generated impulse waves were investigated with two physical models. Both models were based on Froude similitude. The concept of model similitude and limitations due to scale effects are discussed in Section 3.2. The first model setup was a 2D wave channel, where experiments with slides made of mesh bags filled with granular material were conducted (Section 3.3). The objective of these experiments was to provide a proof-of-concept that mesh-packed slides generate wave characteristics similar to free granular slides. The second setup was a 3D wave basin, where the impulse waves propagate radially from the impact location. Again, mesh-packed slides were employed for wave generation. Section 3.4 describes the general layout of the basin, introduces the videometric measurement technique applied for tracking the free water surface, and explains the subsequent data processing approach.

3.2 Model similitude

3.2.1 Similarity

Laboratory experiments were conducted with the aim to simulate the processes of spatial impulse wave propagation, which occur at a much larger scale in nature. While the hydraulic processes in nature take place at prototype (subscript *P*) scale, the experiments replicate these processes at model (subscript *M*) scale. The theory of similarity differentiates three levels between these two scales: *geometric*, *kinematic*, and *dynamic similarity* as shown in Figure 3.1 (Novak *et al.* 2010, Heller 2011, Chadwick *et al.* 2013).

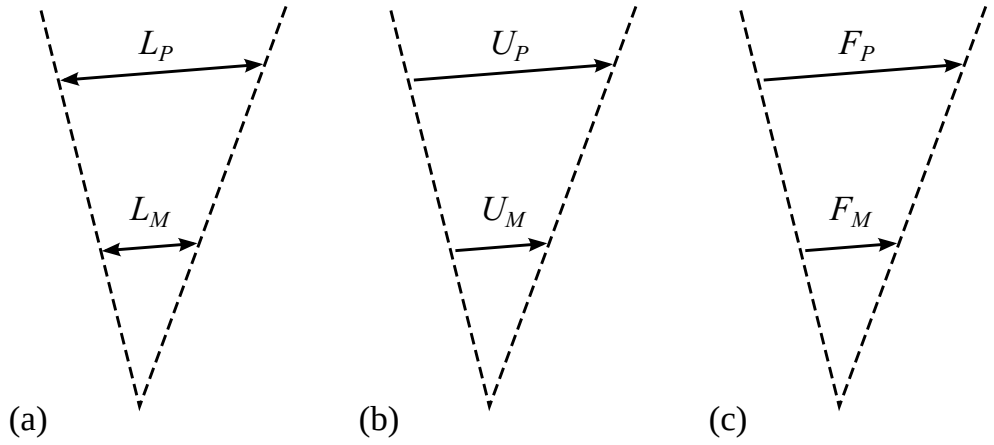

Fig. 3.1 (a) Geometric, (b) kinematic, and (c) dynamic similarity with lengths L, velocities U, and forces F for prototype (subscript P) and model (subscript M) (adapted from Chadwick *et al.* 2013)

Geometric similarity requires that all equivalent lengths at prototype and model scale have the same ratio and all equivalent angles are identical. The ratio of a corresponding length at prototype scale L_P to model scale L_M is defined as the length scale factor

$$\lambda_L = \frac{L_P}{L_M}. \tag{3.1}$$

Consequently, areas and volumes are scaled with λ_L^2 and λ_L^3, respectively. *Kinematic similarity* adds the fundamental dimension of time and implies a constant velocity ratio between prototype U_P and model U_M. The velocity scale factor is defined as

$$\lambda_U = \frac{U_P}{U_M}. \tag{3.2}$$

Since velocity has the fundamental dimensions [LT^{-1}], the velocity scale factor may be restated with the corresponding scale factors for length $\lambda_L = L_P/L_M$ and time $\lambda_T = T_P/T_M$ (Chadwick *et al.* 2013). Besides velocity, kinematic similarity requires time-dependent quantities including acceleration and discharge to have constant ratios between prototype and model (Heller 2011). To attain *dynamic similarity*, all corresponding forces have to be constant with a force scale ratio

$$\lambda_F = \frac{F_P}{F_M}. \tag{3.3}$$

The force is generally defined as mass $\times$ acceleration and features the fundamental dimensions [MLT^{-2}]. Therefore, force may be restated with the scale factors $\lambda_L = L_P/L_M$, $\lambda_T = T_P/T_M$ and $\lambda_M = M_P/M_M$ (Chadwick *et al.* 2013). Each level of similarity includes its preceding, e.g. dynamic similarity also includes geometric and kinematic similarity. According to Hughes (1993) and Heller (2011), the most relevant forces in hydraulic modelling are the inertial force, gravity, viscous force, surface tension force, elastic compression force, and pressure forces. Perfect dynamic similarity is attained, if all these forces have an equal ratio between prototype and model. Consequently, all ratios among these forces at the same scale also have to be identical both at prototype and at model scale (Heller 2011). However, there is no known fluid satisfying equal force ratios of all relevant forces between prototype and a scale model (Hughes 1993). Depending on the experimental setup, the most relevant force ratio has to be determined and the effect of neglecting the other force ratios, referred to as *scale effects*, has to be quantified. In free surface hydraulics, the most often applied force ratio is between inertial force and gravity force (Heller 2011), which is defined as the general Froude number (subscript G)

$$\mathsf{F}_G = \sqrt{\frac{\text{inertial force}}{\text{gravity force}}} = \frac{U}{\sqrt{gL}}. \tag{3.4}$$

Froude similitude applies, when equal Froude numbers F_G prevail at prototype and model scale. Hydraulic experimentation of landslide generated impulse waves is generally based on Froude similitude (Heller *et al.* 2008) and was applied for the 2D wave channel as well as for the 3D wave basin experiments. Potential scale effects arising from the application of laboratory models with Froude similitude are discussed in Section 3.2.3.

3.2.2 Dimensional analysis

The theory of dimensional analysis allows for the derivation of dimensionless relationships to describe the behavior of a hydraulic phenomenon (Novak *et al.* 2010, Chadwick *et al.* 2013). A physical system, representing a hydraulic phenomenon in this context, may be described as a function of n quantities Q

$$\mathrm{f}(Q_1, Q_2, Q_3, ..., Q_n) = 0. \tag{3.5}$$

The Π theorem of Buckingham (1914) states that Eq. (3.5) is reduced to $i = n - k$ dimensionless quantities Π, with k as the number of fundamental dimensions involved, e.g. length [L], time [T], or mass [M]

$$\mathrm{F}(\Pi_1, \Pi_2, \Pi_3, ..., \Pi_i) = 0. \tag{3.6}$$

Perfect similitude requires all dimensionless quantities Π to be equal at prototype and at model scale; e.g. $\Pi_{1,P} = \Pi_{1,M}$.

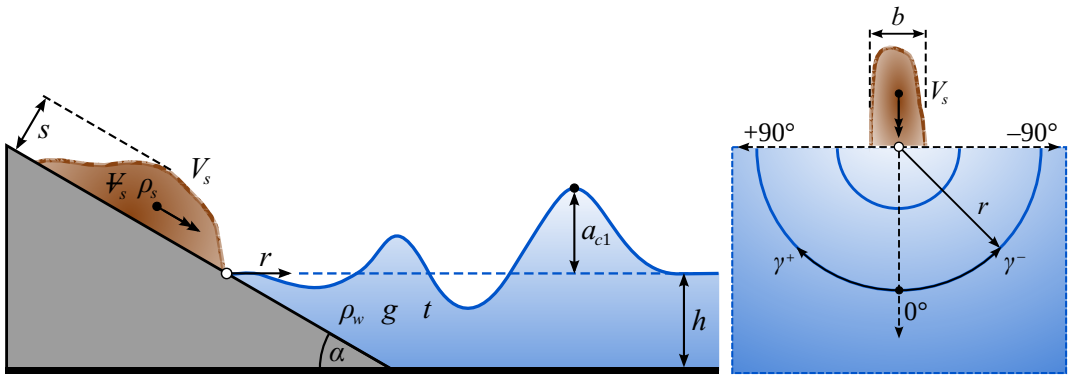

Fig. 3.2 Definition plot for spatial impulse waves with selected independent governing parameters and first wave crest amplitude a_{c1} as dependent target variable

Figure 3.2 shows as definition plot of the physical system, representing spatial impulse waves generated by subaerial landslides. It includes $n = 13$ selected quantities of the 3D wave basin experiments, subdivided into 12 independent governing parameters and the first wave crest amplitude a_{c1} as dependent target variable. The independent governing parameters and their test ranges are specified in Table 3.1. Selecting the quantities for

experimentation is an arbitrary process (Novak *et al.* 2010) based on experience and still may lead to omittance of key governing parameters, while including others with no influence on the target variable. The selected governing parameters for spatial impulse waves in Figure 3.2 were based on the comprehensive analysis by Heller and Hager (2010) of in total 434 plane impulse wave tests conducted by Fritz (2002), Zweifel (2004), and Heller (2008). The quantities of the 2D wave channel experiments with mesh-packed slides are not described hereafter, but are elaborated by Heller *et al.* (2008) and Heller (2008) for this specific experimental setup.

Table 3.1 Governing independent parameters for spatial impulse waves

Symbol	Unit	Dimension	Description	Test range
V_s	[m/s]	[LT^{-1}]	Slide impact velocity	0.72 - 4.76
$\forbar{V}_s$	[m^3]	[L^3]	Bulk slide volume	0.0075 - 0.0299
ρ_s	[kg/m^3]	[ML^{-3}]	Bulk slide density	1,338
s	[m]	[L]	Slide thickness	0.06 - 0.12
b	[m]	[L]	Slide width	0.25 - 1.00
α	[°]	[-]	Slide impact angle	30 - 90
h	[m]	[L]	Still water depth	0.2 - 0.4
ρ_w	[kg/m^3]	[ML^{-3}]	Water density	1,000
g	[m/s^2]	[LT^{-2}]	Gravitational acceleration	9.81
r	[m]	[L]	Radial wave propagation distance	0.45 - 3.26
γ	[°]	[-]	Wave propagation angle	0 - 90
t	[s]	[T]	Time	0 - 10

Based on these independent governing parameters, the first wave crest amplitude a_{c1} may be generally quantified by

$$a_{c1}(r,\gamma) = f\left(V_s, \forbar{V}_s, \rho_s, s, b, \alpha, h, \rho_w, g, r, \gamma, t\right). \tag{3.7}$$

The physical system shown in Figure 3.2 consists of $k = 3$ fundamental dimensions, namely length [L], time [T], and mass [M] (Table 3.1). By applying dimensional analysis to Eq. (3.7), the 12 governing parameters were reduced to 9 dimensionless quantities analogous to Heller *et al.* (2008) and Heller (2008). The three selected reference parameters are still water depth h, gravitational acceleration g, and water density ρ_w. The procedure of dimensional analysis is demonstrated by Heller (2011) using the example of the slide impact velocity V_s. The dimensionless quantity $\Pi_1$is found by balancing it with V_s and the three reference parameters h, g, and ρ_w, featuring three unknown exponents υ, φ, and ω:

$$\Pi_1 = V_s h^{\upsilon} g^{\varphi} \rho_w^{\omega}. \tag{3.8}$$

Regarding its fundamental dimensions Eq. (3.8) is reformulated as:

$$[-] = [\mathrm{LT}^{-1}][\mathrm{L}]^{\upsilon}[\mathrm{LT}^{-2}]^{\varphi}[\mathrm{ML}^{-3}]^{\omega}. \tag{3.9}$$

Based on its fundamental dimensions, Eq. (3.9) is represented as a system of equations:

$$\begin{array}{rrcl} [L]: & 0 & = & +1+1\upsilon+1\varphi-3\omega \\ [T]: & 0 & = & -1+0\upsilon-2\varphi+0\omega \\ [M]: & 0 & = & +0+0\upsilon+0\varphi+1\omega \end{array} . \tag{3.10}$$

Solving Eq. (3.10) yields $\upsilon = -1/2$, $\varphi = -1/2$, and $\omega = 0$. The dimensionless parameter Π_1 was defined by Kamphuis and Bowering (1970) as the slide Froude number F upon impact with the water:

$$\Pi_1 = \mathsf{F} = \frac{V_s}{\sqrt{gh}}. \tag{3.11}$$

The further governing dimensionless parameters Π_2 to Π_8 are listed in Table 3.2.

Table 3.2 Governing dimensionless parameters for spatial impulse waves

Symbol	Description	Test range
$\Pi_1 = \mathsf{F} = V_s/\sqrt{gh}$	Slide Froude number	0.40 - 3.40
$\Pi_2 = V = \forall_s/(bh^2)$	Relative bulk slide volume	0.187 - 0.750
$\Pi_3 = D = \rho_s/\rho_w$	Relative bulk slide density	1.338
$\Pi_4 = S = s/h$	Relative slide thickness	0.15 - 0.6
$\Pi_5 = B = b/h$	Relative slide width	0.83 - 5.00
$\Pi_6 = \alpha$	Slide impact angle	30 - 90
$\Pi_7 = r/h$	Relative radial wave propagation distance	1.1 - 16.3
$\Pi_8 = \gamma$	Wave propagation angle	0 - 90
$\Pi_9 = T = t\sqrt{g/h}$	Relative time	0 - 70

Additionally, Zweifel *et al.* (2006) introduced the relative slide mass $M = VD$ as a combination of the relative bulk slide volume and density. Therefore, the physical system of Eq. (3.7) may be generally reformulated for describing the relative first wave crest amplitude A_{c1} based on the derived dimensionless governing parameters with

$$A_{c1}(r/h,\gamma) = a_{c1}(r,\gamma)/h = F(\mathsf{F},M,S,B,\alpha,r/h,\gamma,T). \tag{3.12}$$

A major advantage of the dimensionless description of a physical system is the fact that it simplifies its interpretation (Novak *et al.* 2010). However, no evidence of potential scale effects follows by the analysis. While the water density ρ_w was selected above as a parameter, other fluid characteristics, e.g. viscosity or surface tension, were excluded. Consequently, potential scale effects arise, which are discussed in the following section.

3.2.3 Scale effects

The spatial impulse wave experiments were modelled according to Froude similitude, i.e. the force ratio of inertial to gravity forces. As described in Section 3.2.1, neglecting other force ratios potentially leads to significant scale effects. According to Heller (2011), the application of Froude similitude excludes the effects of the

$$\text{Reynolds number } \mathsf{R} = \frac{\sqrt{gh^3}}{\nu_w}, \tag{3.13}$$

$$\text{Weber number } \mathsf{W} = \frac{\rho_w g h^2}{\sigma_w}, \tag{3.14}$$

$$\text{Cauchy number } \mathsf{C} = \kappa_w \rho_w V_s^2. \tag{3.15}$$

These dimensionless numbers include the celerity of shallow-water waves $c = \sqrt{gh}$ [m/s], the kinematic fluid viscosity of water ν_w [m^2/s], the water surface tension σ_w [N/m], and the water compressibility κ_w [m^2/N].

The Reynolds number R (Eq. 3.13) accounts for the ratio of inertial to viscous forces (Hughes 1993). Wave attenuation during propagation is influenced by viscous effects and Heller *et al.* (2008) state that laboratory scale impulse waves affected by scale effects travel more slowly and have a higher decay rate than at prototype scale. Heller (2008) found analytical approaches to quantify viscous wave attenuation inapplicable to impulse waves, as their decay process is mainly affected by turbulence, frequency dispersion, and air entrainment. These processes are not taken into account by the analytical expressions so that wave attenuation was strongly underestimated. In addition, Fritz (2002) and Heller (2008) discussed the effect of viscosity on the underwater slide runout distance, which decreases relatively for smaller scale models. However, Heller *et al.* (2008) and Heller (2008) found this effect to be negligible, as the generation of the primary wave is terminated before the slide has reached its final runout distance.

The ratio of inertial to surface tension forces is accounted for by the Weber number W (Eq. 3.14) (Hughes 1993). Regarding the generation and propagation of impulse waves, the surface tension affects the process of air entrainment and the wave celerity (Heller 2008). While the effect on the wave celerity is less than 1 % for still water depths $h \geq 0.02$ m and wave periods $T \geq 0.35$ s (Hughes 1993, Novak *et al.* 2010), impact crater formation (Fritz *et al.* 2003) and its collapse as well as wave breaking are influenced by the entrainment and detrainment of air bubbles, as shown in Figure 3.3. Especially the size of air bubbles and consequently the bubble-rise velocity is affected by the scale ratio (Novak *et al.* 2010). Furthermore, slide impact onto the free water surface may be abstracted as a volumetric current, which entrains air into the water. For impinging water jets, Kobus and Koschitzky

(1991) determined a critical velocity v_c between 0.8 and 1.0 m/s as inception limit for air entrainment.

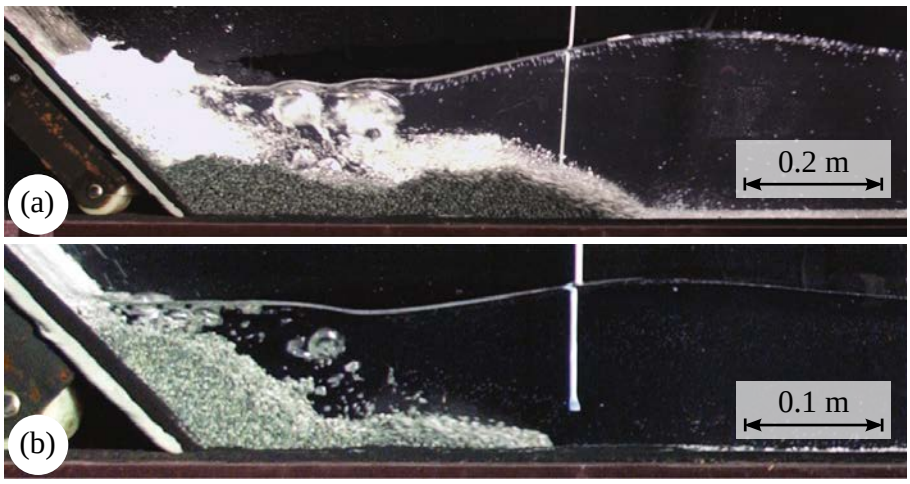

Fig. 3.3 Comparison of air entrainment and detrainment for two scale series tests at α = 45° with (a) F = 2.64, $S = 0.25$, $M = 1.36$, P = 1.26, R = 289,329, W = 5,345, and (b) F = 2.42, $S = 0.20$, $M = 1.27$, P = 1.02, R = 103,415, W = 1,336 (Heller *et al.* 2008, adapted from Heller 2008)

The Cauchy number C (Eq. 3.15) accounts for the ratio of inertia to elastic compression forces. Hydraulic laboratory experiments involving free water surfaces are generally considered incompressible (Hughes 1993). This applies also for the water phase of landslide generated impulse waves, since landslide velocities V_s are substantially slower than the sonic velocity of water (Heller 2008). However, the wave generation process features an air-water mixture (Figure 3.3) and the rapid impact of an object onto the free water surface causes the creation of an air cavity with low pressure. Abelson (1970) investigated the latter effect and found atmospheric pressures in the cavity for vertical impact velocities up to 10 m/s. Above this threshold, the pressure inside the cavity decreased linearly with increasing impact velocity. While slide impact velocities V_s at laboratory scale range beneath this threshold, observed landslides at prototype scale reached $V_s \approx 150$ m/s (Erismann and Abele 2001).

While isolated scale effects are assessed by analogy with similar hydraulic processes, the complexity of landslide generated impulse waves and the quantification of related scale effects are challenging in hydraulic experimentation. Therefore, Heller *et al.* (2008) conducted scale family experiments to overcome these constraints and determined the following lower boundaries for the Reynolds and the Weber number as

$$\mathsf{R} \geq 3 \cdot 10^5 \tag{3.16}$$

$$\mathsf{W} \geq 5{,}000. \tag{3.17}$$

As a rule of thumb, scale effects due to viscous and surface tension forces are negligible for still water depths $h \geq 0.2$ m (Heller *et al.* 2008) so that all experiments of the present study were conducted above this limit (Table 3.1). Still, the Cauchy number C of the air phase and hence the pressure within the impact crater is not taken into account. Although pressure effects may not be adequately reproduced in hydraulic laboratories, the validation of the laboratory experiments against large scale experiments or prototype impulse wave events allows for taking these into account ex post (Section 5.6).

3.3 2D wave channel

3.3.1 Experimental setup

The experiments with mesh-packed slides were conducted in a rectangular wave channel. The experimental setup, consisting of the channel and a pneumatic landslide generator, was designed by Fritz (2002) and purpose-built for investigating landslide generated impulse waves. The setup was also used for the experiments of Zweifel (2004) and Heller (2008). The channel has a length of 11 m, a width of 0.50 m and a height of 1 m (Figure 3.4). The front sidewall of the channel consists of glass windows, while the back sidewall as well as the end plates are made of steel. In the section where the slides impact the water body the bottom of the channel is also made of steel. This section comprises a third of the total channel length. The remaining two-thirds of the bottom are made of glass, allowing for laser application from below. However, no laser-based measurement techniques were used in this work. A wave absorber was placed at the end of the channel.

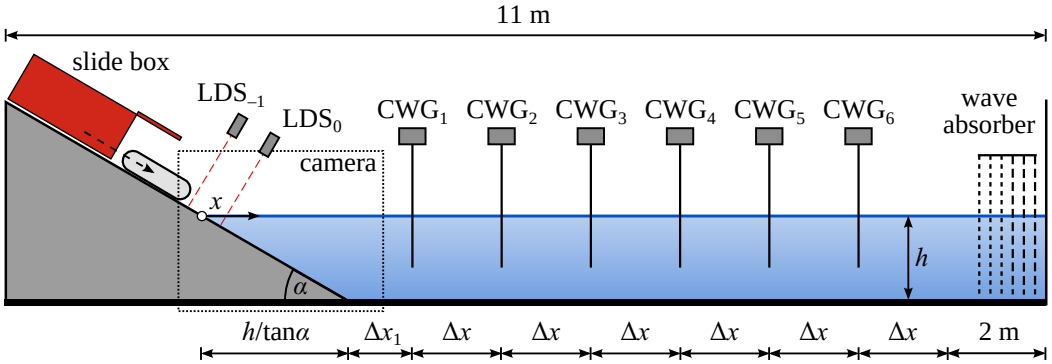

Fig. 3.4 Experimental setup and positioning of six capacitance wave gauges (CWG) along 2D wave channel with spacing $\Delta x_1 = 1.13$ m and $\Delta x = 0.71$ m for $\alpha = 30°$; $\Delta x_1 = 1.13$ m and $\Delta x = 1.00$ m for $\alpha = 45°$; and $\Delta x_1 = 1.27$ m and $\Delta x = 1.06$ m for $\alpha = 60°$

The impulse waves were generated with a pneumatic landslide generator (Fritz and Moser 2003). The generator was developed to independently vary the key slide characteristics, e.g. slide velocity, mass, or thickness. It consists of a rig structure featuring an inclinable sliding plane and a movable slide box. The general wave generation sequence applied for

this work involved three steps: First, the slide box was moved to its upper start position, filled with the slide, and closed. Second, the slide box was pneumatically accelerated at a rate larger than apparent gravity. During acceleration the flap at the bottom end of the box was opened. Third, the slide box was, again pneumatically, decelerated. Due to deceleration, the slide material was released, moved down the sliding plane, and eventually impacted the water surface. For experimental runs with low slide impact velocities, the slide box was moved to its lowest position and only the flap was opened to release the slide, which was then accelerated only by gravity.

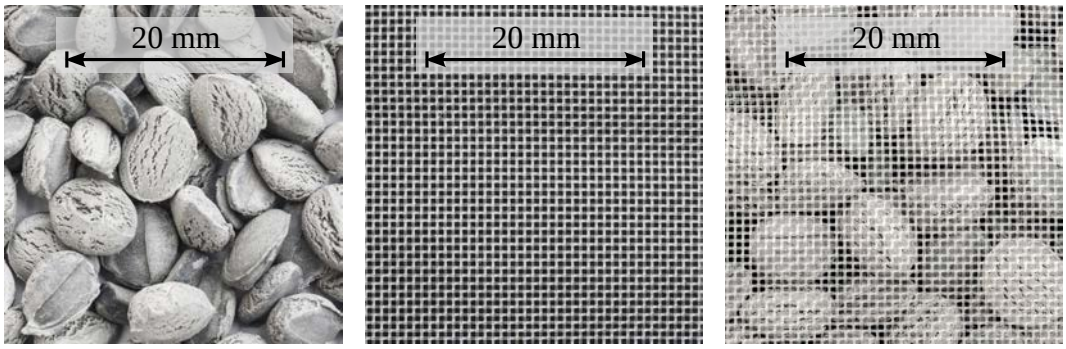

Fig. 3.5 (a) Granular material, (b) mesh fabric, and (c) mesh-packed slide (Photos: A. Schlumpf, VAW)

The slides were composed of granular material loosely filled in bags made of mesh material (Figure 3.5). The granular material had a grain (subscript g) diameter $d_g = 8$ mm, a grain density $\rho_g = 2{,}429$ kg/m^3, a bulk slide density $\rho_s = 1{,}338$ kg/m^3, and was made of 87 % $BaSO_4$ and 13 % PP (Heller 2008). Sifting media (SEFAR NYTAL PA-38GG-500, Sefar AG, Heiden, Switzerland) with a mesh opening of 500 μm and a porosity of 47 % was used as mesh fabric for the bags. Two bag sizes were fabricated to vary the form of the initial slide geometry. Form $f4$ (Heller 2008) had a box length of 0.3 m and a thickness of 0.118 m. Form $f6$ had a box length of 0.6 m and a thickness of 0.059 m.

3.3.2 Instrumentation

Three measurement techniques were used to capture the wave generation and propagation process: Laser Distance Sensors (LDS) for the slide characteristics prior to impact, a camera for the impact zone, and Capacitance Wave Gauges (CWG) for the wave propagation zone. The impact velocity and the slide thickness were measured with two LDS, mounted perpendicularly to the sliding plane (Figure 3.4). In contrast to experiments with free granular slides, the impact velocity of the mesh-packed slides was not measured as a slide centroid velocity, but as the velocity of the slide front under dry conditions without water in the channel. The LDS had a response time of 10 ms (Fritz 2002). The slide impact zone was captured with a pco.edge 3.1 camera (PCO AG, Kehlheim, Germany) and a Zeiss Distagon T 2/28 lens (Carl Zeiss AG, Oberkochen, Germany) to qualitatively

describe the slide deformation process during underwater slide propagation. The wave propagation and decay process was measured with six CWG positioned along the channel axis (Figure 3.4). CWG are point gauges for tracking the evolution of the free water surface at a single position. They are well suited for steep waves. However, they are subject to tailing effects due to a delayed drawdown of the thin water film after passage of a wave crest as shown by Fuchs (2013) and Evers and Hager (2015b), which potentially causes an underestimation of the wave trough following a wave crest. To minimise this tailing effect, the CWG were treated with detergent prior to each experimental run. More information on the instrumentation of the 2D wave channel is available in Fritz (2002), Zweifel (2004), and Heller (2008).

3.4 3D wave basin

3.4.1 Experimental setup

A 4.5 m by 8 m wave basin with a height of 0.75 m was built for investigating the spatial propagation characteristics of landslide generated impulse waves (Figure 3.6). Since the videometric measurement system (Section 3.4.2) applied for tracking the spatial wave features required an opaque white water surface, deionized (DI) water was filled into the basin and mixed with titanium dioxide (TiO_2), as described in Section 2.4. To reduce the rate of reionization of the TiO_2/DI-water suspension caused by dissolution from the side walls and bottom, the basin was coated with PolyVinyl Chloride (PVC) sheets. Porous filter foam mats were placed vertically into the basin at one of the short side walls (Figure 3.7). The decay time from irregular wave movement after an experiment to still water conditions for the next experiment was thereby substantially reduced.

Fig. 3.6 Multi exposure picture of landslide generated impulse wave under clear-water conditions (Photo: A. Schlumpf, VAW)

A mobile chute with an inclinable sliding plane, a release box, and guidance walls was designed as wave generator (Figures 3.6 and 3.7). The sliding plane as well as the the release box and guidance walls were made of smooth PVC with an estimated sand roughness coefficient <0.001 mm. The supporting structure of the mobile chute was made of aluminum profiles. The sliding plane was inclinable to impact angles α of 30°, 45°, 60°, and 90° and had a total length of 2.8 m. Mesh-packed slides as described in Section 3.3.1 were placed into the release box. Due to the opaque TiO_2/DI-water suspension contained in the wave basin, the application of mesh-packed slides meant a significant improvement for retrieving the slide mass after an experimental run. The position of the release box was adjustable along the sliding plane to vary the slide impact velocity onto the water surface. Note that slides were only accelerated due to gravity. The release box allowed for a predefinition of the slide geometry by adjusting the slide thickness s at 0.06 m and 0.12 m as well as the slide width b between 0.25 m and 1.00 m (Figure 3.7). In addition to the two slide bag forms of the 2D wave channel tests, two more mesh bags were used, allowing for slide widths b of 0.25 m and 1.00 m at a slide thickness s = 0.06 m. The slide was released from the box by manually opening the flap at its bottom.

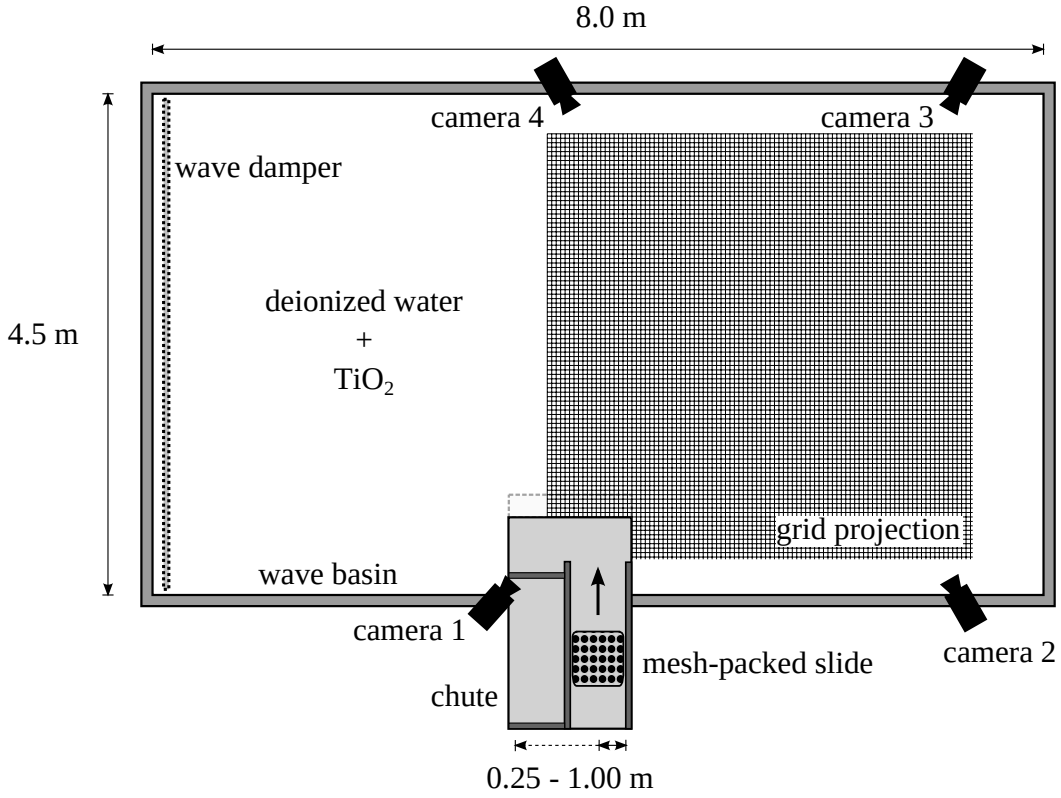

Fig. 3.7 Experimental setup of 3D wave basin with camera positions of videometric measurement system

3.4.2 Instrumentation

3.4.2.1 Slide impact velocity

While the geometric slide properties (slide thickness, slide width) were predefined by the release box and the corresponding mesh bags, the slide impact velocity had to be measured. As for the experiments in the 2D wave channel (Section 3.3), only the slide front velocity was measured. Since the slide deformation during subaerial acceleration was negligible due to the mesh bags, the slide centroid velocity was equal to the slide front velocity. However, unlike in the 2D experiments, the slide velocity was measured above the water surface. Laser Light Barriers (LLB) OHDK 14 (Baumer Electric AG, Frauenfeld, Switzerland) were mounted perpendicular to the sliding plane. The short response time <0.5 ms of the sensor allowed for a measuring section with a distance of 0.1 m between the first and the second LLB. The impact velocity V_s was determined as the length of the measuring section divided by the time difference between the two LLB. The acquisition rate of the sensor signal was set to 1,000 Hz, resulting in a measurement accuracy of approximately ± 5 % for a maximum measured slide impact velocity V_s of 4.76 m/s. The LLB measuring section was set right above the still water surface as shown in Figure 3.8.

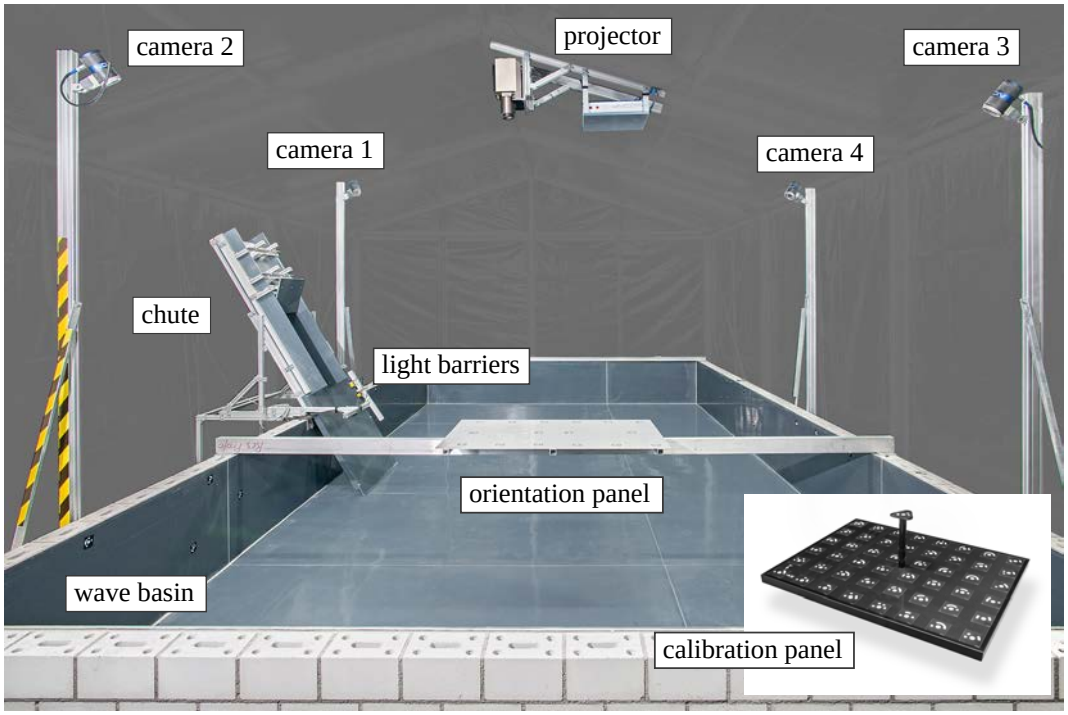

Fig. 3.8 Wave basin with components of the videometric measurement system (Photos: A. Schlumpf, VAW)

3.4.2.2 Water surface tracking

The wave movement of the water surface during a test run was tracked with a videometric measurement system. The commercially available *ProSurf*-system (AICON 3D Systems

GmbH, Braunschweig, Germany) allows to measure the spatial positions of projected grid intersections on arbitrary surfaces. To convert a commonly transparent water surface into a white opaque projection screen, deionized (DI) water was mixed with 4 kg/m^3 titanium dioxide (TiO_2), which had negligible effects on water viscosity and the surface tension, as specified by Przadka *et al.* (2012) (see also Section 2.4). A regular grid pattern with 79 $\times$ 79 intersections including the boundaries was projected onto the opaque water surface, thereby defining the measuring zone. A frame tent was built around the experimental setup to keep out scattered light. Depending on the still water depth, the rectangular measuring zone had a lateral length between 3.5 and 3.8 m with a corresponding grid spacing between 4.4 and 4.8 cm. The *ProSurf*-system applied in this work comprised four cameras with a resolution of 1,600 $\times$ 1,200 pixels, that were positioned around the measuring zone of the wave basin (Figures 3.7 and 3.8). The cameras were synchronized and powered by a control box. Figure 3.9 shows four synchronized shots of an experimental run. The image acquisition rate of the system was set to 24 Hz for sufficient temporal resolution.

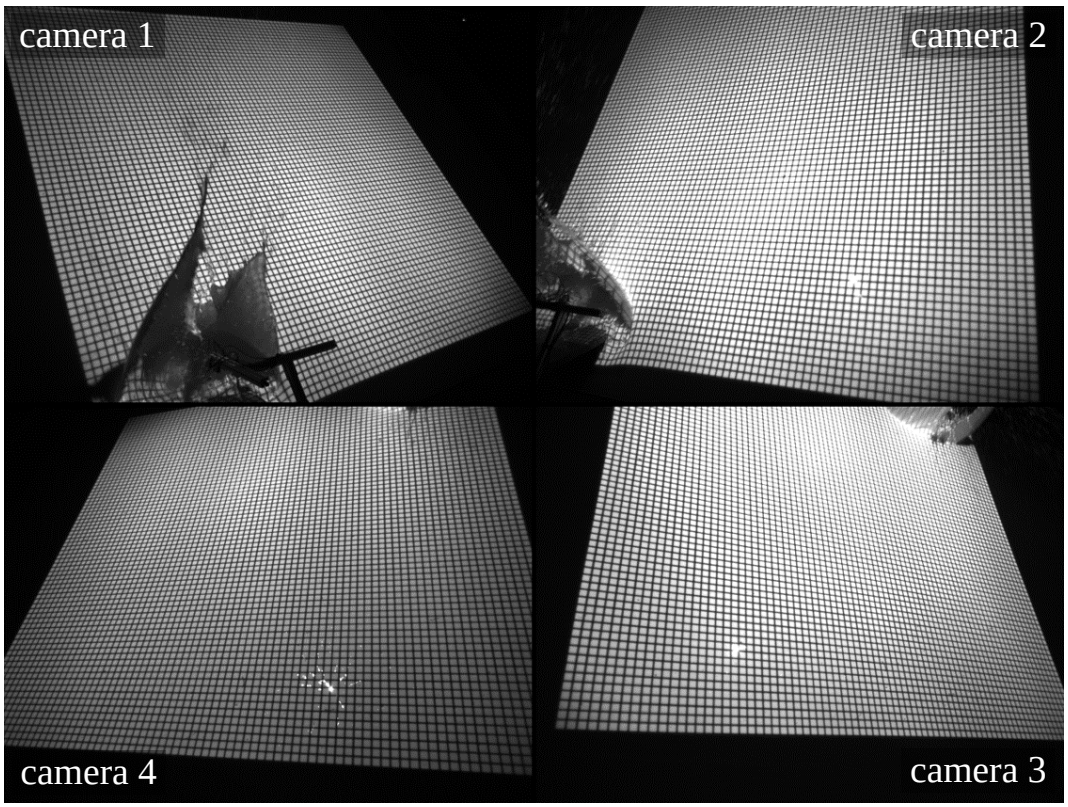

Fig. 3.9 Synchronized shots by four cameras positioned around projected grid pattern

Figure 3.10 presents the functional principle of the videometric system. The position and orientation of the measurement cameras were spatially referenced. Therefore, each pixel of a camera shot constitutes a vector in space. The pixels of the same grid intersection shot by two different cameras represent two vectors crossing each other, thus defining a point in space. When this measurement principle for a single intersection is extended

to the entire grid projection a point cloud with a theoretical maximum of 6,241 points representing the free water surface at a specific instant of time results. In practice, the actual number of tracked grid intersections was lower due to strongly distorted parts of the free surface, where the grid pattern was untraceable or appeared covered for one or more cameras. Nevertheless, the application of four cameras yielded satisfactory results for productive data processing (Section 3.4.3). Prior to measuring, the cameras' positions and orientations had to be calibrated: An orientation panel with precalibrated measuring marks was recorded; in addition, an internally referenced calibration panel was recorded 50 times by all four cameras at different locations within the measuring zone. The orientation and calibration measurement steps before an experimental series are shown in Figure 3.11. In case the position and orientation of the cameras had changed due to intended adjustment or accidental contact, the two measurements were recorded again.

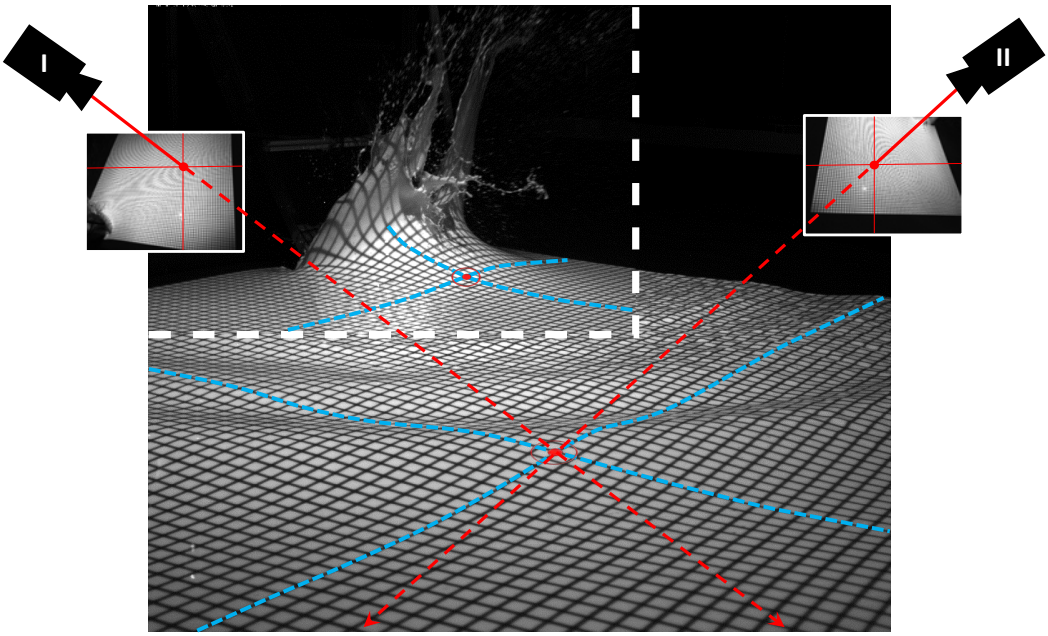

Fig. 3.10 Functional principle of videometric water surface tracking; the background image combines two shots at different time steps separated by a white dashed line

(a) (b) (c)

Fig. 3.11 Shots by camera 1 of (a) orientation measurement; (b) calibration measurement; (c) measurement of experimental run

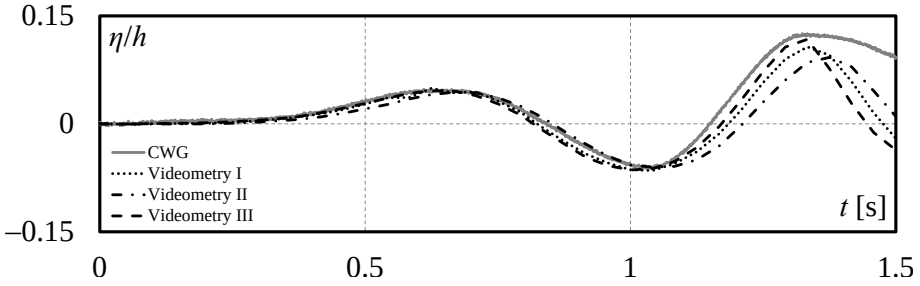

Fig. 3.12 Comparison of capacitance wave gauges (CWG) and three videometric measurements

Frank and Hager (2014) discussed the measurement accuracy of the videometric system and found absolute deviations of <2 mm to point gauge data for a solid, plane surface as well as for the mild slopes of a fixed, dry dike breach topography. Evers and Hager (2015b) compared the measured displacements of the water level tracked by the videometric system to CWG. Figure 3.12 shows time-variation curves for one CWG and three videometric measurements. While the first wave crest and trough are properly captured, deviations are apparent for the second wave crest. However, these deviations also apply to the three videometric measurements. In addition, the CWG measurements show the tailing effect as discussed in section 3.3.2. These tailing effects appear in Figure 3.12 after $t = 1.3$ s involving a substantially lower gradient of the draw down curve for the CWG measurement.

The water surface profiles of five experimental runs, which were repeated with identical preset parameters, are shown in Figure 3.13 for three instants of time t at 0.5, 1.5, and 2.5 s. While the measured water surface profiles feature larger deviations within the vicinity of the slide impact location at $r = 0$ m, wave crests and troughs are captured sufficiently detailed for larger propagation distances. Note that deviations between the individual runs are not necessarily related to inaccuracies of the measurement system, but are also influenced by the repeatability of the wave generation process; e.g. the slide impact velocities V_s vary within the measurement accuracy of the laser light barriers between 4.35 and 4.55 m/s (see Section 3.4.2.1). Figure 3.13 also accounts for a test repeatability within an acceptable tolerance. Since a free water surface does not allow for a one-to-one comparison with a calibrated contour as conducted by Frank and Hager (2014) for dike breaches, the measurement accuracy for water surface tracking was estimated to ± 1 mm, based on the previous findings.

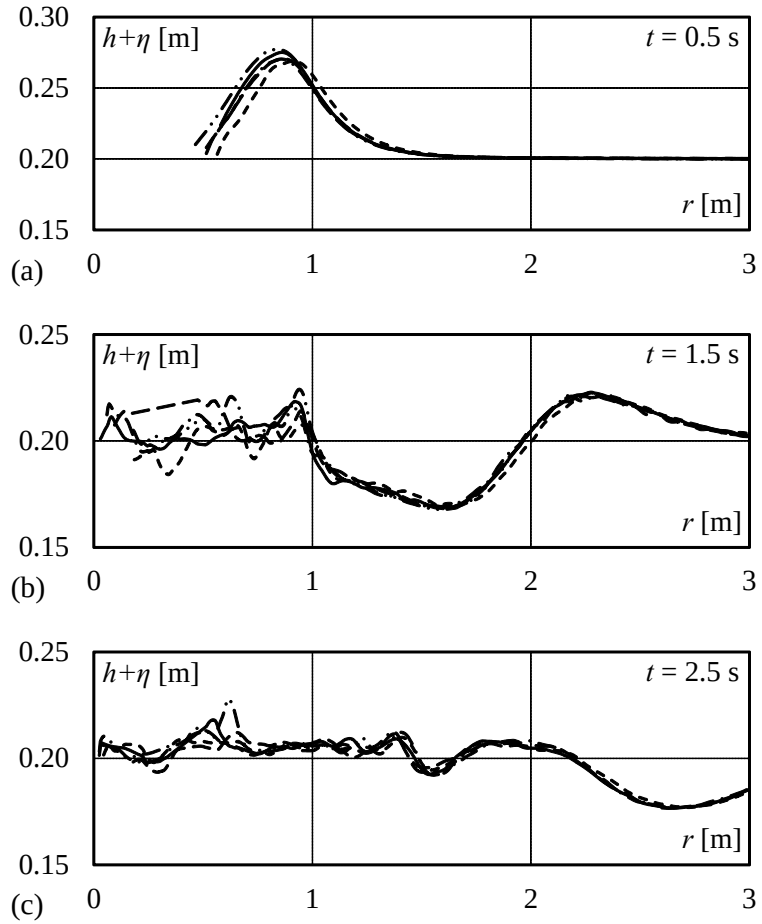

Fig. 3.13 Water surface profiles of five similar experimental runs with slide impact velocities V_s between 4.35 m/s and 4.55 m/s, slide mass $m_s = 20$ kg, slide thickness $s = 0.06$ m, slide width $b = 0.50$ m, and slide impact angle $\alpha = 60°$ for wave propagation angle $\gamma = 0°$

3.4.3 Data processing

The videometric measurement system provides point clouds, which contain discrete points on the free water surface, at a frame rate of 24 Hz. To obtain meaningful information on the spatial and temporal evolutions of the wave train and its main characteristics, including e.g. wave amplitudes, the point clouds were processed with a semi-automatic evaluation scheme developed in Python. The wave characteristics were spatially referenced in a polar coordinate system with the slide impact location as its pole (see also Section 2.3.3).

In a first step, the point clouds were extracted from the synchronized shots of the four cameras around the wave basin. Figure 3.14(a) shows a screenshot of the *ProSurf*-software with a shot taken by camera 1 and an overlay of detected grid intersection points. For tracking the grid intersections, the software requires the location of the same intersection in the frames of two cameras as a common reference. After an intersection has been defined as a starting point, the software's proprietary algorithm automatically identifies neighboring grid intersections on a step-by-step basis, taking into account all four cameras.

Although the software features a function for an automatic starting point recognition, most of the starting points had to be defined manually for each synchronized quadruple shot. After detection, the point data were exported in Cartesian coordinates as an ASCII-file.

The point cloud is plotted in Figure 3.14(b) in planar *xy*-coordinates with the slide impact location as origin. Through cubic interpolation onto a regular data grid, the z-coordinates are added as attributes of a contour plot in Figure 3.14(c). The data grid has a cell width of 5 mm and interpolated areas, which are not covered by the point cloud, are masked. The contour plot provides a continuous representation of the water surface. In Figure 3.14(d) a polar coordinate system with the slide impact location as its pole is introduced. Between 0° and 90° a total of 91 slices are extracted at a regular step width of 1°.

Figure 3.14(e) shows the plot of the 0° slice extracted from the contour plot. The slide impact location is at $r = 0$ m and the Still Water Level (SWL) at $z = 0.2$ m. Besides the amplitudes and positions of the first wave crest, the first wave trough, and the second wave crest, the crossings of the water surface with the still water level were tracked as primary wave features. The tracking procedure for the primary wave features was separated into automated 8 steps:

1. Wave crests, i.e. positive peak amplitudes, of all 91 slices between 0° and 90° were detected.
2. Radii of the wave crests were clustered according to their distance from the impact location. Depending on their position within the wave train, the clusters were marked first or second wave crest.
3. Radii of each cluster were averaged with a linear smoothing function to approximate the expected location of the wave crest.
4. Locations of water level maxima within a standard search range of ± 0.1 m around the linear function were tracked, yielding the locations of the first and second wave crests.
5. First wave trough was tracked as the minimum between the first and second wave crest.
6. Initial uplifting of the water level caused by the approaching first wave crest, i.e. the first intersection with the still water level, was tracked at the location where the water level exceeded an absolute threshold equal to the estimated measurement accuracy of 1 mm (Section 3.4.2.2) above the still water level.
7. Second intersection with the still water level was tracked between the first wave crest and the first wave trough.
8. Third intersection with the still water level was tracked between the first wave through and the second wave crest.

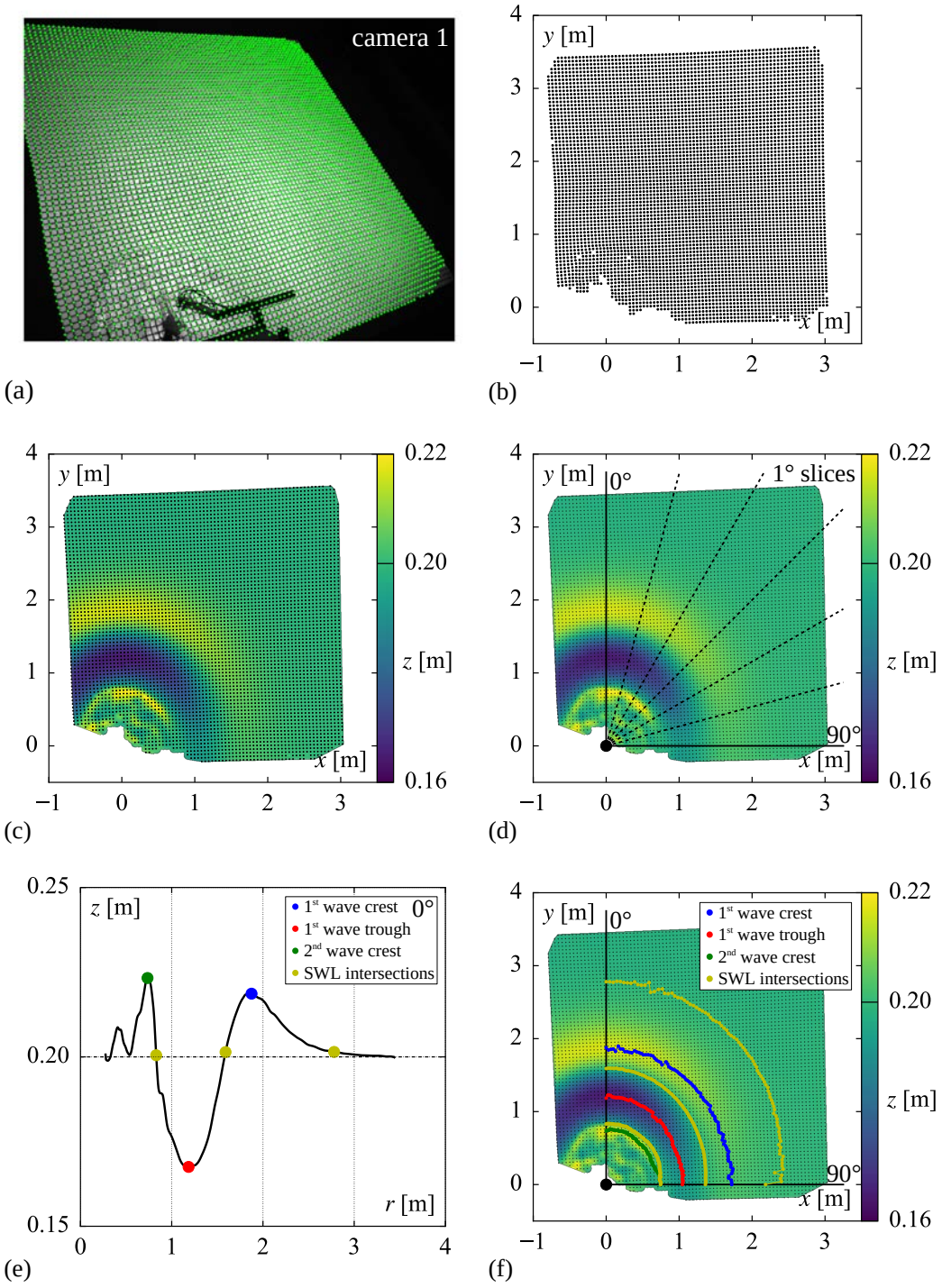

Fig. 3.14 Data processing steps: (a) *ProSurf* grid detection, (b) planar point cloud, (c) interpolated contour plot, (d) slice extraction, (e) wave feature detection, and (f) tracked wave features

A spatial wave train with all six primary wave features for angular coordinates between 0° and 90° is shown in Figure 3.14(f). The step width for slicing the contour plots was set to 1° to obtain enough data points for a robust wave feature tracking procedure, since a

high angular resolution allowed for the exclusion of erroneously tracked wave features and outliers, while maintaining a sufficient number of data points at the same time. The two iterations for tracking the wave crest locations, combining a peak detection and subsequent search window approach, were applied, since the the peak detection approach itself was not sensitive enough to distinguish between small wave amplitudes and splash water due to the slide impact especially for angular coordinates >70°.

The propagation distances within the wave basin were limited and waves were reflected by the vertical sidewalls, affecting the wave field of the outgoing impulse wave train. The next step in data processing involved the exclusion of primary wave features affected by wave reflection. The initial uplifting of the water level was the first wave feature to reach the sidewalls and causing disturbance to the outgoing wave field after reflection. Its motion after leaving the measurement area and reflection was therefore extrapolated. If the extrapolated position of the initial uplifting overlapped with succeeding wave features, these were excluded from the analysis. The extrapolation involved the propagation velocity as well as the residence time at the vertical sidewall. The propagation velocity of the initial uplifting was defined as the propagation distance of its last position captured within the measurement area over the time elapsed after slide impact. The residence time t_r of the wave at the vertical sidewall was estimated after Chen *et al.* (2015) with

$$\frac{t_r}{\tau} = \frac{2}{\sqrt{3}} \left(\ln\left(\frac{\sqrt{3}+1}{\sqrt{3}-1} \right) \varepsilon^{-1/2} + \frac{1}{8} \ln\left(\frac{\sqrt{3}+1}{\sqrt{3}-1} \right) \varepsilon^{1/2} \right). \tag{3.18}$$

The residence time t_r is made dimensionless with $\tau = \sqrt{h/g}$ and contains the relative wave amplitude $\varepsilon = a_{c1}/h$ with first wave crest amplitude a_{c1}, still water depth h, and gravitational acceleration $g = 9.81\ \mathrm{m/s^2}$.

While primary wave features are directly trackable in the wave profile slices as shown in Figure 3.14(e), secondary wave features, including wave height, wave period, and wave celerity, are deduced from the former. For the first wave height position, the first wave crest was taken as the reference position. The wave crest amplitude and the linearly interpolated amplitude of the subsequently passing first wave trough at the same position were summed to obtain the first wave height. The same procedure was applied to obtain the first wave period with the third still water level intersection as reference position and the time step of the first still water level intersection linearly interpolated thereupon. The wave celerities for the first and the second wave crest were determined as the distances between the wave crest positions 0.25 s prior to the reference position and 0.25 s after over a time interval of 0.5 s.

The last data processing step involved the exclusion of tracked data below measurement accuracy. In Section 3.4.2.2, the accuracy of the videometric system was estimated to ± 1 mm. Since all tracked wave features were directly or indirectly deduced from wave

amplitude information, wave crests and troughs with measured amplitudes <2 mm were excluded from the data analysis.

3.5 Summary

Two hydraulic scale models for investigating landslide generated impulse wave propagation were described: a 2D wave channel and a 3D wave basin setup. The 2D setup allowed to test whether mesh-packed slides create similar wave features compared to free granular slides. In the 3D setup, the spatial impulse wave propagation was modelled. Both models were based on Froude similitude. A dimensional analysis yielded 12 independent governing parameters: Slide impact velocity, bulk slide volume, bulk slide density, slide thickness, slide width, slide impact angle, still water depth, water density, gravitational acceleration, radial wave propagation distance, wave propagation angle, and time. These were reduced to 9 dimensionless governing parameters. Potential scale effects are discussed and the experiments complied with a lower threshold of 0.2 m for the still water depth. A videometric measurement system was applied to track the water surface of the 3D wave basin during an experimental run. Subsequent data processing of the water surface contours yields key wave characteristics of the spatial wave train, including wave crest and trough amplitudes, wave height, and wave period.

4 Results

4.1 Overview

Chapter 4 consists of two parts, describing the results of the 2D wave channel experiments as well as the 3D wave basin experiments. The first part provides the proof-of-concept that mesh-packed slides generate key wave characteristics, including wave amplitude and height, similar to free granular slides (Section 4.2). In the second part, a phenomenological description of the hydraulic processes related to the spatial propagation of landslide generated impulse waves is given, based on the temporal evolution of the water surface of selected experimental runs (Section 4.3.2). Subsequently, a comparative study in Section 4.3.3 discusses the applicability of existing equations, presented in Chapter 2, for predicting the measured heights of the first wave within the wave train. On this basis, dimensionless fit equations for the crest and trough amplitudes, height, period, and celerity of the first wave as well as the crest amplitude and celerity of the second wave are presented. All wave characteristics are construed from the governing dimensionless slide parameters (Section 3.2.2). A detailed discussion of the results is provided in Chapter 5.

4.2 2D wave channel

4.2.1 Experimental parameter ranges

The experimental parameter ranges for the 2D experiments are listed in Table 4.1. The slide impact velocity V_s, the bulk slide mass m_s, the slide thickness s, the slide impact angle α, and the still water depth h were systematically varied in the experiments. The slide width b corresponds to the channel width of 0.5 m. The streamwise coordinate is x. The following wave characteristics were included into the analysis as target variables: the maximum wave crest amplitude a_M and wave height H_M, the wave amplitude $a(x)$ and wave height $H(x)$ of the first wave, and the celerity of the first wave crest c_{am}. In total, 42 experiments with mesh-packed slides were conducted and analysed.

Table 4.1 Governing experimental parameter ranges for plane impulse waves

Parameter [unit]	Test range	Dimensionless parameter	Test range
V_s [m/s]	1.2 - 9.2	$\mathsf{F} = V_s/\sqrt{gh}$	0.70 - 5.36
m_s [kg]	19.5 - 20.1	$M = VD = m_s/\rho_w bh^2$	0.24 - 1.01
s [m]	0.062 - 0.145	$S = s/h$	0.16 - 0.65
α [°]	30 - 60	α	30 - 60
h [m]	0.20 - 0.40	-	-
-	-	P	0.26 - 2.78

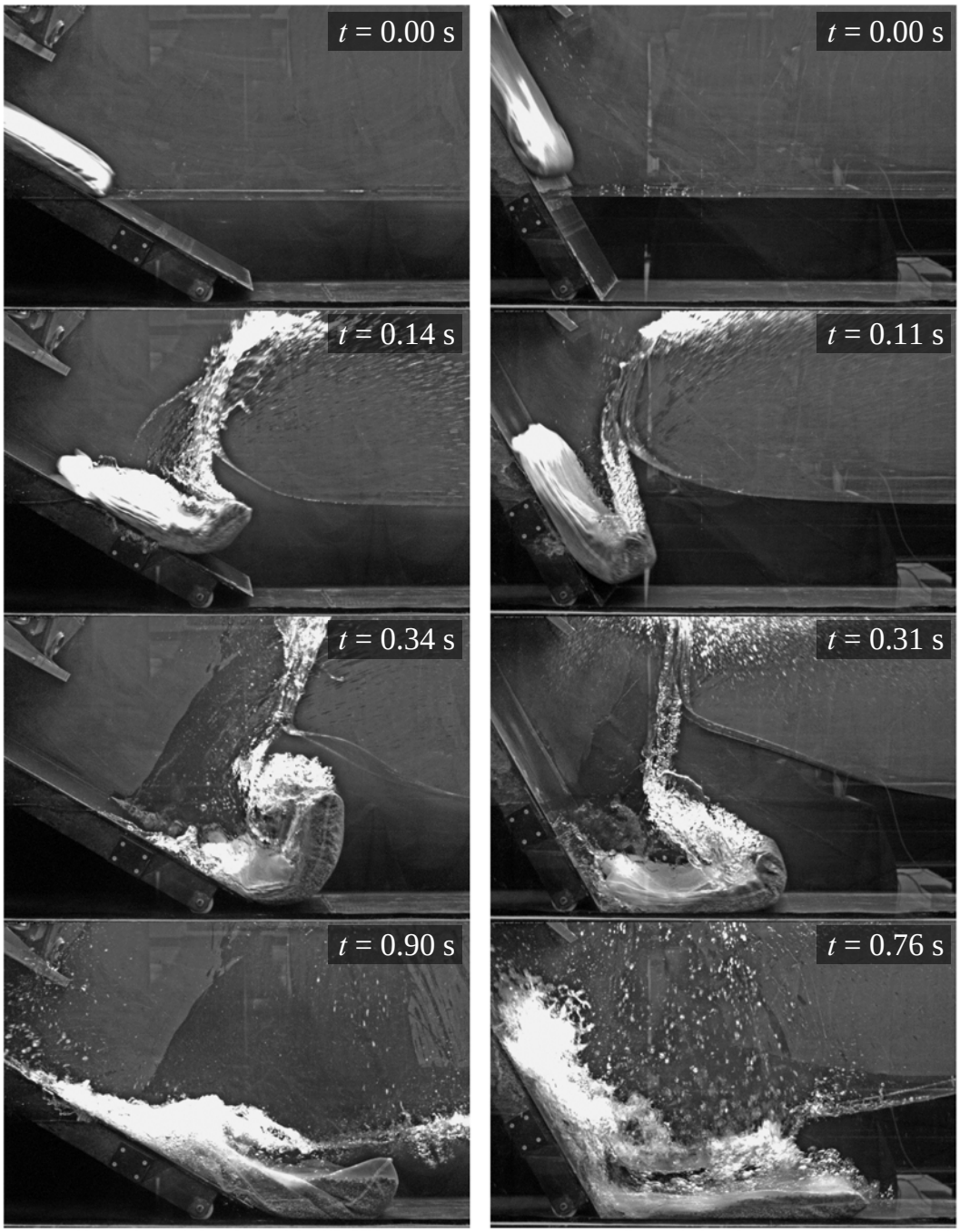

Fig. 4.1 Photographs at various stages of 2D wave generation process with mesh-packed slides at $h = 0.3$ m; (a) $\alpha = 30°$ with $\mathsf{F} = 2.27$, $S = 0.23$, $M = 0.45$, and $\mathsf{P} = 0.84$; (b) $\alpha = 60°$ with $\mathsf{F} = 3.03$, $S = 0.21$, $M = 0.45$, and $\mathsf{P} = 0.90$ (Evers and Hager 2015a)

4.2.2 Slide impact and wave generation process

Figure 4.1 shows photographs at various stages of the slide impact and wave generation process for slide impact angles $\alpha = 30°$ and 60°. Fritz *et al.* (2003) observed compaction and strong deformation of free granular slides after the impact onto the still water surface and during their underwater movement to the channel bottom. Depending on the slide impact angle α, the mesh-packed slides are both bent and lifted upwards after impact. These effects are more pronounced for $\alpha = 30°$ than for 60°. After impact, the slide thickness s is significantly increased, resembling the mechanisms of compaction and deformation of free granular slides. In contrast, no significant slide deformation occurs along the sliding plane before impact. Further distinct impulse wave generation features observed by Fritz *et al.* (2003) include the process of flow separation as well as the formation of an air cavity referred to as the impact crater. Both features are also observable in Figure 4.1 for mesh-packed slides. After $t = 0.34$ s (30°) and 0.31 s (60°), respectively, the impact craters collapse, causing massive air entrainment.

4.2.3 Maximum wave amplitude and height

Figure 4.2 shows the measurement results of the relative maximum wave crest amplitude $A_M = a_M/h$ and wave height $Y_M = H_M/h$ versus P for the experiments with mesh-packed slides. The maxima are analysed independently from their position within the wave train and along the propagation distance. Most maxima were observed at the first wave crest and were already fully developed at the first capacitance wave gauge CWG_1. The data of both wave maxima scatter with $\pm 30\%$ of Eqs. (2.5) and (2.7) for free granular slides by Heller (2008). For $\mathsf{P} \leq 1$, the equations tend to overestimate the actual measured values. Both findings also apply to the plots based free granular slide experiments by Heller (2008). The coefficients of determination are $R^2 = 0.82$ and 0.85 for maximum relative wave amplitude and height, respectively, compared to $R^2 = 0.89$ and 0.85 for free granular slides (Heller 2008).

Note the effect of the slide impact angle α on A_M and Y_M. The maxima are predominantly scattered within the area between the curves of Eqs. (2.5) and (2.7) an the corresponding -30% curves for $\alpha = 60°$. For $\alpha = 45°$, the maxima are narrowly scattered along their corresponding equations. For $\alpha = 30°$, the maxima scatter above the equations up to +30%. However, a good overall agreement of maximum impulse wave amplitude and heights between free granular and mesh-packed slides results from the experiments.

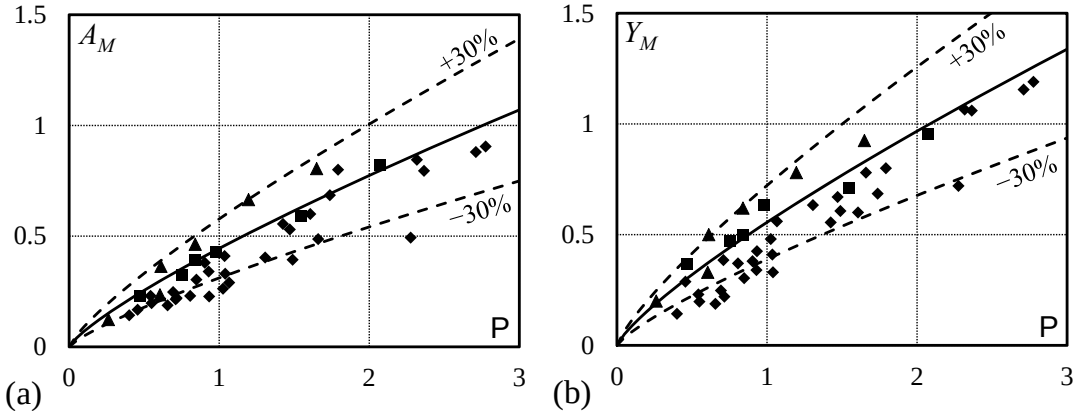

Fig. 4.2 2D mesh-packed slides' relative maximum wave (a) crest amplitude A_M with Eq. 2.5 (—) and (b) height Y_M with Eq. 2.7 (—) versus P for $\alpha = 30°$ (▲), 45° (■), 60° (♦) (Evers and Hager 2015a)

4.2.4 Wave amplitude and height decay

Only the first wave was considered for the evaluation of the wave crest amplitude and height decay. This applies also to wave trains, where these maxima occurred at the second wave crest. In Figure 4.3, the measured wave crest amplitudes $A(X) = a(x)/h$ (Eq. 2.8) and heights $Y(X) = H(x)/h$ (Eq. 2.9) are plotted versus $\mathrm{P}X^{-1/3}$. The relative propagation distance $X = x/h$ has its origin at the slide impact point (Figure 3.4). In contrast to the maxima A_M and Y_M, no immediate effect of the slide impact α results. For wave trains with $\mathrm{P}X^{-1/3} \geq 0.75$ at $X_{\mathrm{CWG_1}}$, an increase in wave amplitude and height is observed. These wave trains developed their maxima at $\mathrm{CWG_2}$. An increased undercut of the -30% curve for $A(X)$ in Figure 4.3(a) for $\mathrm{P}X^{-1/3} \leq 1$ applies also to the data of Heller (2008). This statement is valid for the data exceeding the +30% curves of $A(X)$ as well as $Y(X)$ for $0.5 \leq \mathrm{P}X^{-1/3} < 1$. Although the measured wave crest amplitude and height data of mesh-packed slides significantly exceeds and undercuts the $\pm 30\%$ scatter range for certain ranges of $\mathrm{P}X^{-1/3}$, this observation is also applicable to the data of Heller (2008) for free granular slides. The coefficients of determination are $R^2 = 0.71$ and 0.78 for relative wave amplitude and height decay, respectively, compared to $R^2 = 0.83$ and 0.84 for free granular slides (Heller 2008). A satisfactory overall agreement of the wave decay results from the experiments.

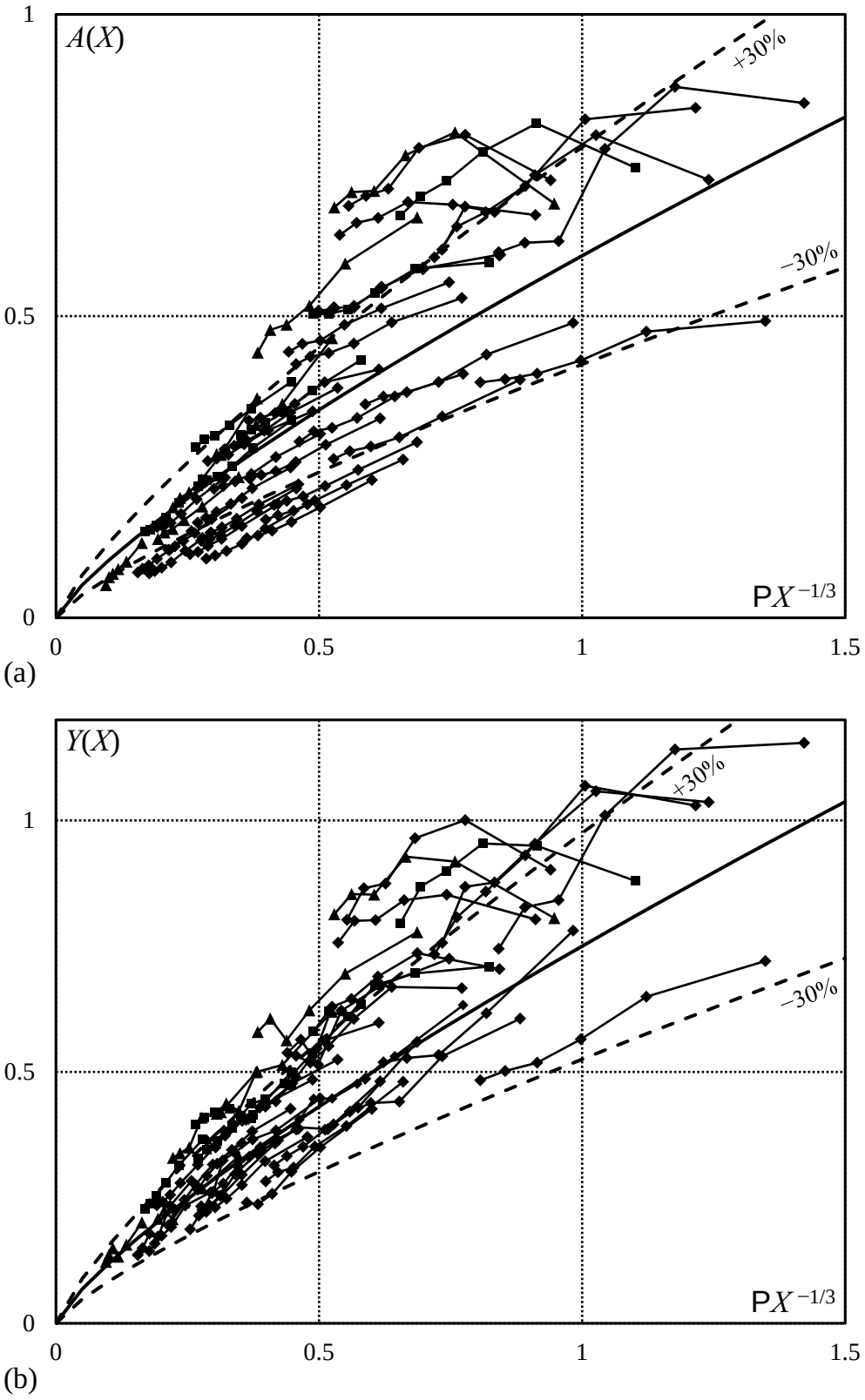

Fig. 4.3 2D mesh-packed slides relative wave (a) crest amplitude decay $A(X)$ with Eq. 2.8 (—) and (b) height decay $Y(X)$ with Eq. 2.9 (—) versus $PX^{-1/3}$ for $\alpha =$ 30° (▲), 45° (■), 60° (♦) (Evers and Hager 2015a)

4.2.5 Wave crest celerity

The wave amplitudes of the first wave crest between CWG_1 and CWG_6 were averaged to a mean wave amplitude a_m. In analogy to Heller (2008), the mean wave crest celerity c_{am} was determined as the distance between CWG_1 and CWG_2 over the runtime of the first wave crest. The relative celerities $c_{am}/(gh)^{1/2}$ of the first wave crest generated with mesh-packed slides shown in Figure 4.4 lie within the experimental scatter of free granular slides and reproduce Eq. (2.10) well. The coefficient of determination ist $R^2 = 0.95$, compared to 0.91 for free granular slides.

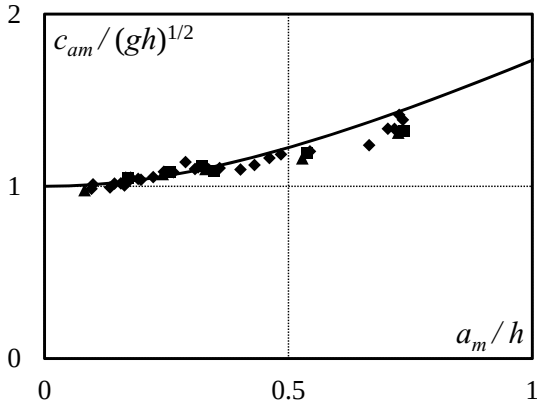

Fig. 4.4 2D mesh-packed slides mean relative crest celerity $c_{am}/(gh)^{1/2}$ with Eq. 2.10 (—) versus mean relative wave amplitude a_m/h for $\alpha = 30°$ (▲), 45° (■), 60° (♦) (Evers and Hager 2015a)

4.3 3D wave basin

4.3.1 Experimental parameter ranges

The experimental parameters and the measured dependent target variables for the 3D experiments are shown in Figure 4.5. The slide impact velocity V_s, the bulk slide mass m_s, the slide thickness s, the slide width b, the slide impact angle α, and the still water depth h were varied in the experiments (Table 4.2). The polar coordinates are composed of the radial wave propagation distance r and the wave propagation angle γ with the slide impact location center as origin (Figure 4.5). The following wave characteristics were included into the the analysis as target variables: the first wave crest and trough amplitudes a_{c1} and a_{t1}, the first wave height H_1, the first wave period T_1, the second wave crest amplitude a_{c2}, and the celerities of the first and the second wave crests c_{c1} and c_{c2}. In total, 74 experiments were evaluated.

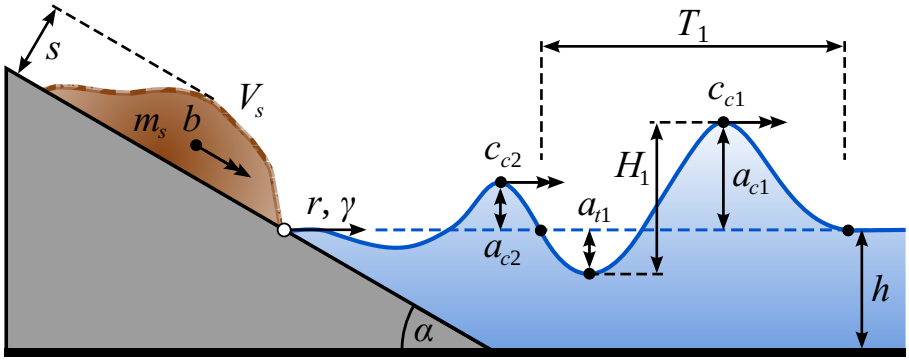

Fig. 4.5 Definition plot for spatial impulse waves with governing experimental parameters and measured dependent target variables

Table 4.2 Governing experimental parameter ranges for spatial impulse waves

Parameter	Test range	Dimensionless parameter	Test range
V_s [m/s]	0.72 - 4.76	$F = V_s/\sqrt{gh}$	0.40 - 3.40
m_s [kg]	10 - 40	$M = m_s/\rho_w bh^2$	0.25 - 1.00
s [m]	0.06 - 0.12	$S = s/h$	0.15 - 0.6
b [m]	0.25 - 1.00	$B = b/h$	0.83 - 5.00
α [°]	30 - 90	α [°]	30 - 90
h [m]	0.2 - 0.4	-	-
-	-	P	0.13 - 2.08

4.3.2 Water surface evolution

The videometric measurement system described in Section 3.4.2.2 yields a quasi-continuous contour representation of the water surface during an experimental run, allowing for detailed insight into its spatial evolution. A phenomenological description of spatial impulse wave generation and propagation is provided in the following for selected experiments (Table 4.3). This section focuses on the effects of three main slide parameters: slide impact velocity V_s, slide impact angle α, and slide width b. Water level profiles for the wave propagation angles $\gamma = 0°$, 45° and 90° were extracted from the contour plots. In addition, oblique camera views are presented for three experiments. The last part addresses the evolution of the crest profile of the first wave during propagation.

Table 4.3 Overview of governing parameters for selected experimental runs

Test	V_s [m/s]	m_s [kg]	s [m]	b [m]	α [°]	h [m]	Contour	Profile	Oblique view
A	1.06	20	0.06	0.50	45	0.4	Fig. 4.6	Fig. 4.7	-
B	2.94	20	0.06	0.50	45	0.4	Fig. 4.8	Fig. 4.9	-
C	1.79	20	0.06	0.50	30	0.4	Fig. 4.10	Fig. 4.11	Fig. 4.12
D	2.38	20	0.06	0.50	60	0.4	Fig. 4.13	Fig. 4.14	Fig. 4.15
E	3.85	20	0.06	0.50	90	0.4	Fig. 4.16	Fig. 4.17	Fig. 4.18
F	3.03	10	0.06	0.25	60	0.2	Fig. 4.19	Fig. 4.20	-
G	2.70	20	0.06	0.50	60	0.2	Fig. 4.21	Fig. 4.22	-
H	2.78	40	0.06	1.00	60	0.2	Fig. 4.23	Fig. 4.24	-

Effect of slide impact velocity

Figures 4.6 to 4.9 show the effect of the slide impact velocity V_s on the wave generation process for Test A with $V_s = 1.06$ m/s and Test B with $V_s = 2.94$ m/s at a fixed slide impact angle $\alpha = 45°$. All equations describing spatial impulse wave propagation discussed in Section 2.3.3 contain V_s as a major governing parameter. In Figure 4.6, contour plots of the water surface for Test A are presented. The y- and x-axes in Figure 4.6 are identical to the propagation angles $\gamma = 0°$ and 90°, respectively. The slide impact onto the still water surface was at $t = 0$ s. At $t = 0.375$ s, the water has been displaced by the slide and a wave crest is formed with its maximum amplitude at $\gamma = 0°$. Figure 4.8 shows at the same time step that in Test B a larger volume of water is displaced with a higher maximum amplitude. While this initial crest is located at $r = 0.4$ m for Test A in Figure 4.7, it is not yet completely formed at $r = 0.4$ m for Test B in Figure 4.9. At $t = 0.750$ s, the first wave trough emerges in Test A. In Test B, there are large gaps in the contour plots close to the slide impact location. This is caused by a strongly distorted water surface, which does not allow for a correct tracking of the projected grid intersections. Both wave trains further propagated at $t = 1.125$ s. The wave troughs are at $r = 0.8$ m for Test A and at $r = 1.0$ m for Test B. Despite its larger propagation distance, the wave trough amplitude is still larger for Test B. At $t = 1.500$ s, a steep second wave crest has formed for both tests with larger propagation distance for Test B again. The contour plots in Figures 4.6 and 4.8 show that the second wave crest is less uniform than the first one at the same location. In both experiments, the steep second wave crest flattens between $t = 1.875$ s and 2.250 s. In general, all wave amplitudes feature a higher magnitude in Test B than in Test A. As shown in the contour plots, the propagation pattern in both tests is approximately circular.

The comparison between Test A and B reveals that an almost triplication of the slide impact velocity V_s significantly increases the magnitude of the wave amplitudes. The impulse product parameter P includes this effect with the slide Froude number F . Furthermore, an increase of V_s moves the location where the first wave crest initially forms away from the slide impact location.

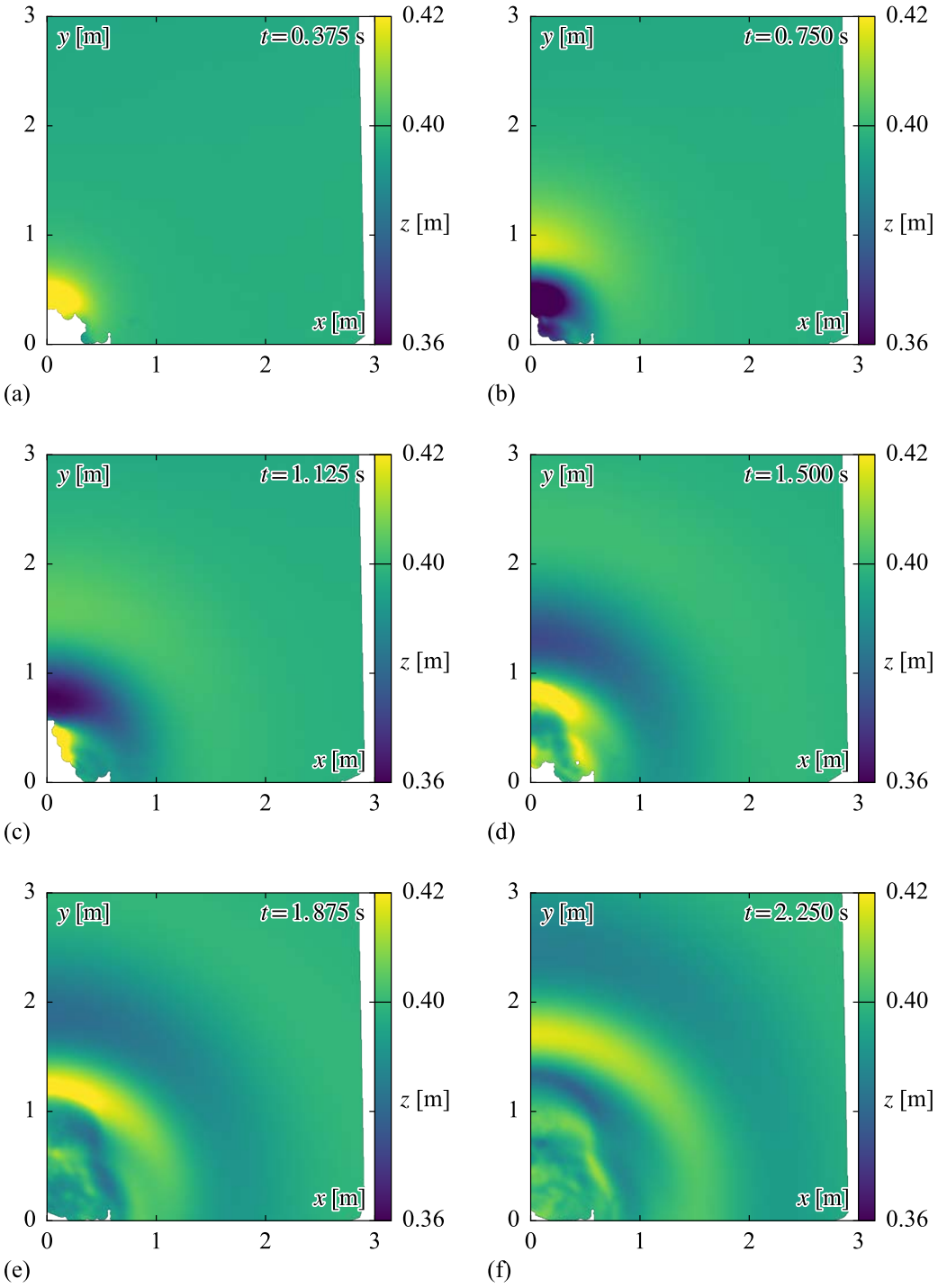

Fig. 4.6 Contour plots for test A at $h = 0.4$ m with $V_s = 1.06$ m/s, $m_s = 20$ kg, $s = 0.06$ m, $b = 0.50$ m, and $\alpha = 45°$ at different times

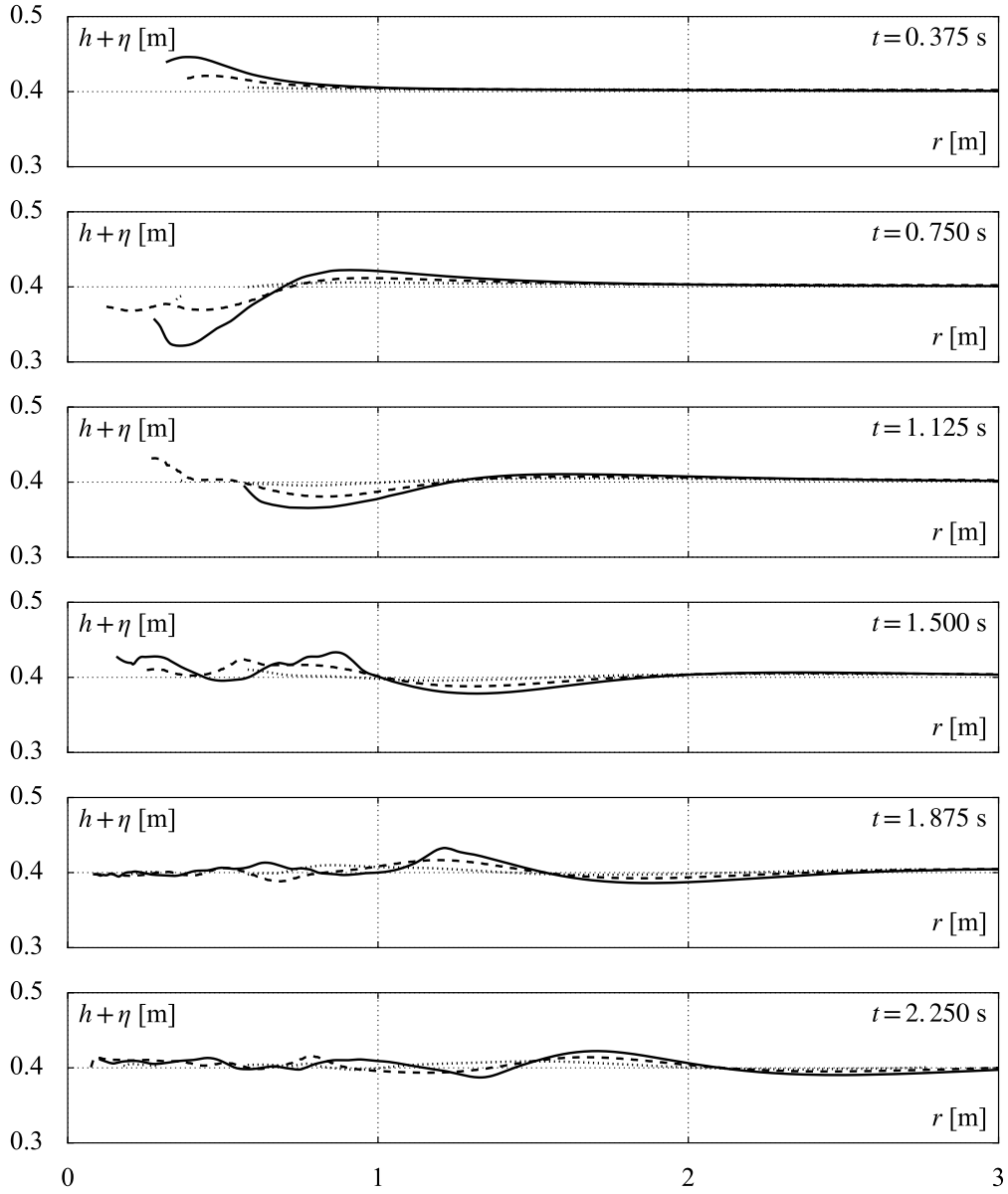

Fig. 4.7 Profile plots for test A at $h = 0.4$ m with $V_s = 1.06$ m/s, $m_s = 20$ kg, $s = 0.06$ m, $b = 0.50$ m, and $\alpha = 45°$ at $\gamma = 0°$ (—), 45° (−−), and 90° ($\cdots$) at different times

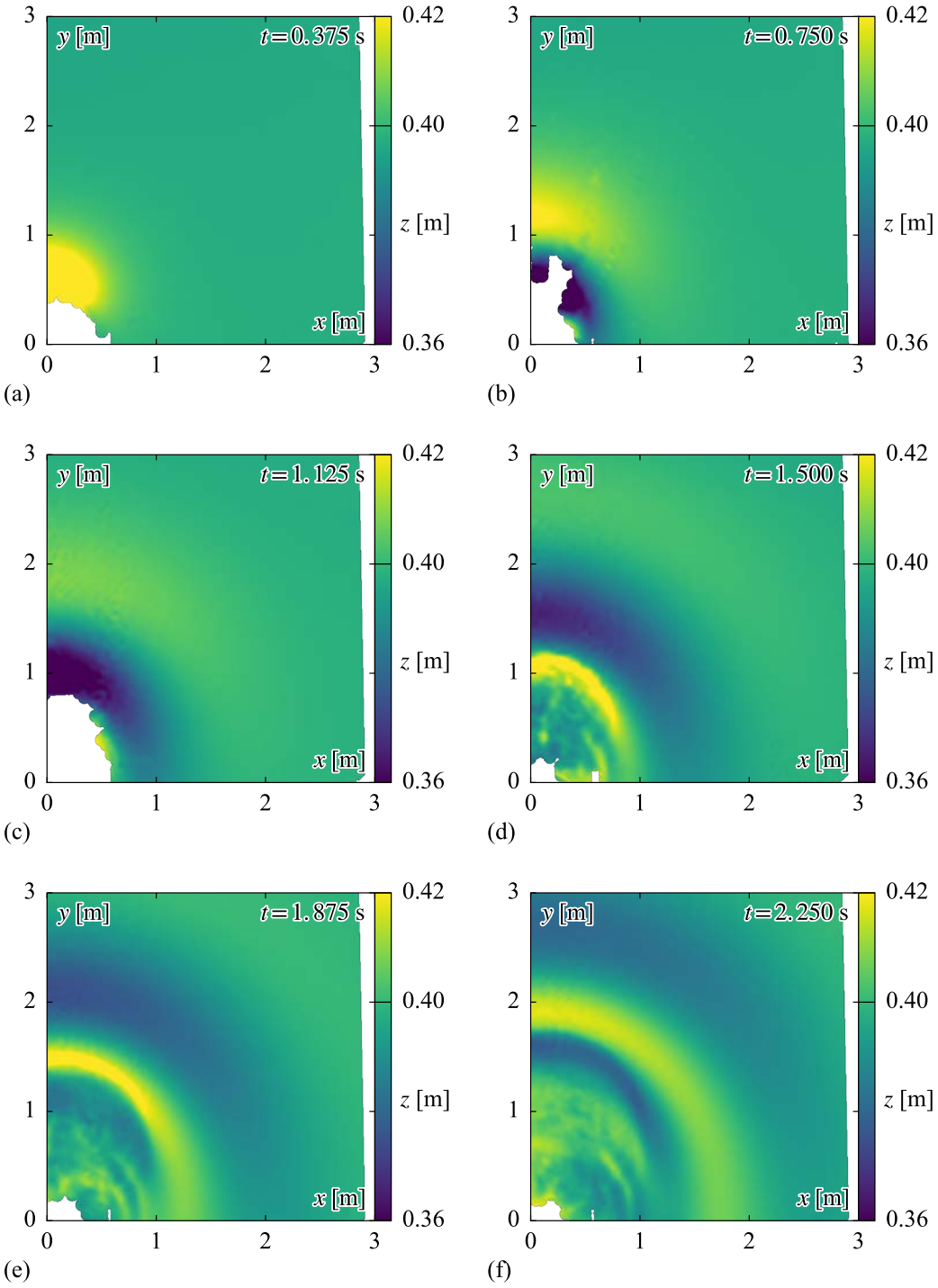

Fig. 4.8 Contour plots for test B at $h = 0.4$ m with $V_s = 2.94$ m/s, $m_s = 20$ kg, $s = 0.06$ m, $b = 0.50$ m, and $\alpha = 45°$ at different times

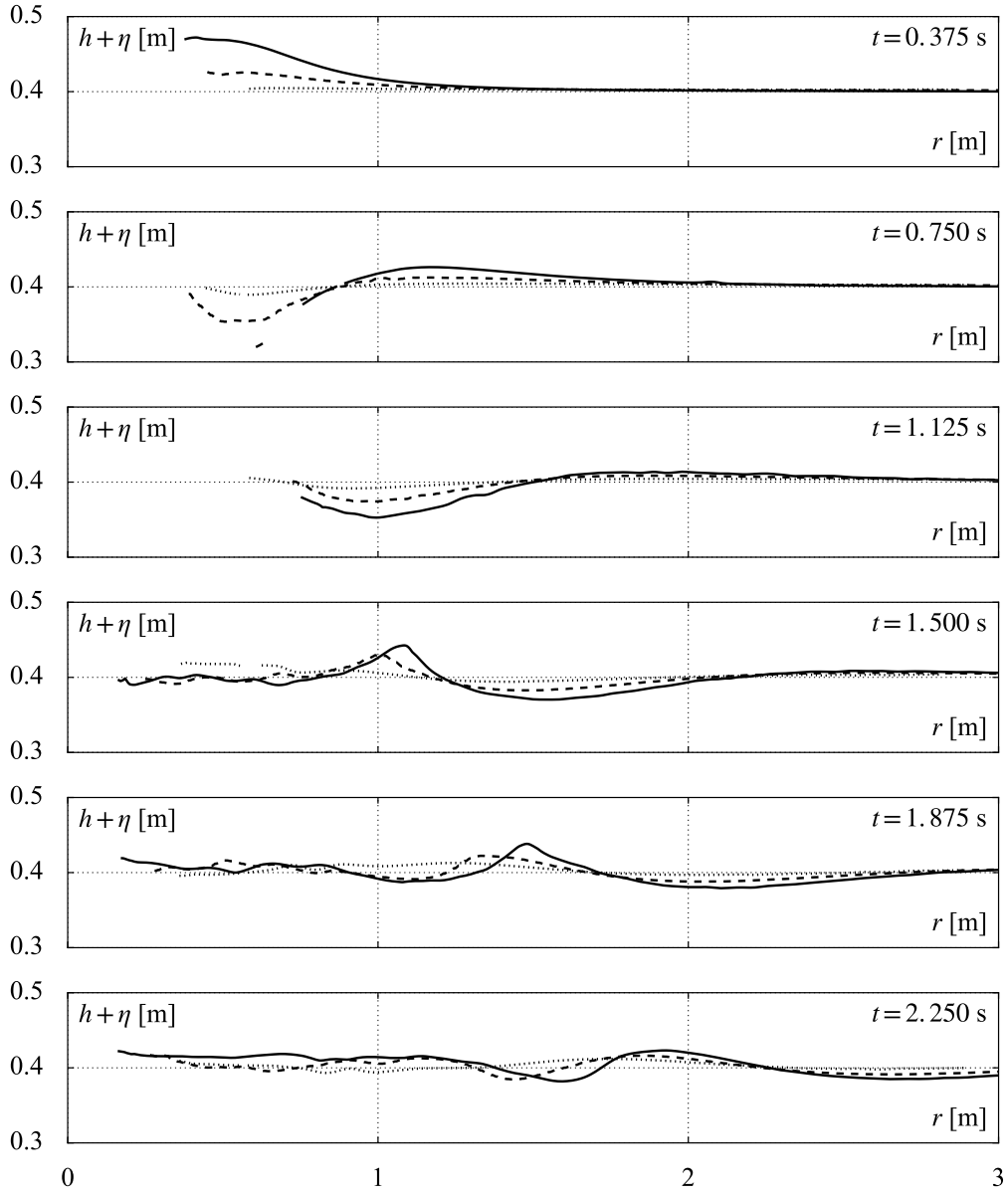

Fig. 4.9 Profile plots for test B at $h = 0.4$ m with $V_s = 2.94$ m/s, $m_s = 20$ kg, $s = 0.06$ m, $b = 0.50$ m, and $\alpha = 45°$ at $\gamma = 0°$ (—), 45° (−−), and 90° (···) at different times

Effect of slide impact angle

Figures 4.10 to 4.12 show the spatial wave generation and propagation process for Test C with a slide impact angle $\alpha = 30°$. The y- and x-axes of the contour plots in Figure 4.10 are identical to the propagation angles $\gamma = 0°$ and 90°, respectively. At $t = 0.375$ s after impact, the slide has displaced the water by pushing it upwards and a first wave crest has formed. As shown in the profile plots of Figure 4.11, this initial wave crest amplitude reaches its maximum for $\gamma = 0°$ and decreases for increasing γ. The first wave crest is propagating radially from the slide impact location (Figure 4.10) and its elevation for $\gamma = 0°$ has already decreased by 50% compared to its initial maximum (Figure 4.11) at $t = 0.750$ s. Also the first wave trough has formed at the same location, where the first wave crest had its initial maximum previously. Similar to the first wave crest, the first wave trough amplitude decreases for increasing γ. At $t = 1.125$ s, a steep second wave crest emerges, while the first wave crest and trough are subject to ongoing amplitude decay. The oblique view in Figure 4.12 at $t = 1.500$ s reveals that there are spilling features on the second wave crest for small values of γ, which are related to its steepness. The wave length, i.e. the distance between the still water level intersections in front of the wave crest and behind the corresponding wave trough, of the second wave is substantially shorter compared to the first wave of the wave train (Figure 4.11).

For Test D, presented in Figures 4.13 to 4.15, α was set to 60°. In general, the observations of the overall wave generation and radial propagation process also apply to Test D. However, even though the slide impact velocity V_s is around 30% higher compared to Test C, the initial wave crest amplitude at $t = 0.375$ s is smaller. In addition, the relative difference between the initial wave crest amplitude at $\gamma = 0°$ and 45° is less pronounced than in Test C. The slide impact angle α was further increased to 90° for Test E (Figures 4.16 to 4.18).

Although V_s of Test E is more than twice the value of Test C, the initial wave amplitude is further decreased. Note that Figure 4.17 includes $\gamma = 80°$ instead of 90°. Figures 4.12(a), 4.15(a), and 4.18(a) show the initial splash screens at their maximum extent after slide impact. The upward movement of the water surface is very distinct in Test C at $\alpha = 30°$ even for a low V_s, while it is hardly visible in Test E for $\alpha = 90°$ for a higher V_s.

The comparison between three different slide impact angles $\alpha = 30°$, 60°, and 90° shows that the momentum transfer from the slide to the water column is significantly governed by this parameter. While the slide impact velocity V_s, which has an increasing effect on the wave amplitudes, as shown for Test A and B, is doubled between Test C with $\alpha = 30°$ and Test E with $\alpha = 90°$, the observed amplitudes of the first wave decrease for $\gamma = 0°$. Moreover, α has an effect on the spatial distribution of the first wave crest: for $\alpha = 30°$, the relative difference between amplitudes at $\gamma = 0°$ and 90° is larger than for $\alpha = 90°$. While the first effect is accounted for in Eq. (2.12) by Panizzo *et al.* (2005) and Eq. (2.4) by Heller and Hager (2010), the second effect is not included in these equations.

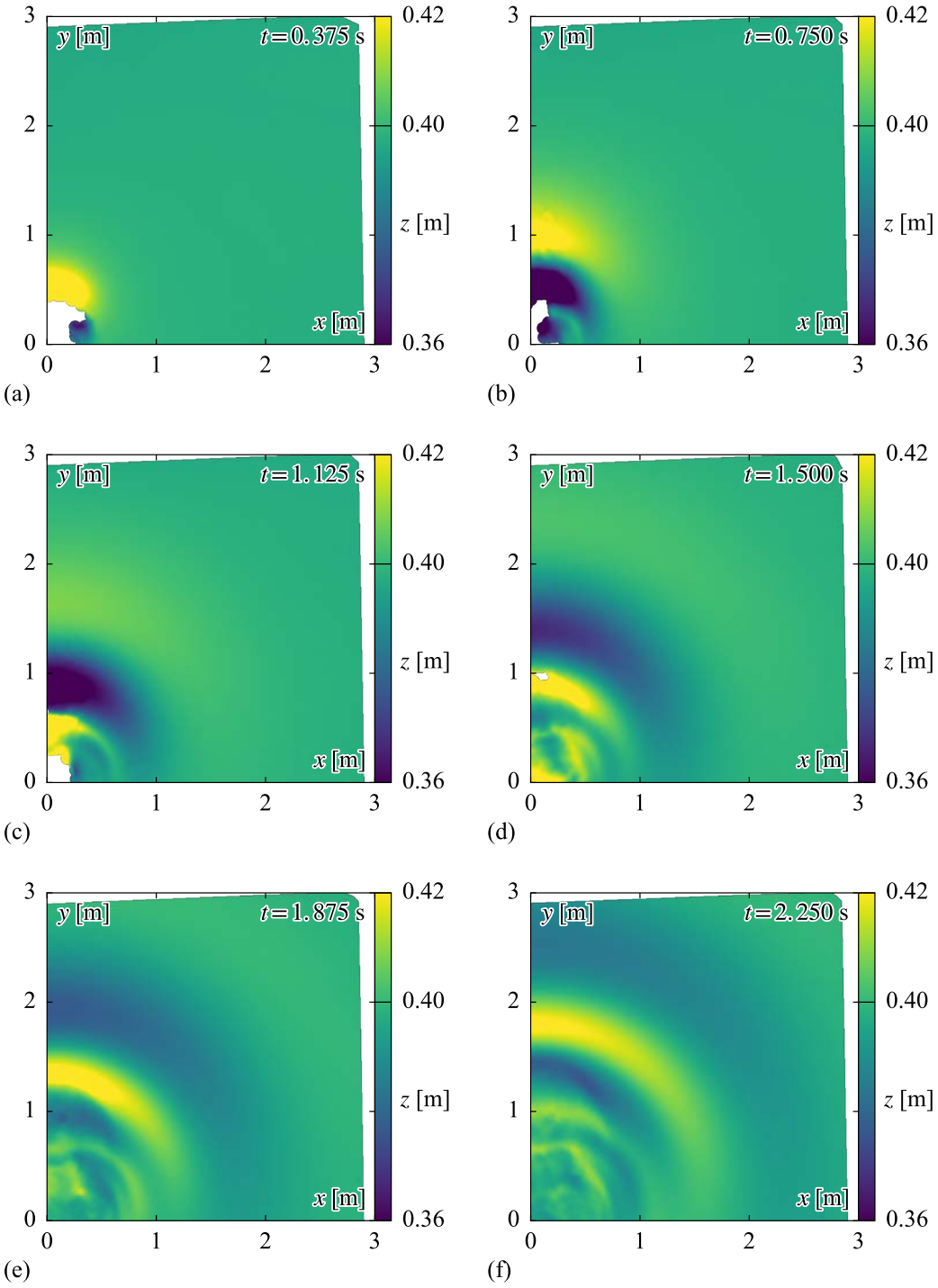

Fig. 4.10 Contour plots for test C at $h = 0.4$ m with $V_s = 1.79$ m/s, $m_s = 20$ kg, $s = 0.06$ m, $b = 0.50$ m, and $\alpha = 30°$ at different times

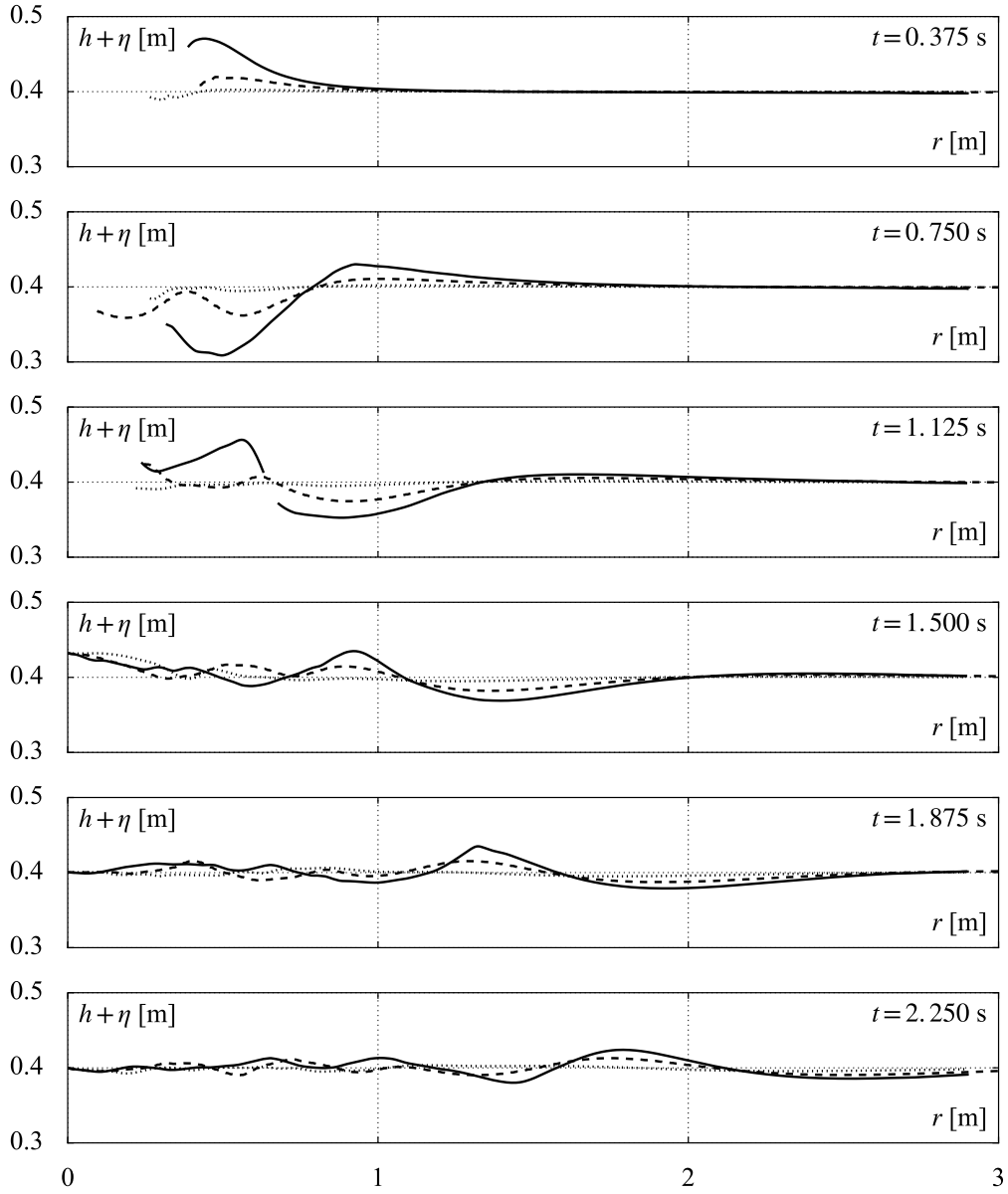

Fig. 4.11 Profile plots for test C at $h = 0.4$ m with $V_s = 1.79$ m/s, $m_s = 20$ kg, $s = 0.06$ m, $b = 0.50$ m, and $\alpha = 30°$ at $\gamma = 0°$ (—), 45° (−−), and 90° (···) at different times

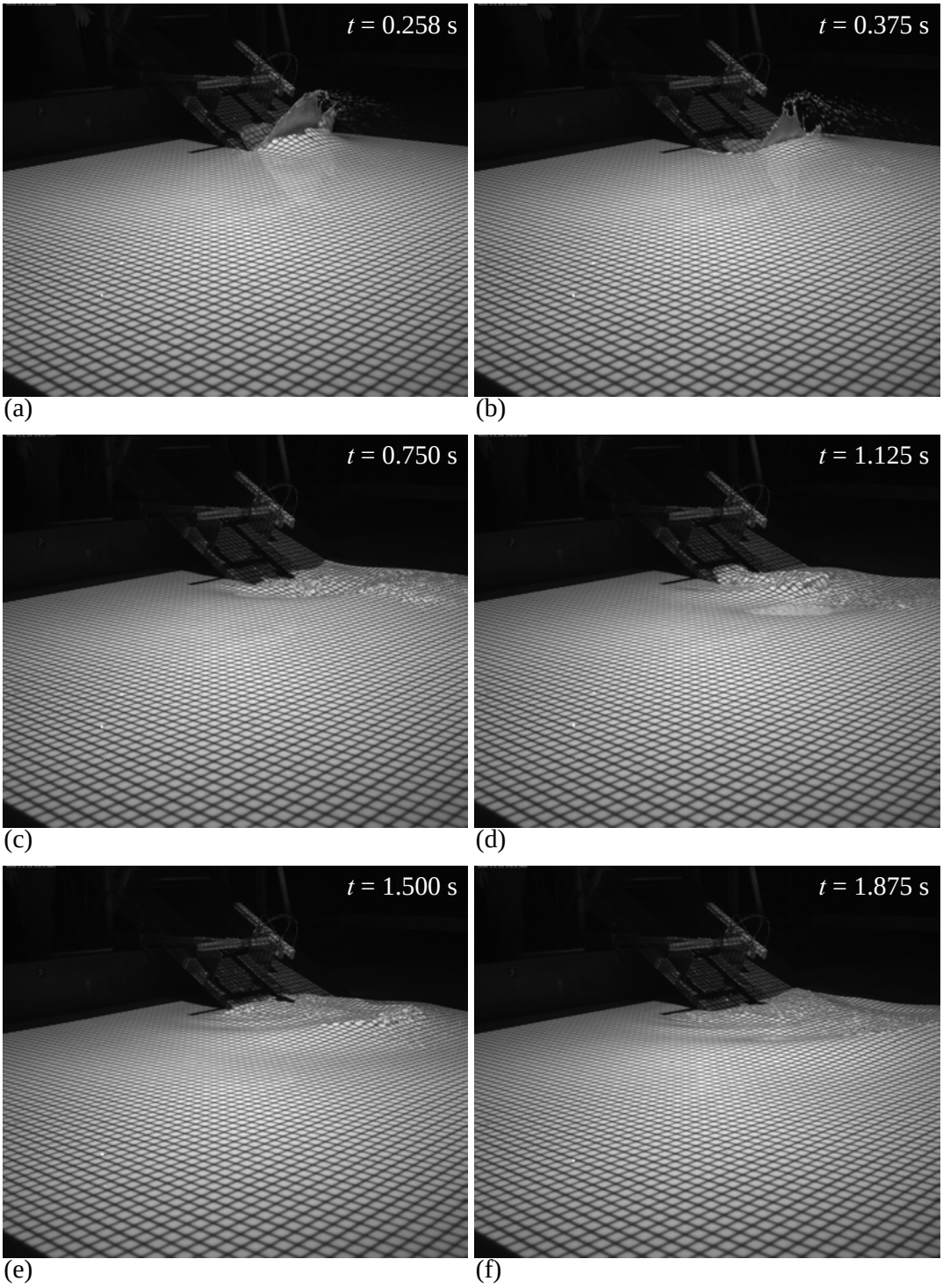

Fig. 4.12 Oblique view for test C at $h = 0.4$ m with $V_s = 1.79$ m/s, $m_s = 20$ kg, $s = 0.06$ m, $b = 0.50$ m, and $\alpha = 30°$ at different times

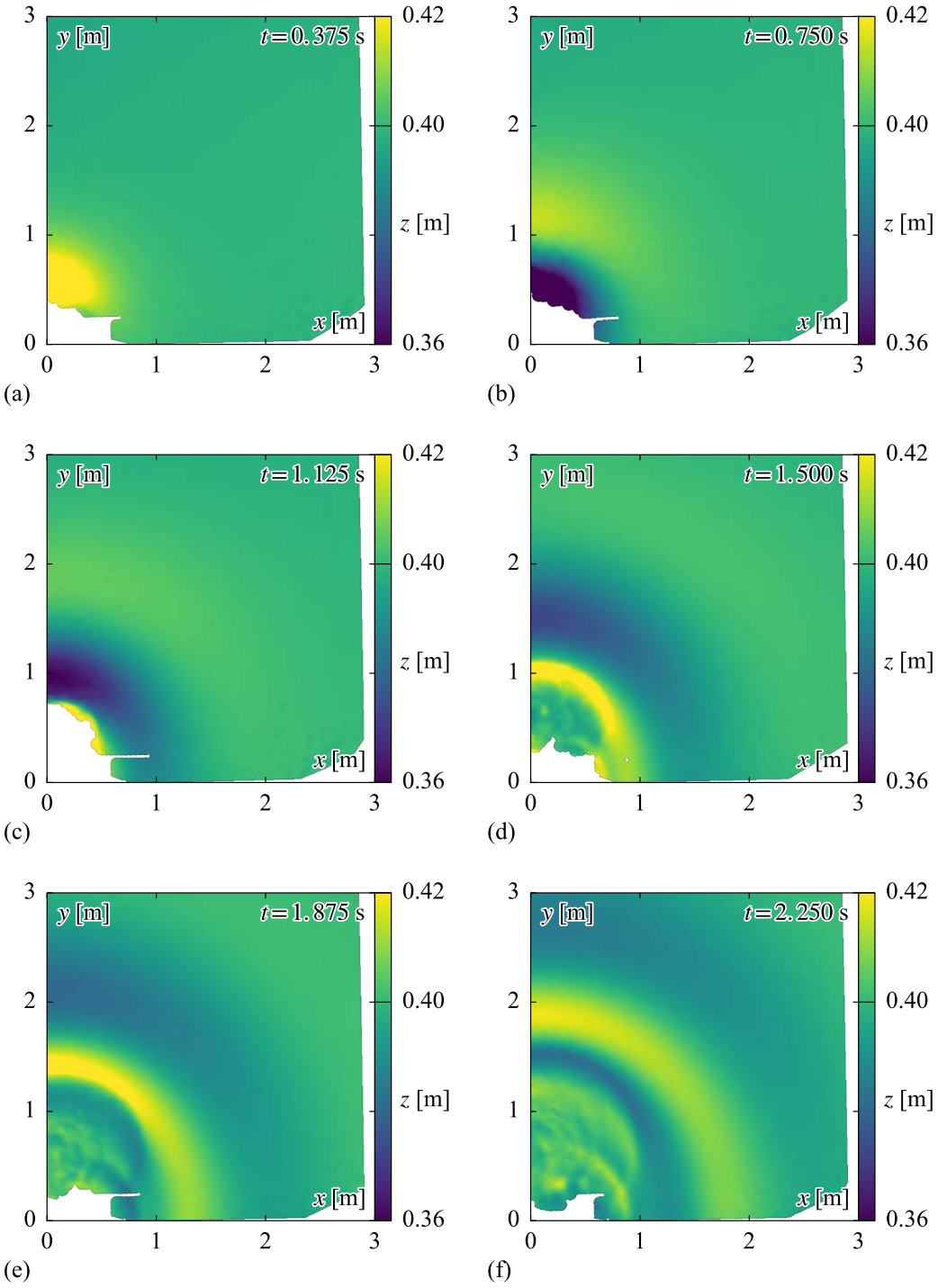

Fig. 4.13 Contour plots for test D at $h = 0.4$ m with $V_s = 2.38$ m/s, $m_s = 20$ kg, $s = 0.06$ m, $b = 0.50$ m, and $\alpha = 60°$ at different times

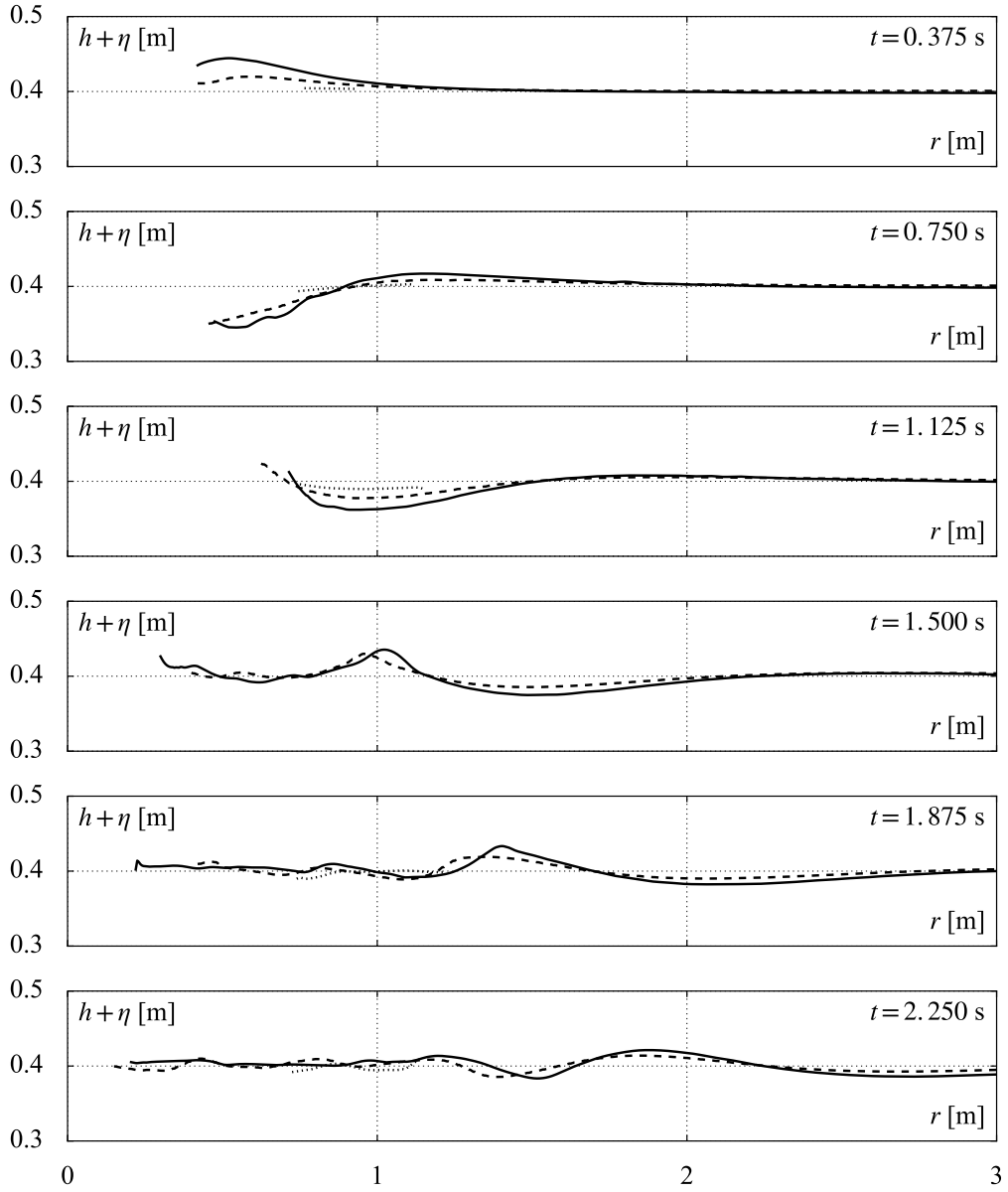

Fig. 4.14 Profile plots for test D at $h = 0.4$ m with $V_s = 2.38$ m/s, $m_s = 20$ kg, $s = 0.06$ m, $b = 0.50$ m, and $\alpha = 60°$ at $\gamma = 0°$ (—), 45° (−−), and 90° ($\cdots$) at different times

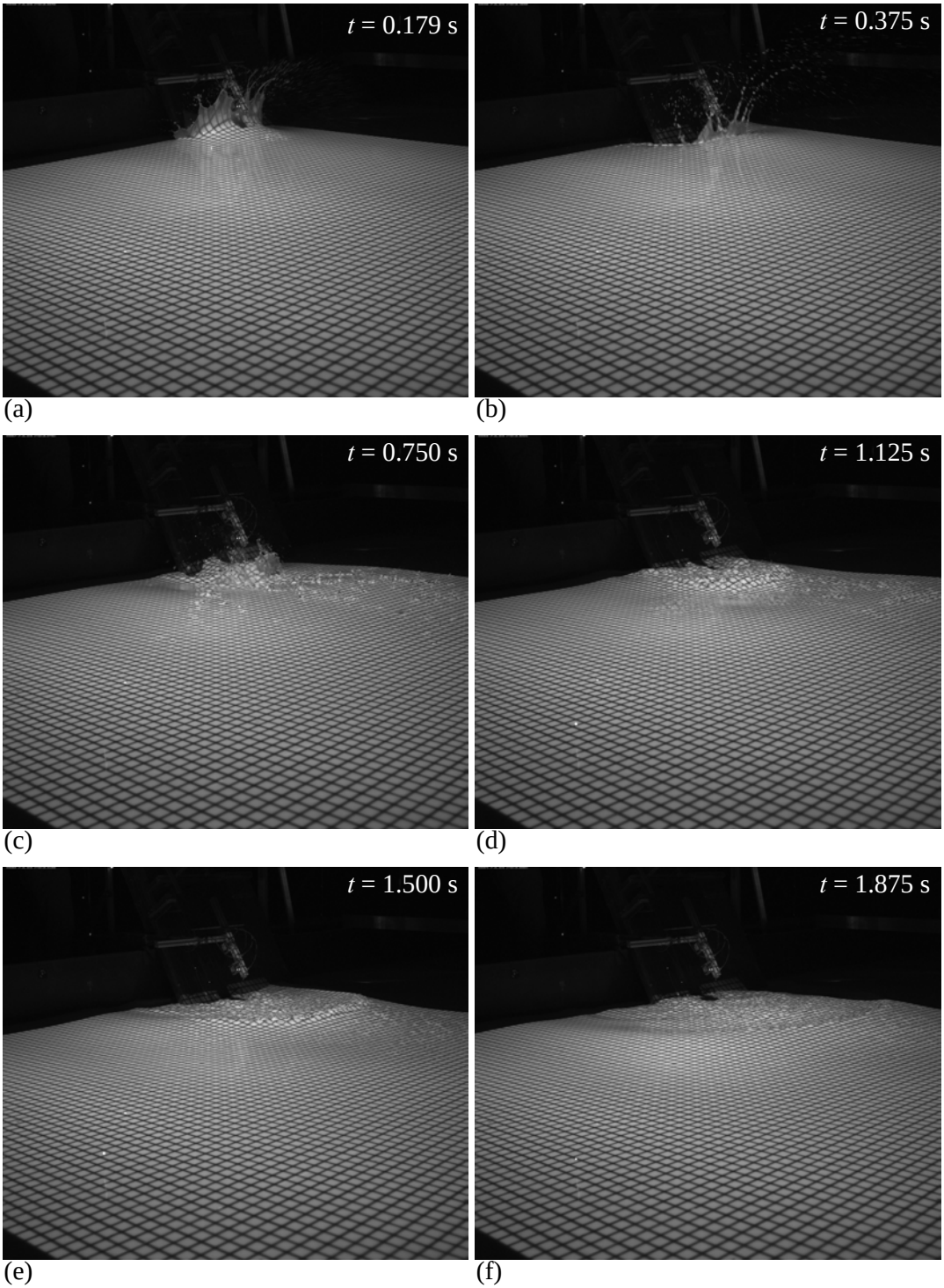

Fig. 4.15 Oblique view for test D at $h = 0.4$ m with $V_s = 2.38$ m/s, $m_s = 20$ kg, $s = 0.06$ m, $b = 0.50$ m, and $\alpha = 60°$ at different times

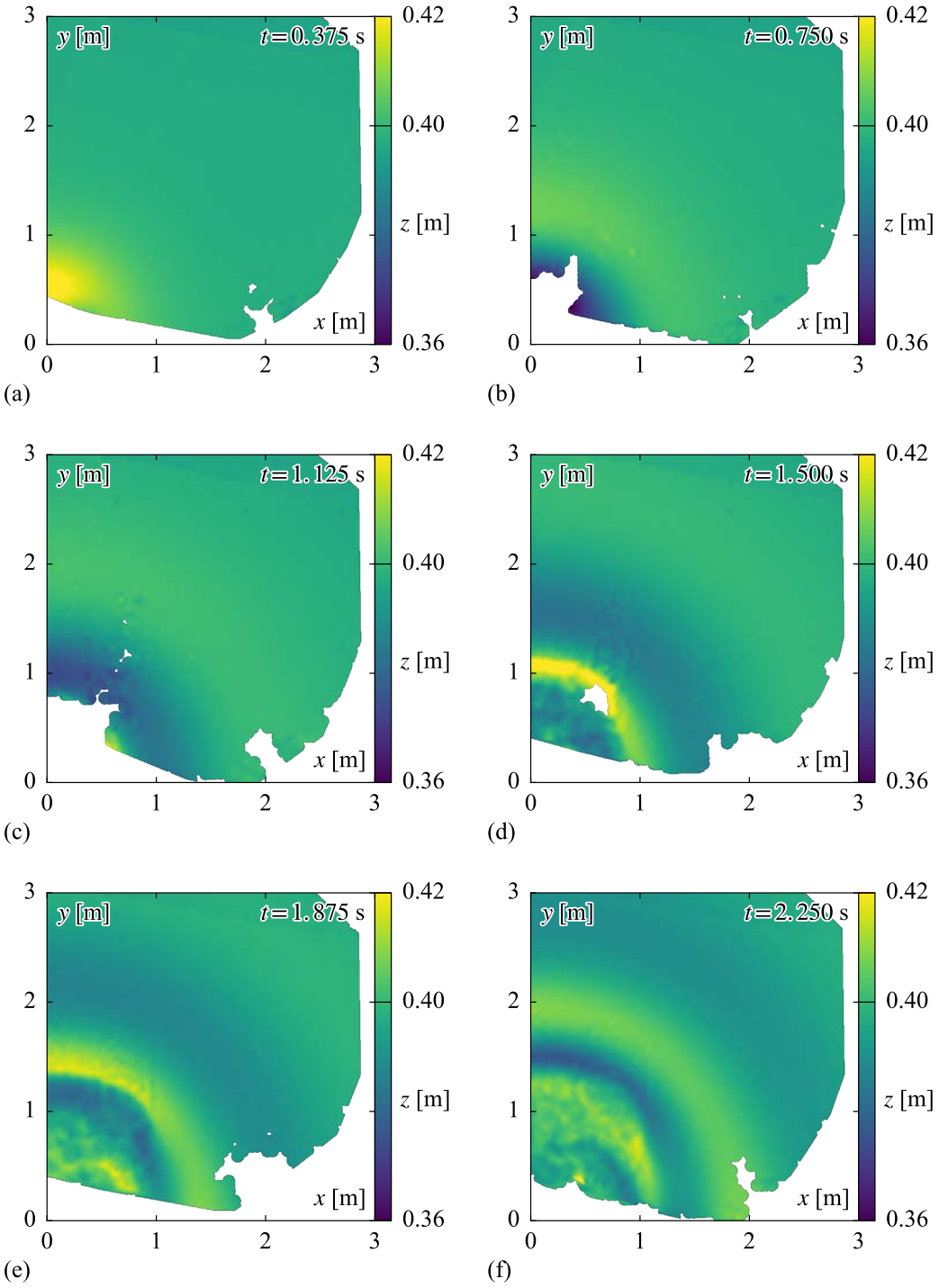

Fig. 4.16 Contour plots for test E at $h = 0.4$ m with $V_s = 3.85$ m/s, $m_s = 20$ kg, $s = 0.06$ m, $b = 0.50$ m, and $\alpha = 90°$ at different times

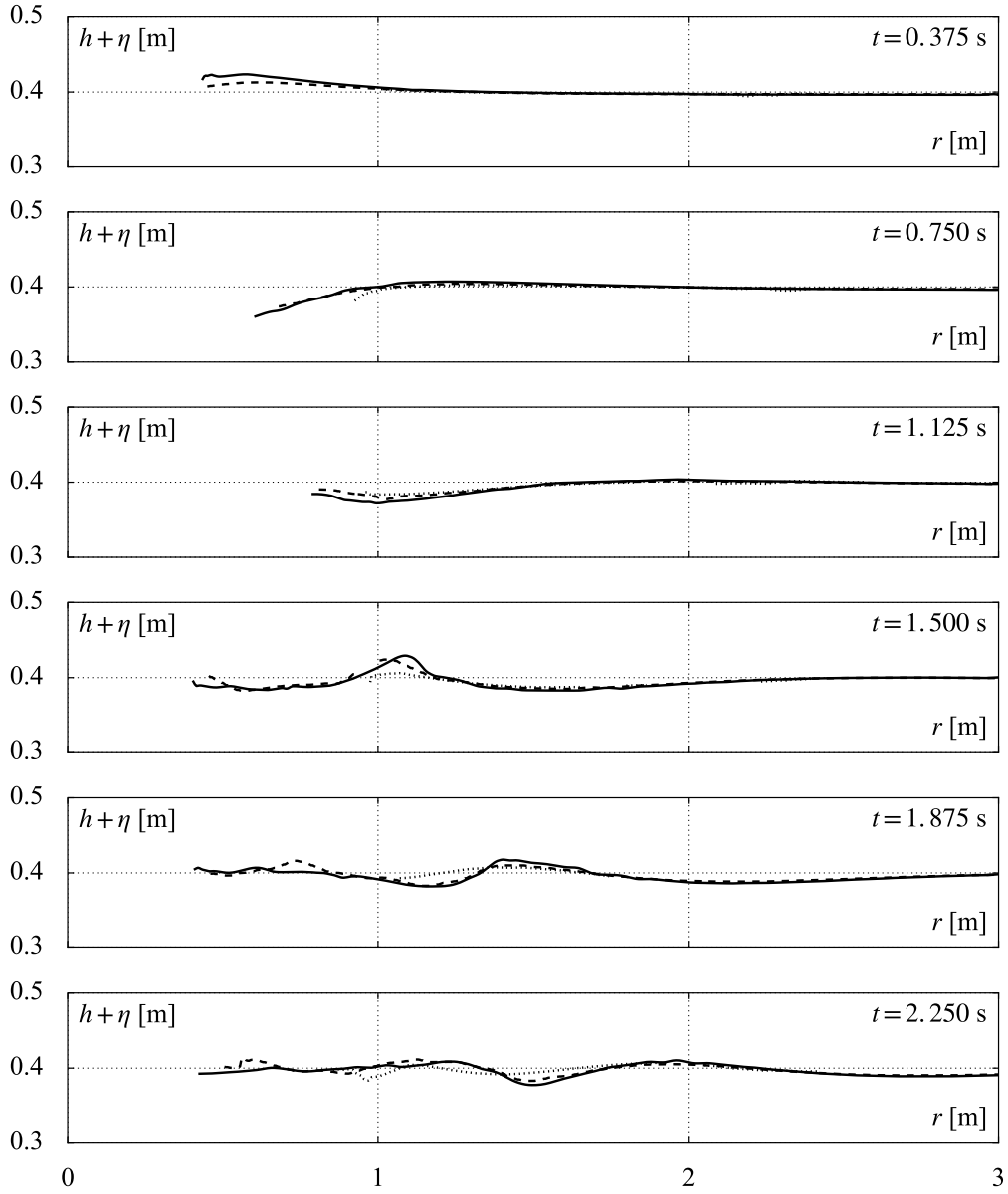

Fig. 4.17 Profile plots for test E at $h = 0.4$ m with $V_s = 3.85$ m/s, $m_s = 20$ kg, $s = 0.06$ m, $b = 0.50$ m, and $\alpha = 90°$ at $\gamma = 0°$ (—), 45° (−−), and 80° (···) at different times

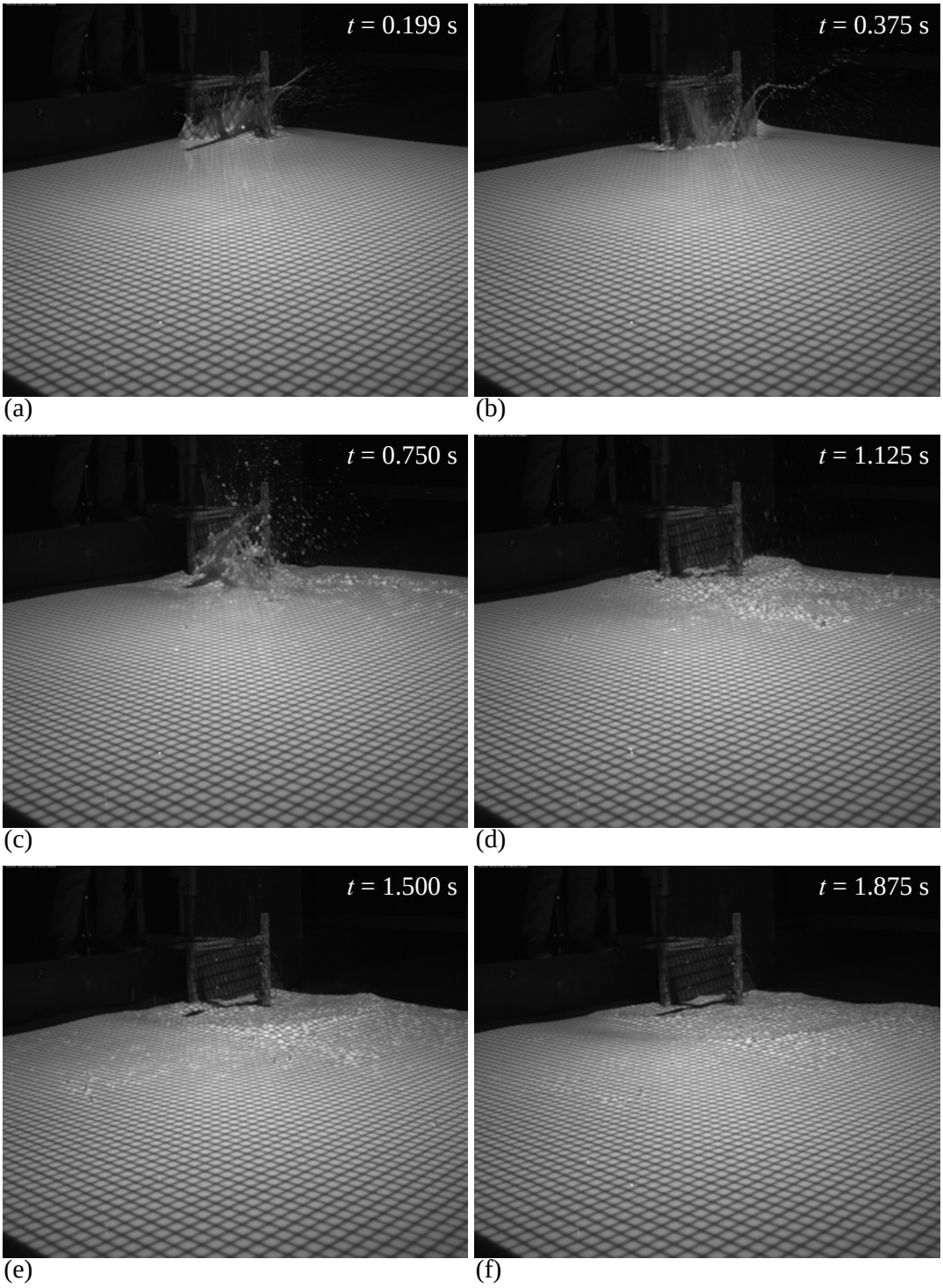

Fig. 4.18 Oblique view for test E at $h = 0.4$ m with $V_s = 3.85$ m/s, $m_s = 20$ kg, $s = 0.06$ m, $b = 0.50$ m, and $\alpha = 90°$ at different times

Effect of slide width

The effect of the slide width b is shown in Figures 4.19 to 4.24 for Test F, G, and H with $b = 0.25$ m, 0.50 m, and 1.00 m, respectively. The other geometric parameters, i.e. slide thickness $s = 0.06$ m, slide impact angle $\alpha = 60°$, and still water depth $h = 0.2$ m, remained constant for all three tests. The variation of b led to bulk slide masses $m_s = 10$ kg, 20 kg, and 40 kg, respectively. Since the slide impact velocities V_s were close to each other in the range of 2.70 m/s to 3.03 m/s and the relative bulk slide mass M is defined as the ratio of m_s to a water mass $\rho_w bh^2$ including b, all tests feature a similar impulse product parameter P (Eq. 2.4). Therefore, in a 2D wave channel with a width equal to b, all experiments would also yield similar wave characteristics. However, there are significant differences observable for spatial wave propagation in a 3D wave basin. The initial wave crest amplitude at $t = 0.375$ s increases with increasing b, which is evident in the contour as well as in the profile plots. In addition, the location where the initial amplitude has formed is also increasingly further off from the slide impact location. While in Test F the initial amplitude has formed approximately at $r = 0.5$ m (Figure 4.20), the location is at $r = 0.6$ m for Test G (Figure 4.22), and the initial amplitude has not yet formed at this location in Test H (Figure 4.24). Moreover, the propagation pattern of the initial wave crest of Test H is elliptic and not nearly circular as in Test F and G. All subsequent wave amplitudes are larger for increasing b. At $t = 2.250$ s, the second wave crest of Test H is still steep and not flattened as in Test F and G.

The wave amplitudes as well as their initial spatial outline are strongly affected by the slide width b. The prediction equations presented in Section 2.3.3 include this effect only in a subordinate way.

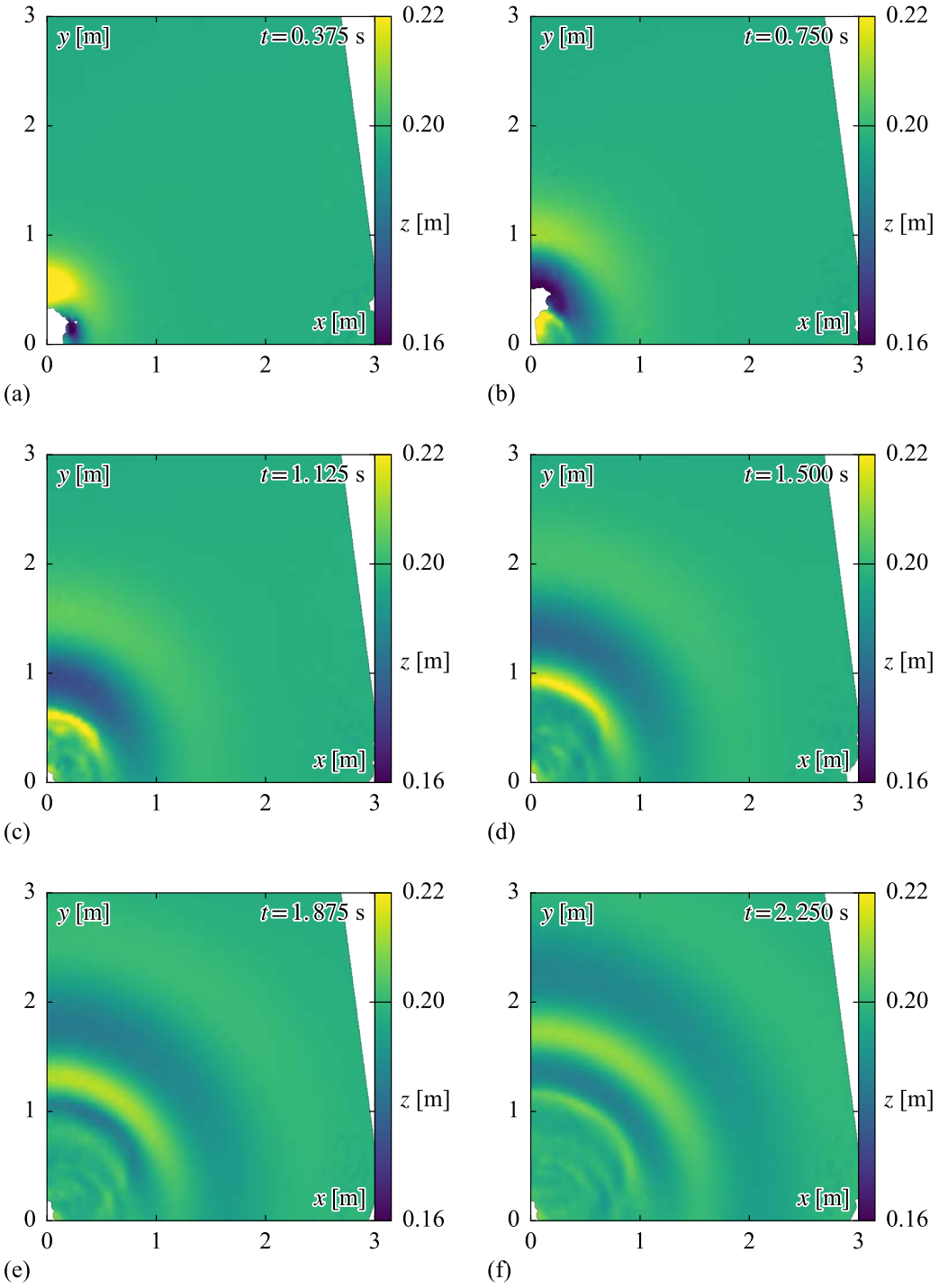

Fig. 4.19 Contour plots for test F at $h = 0.2$ m with $V_s = 3.03$ m/s, $m_s = 10$ kg, $s = 0.06$ m, $b = 0.25$ m, and $\alpha = 60°$ at different times

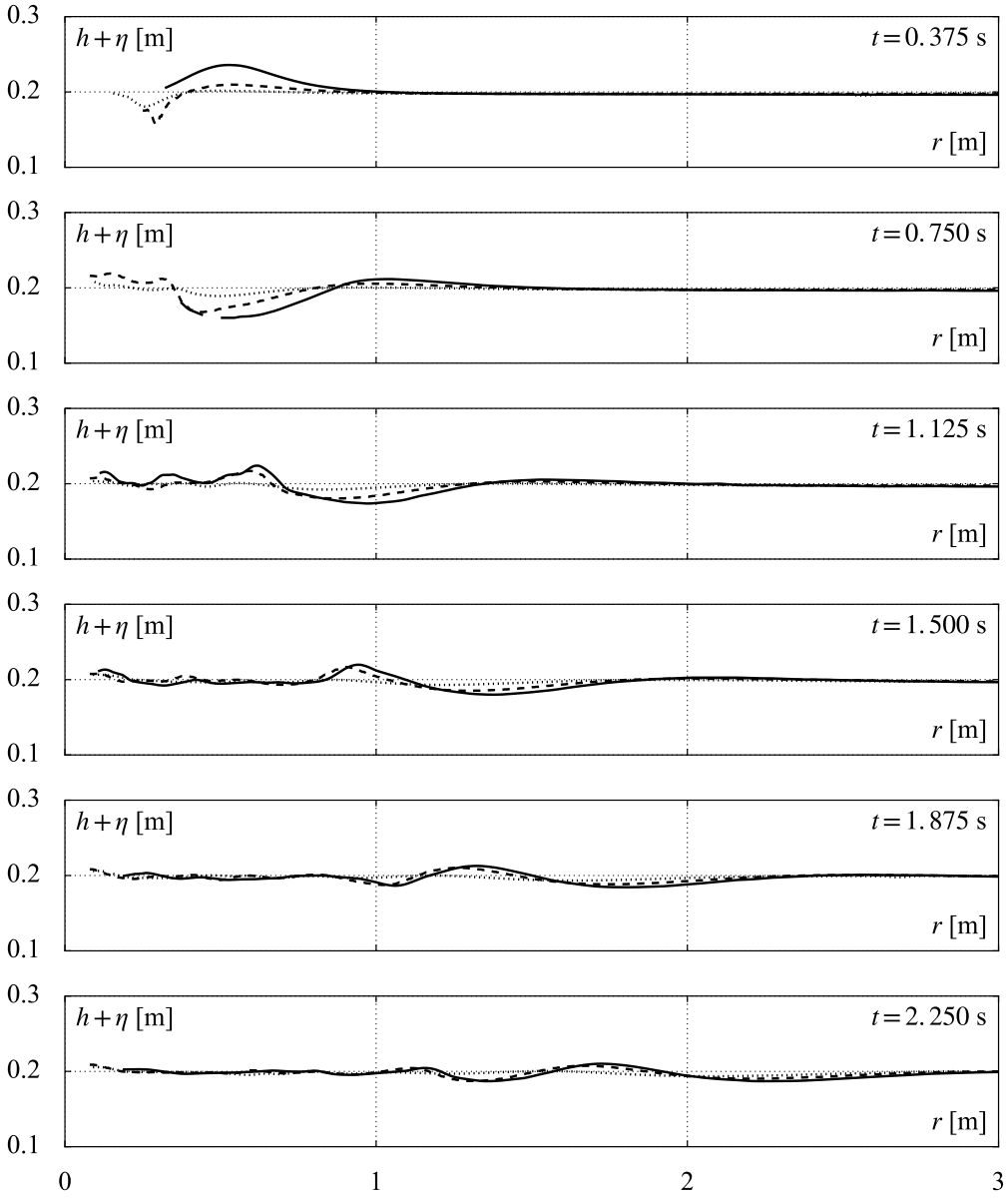

Fig. 4.20 Profile plots for test F at $h = 0.2$ m with $V_s = 3.03$ m/s, $m_s = 10$ kg, $s = 0.06$ m, $b = 0.25$ m, and $\alpha = 60°$ at $\gamma = 0°$ (—), 45° (−−), and 90° ($\cdots$) at different times

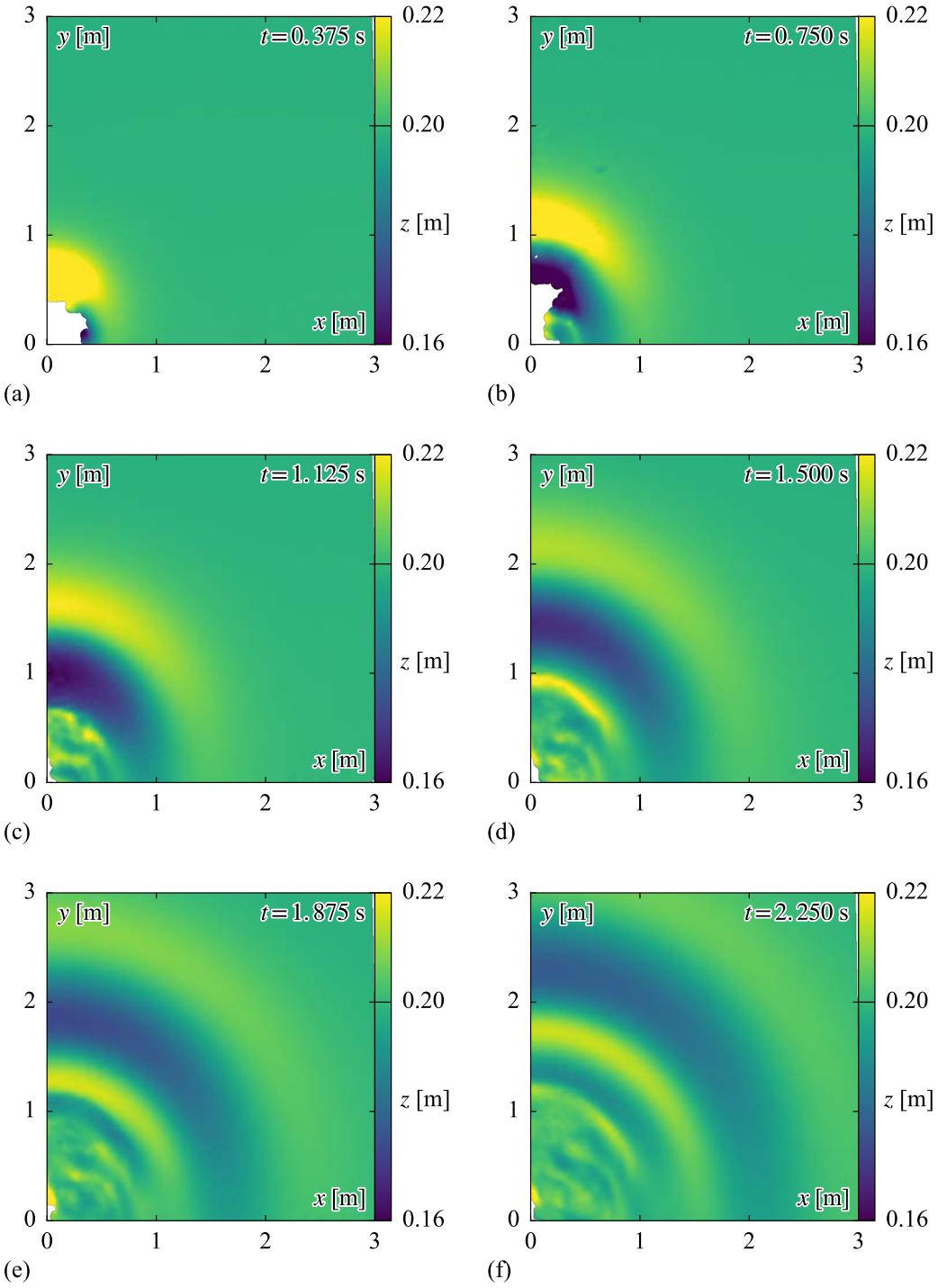

Fig. 4.21 Contour plots for test G at $h = 0.2$ m with $V_s = 2.70$ m/s, $m_s = 20$ kg, $s = 0.06$ m, $b = 0.50$ m, and $\alpha = 60°$ at different times

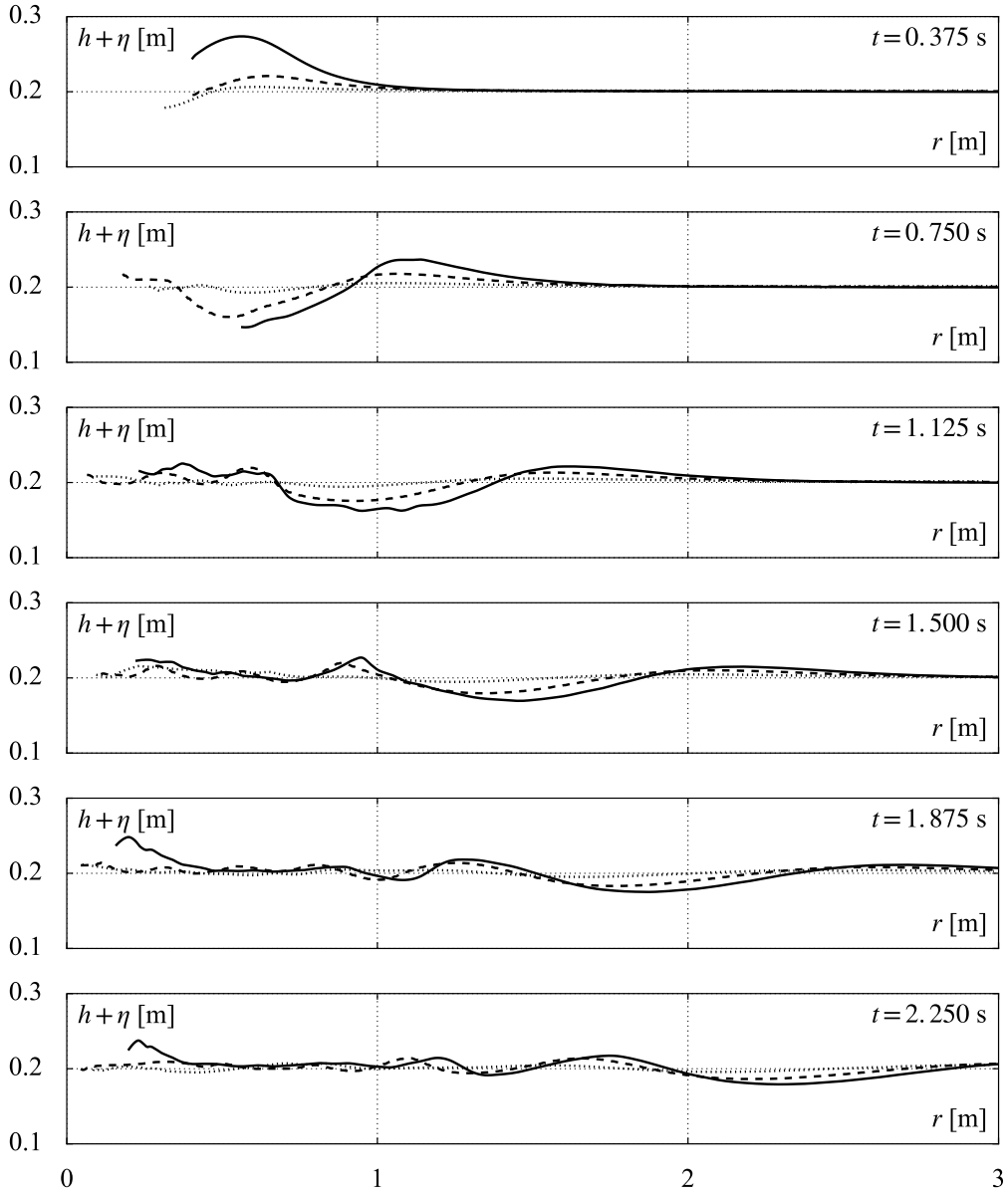

Fig. 4.22 Profile plots for test G at $h = 0.2$ m with $V_s = 2.70$ m/s, $m_s = 20$ kg, $s = 0.06$ m, $b = 0.50$ m, and $\alpha = 60°$ at $\gamma = 0°$ (—), 45° (−−), and 90° (···) at different times

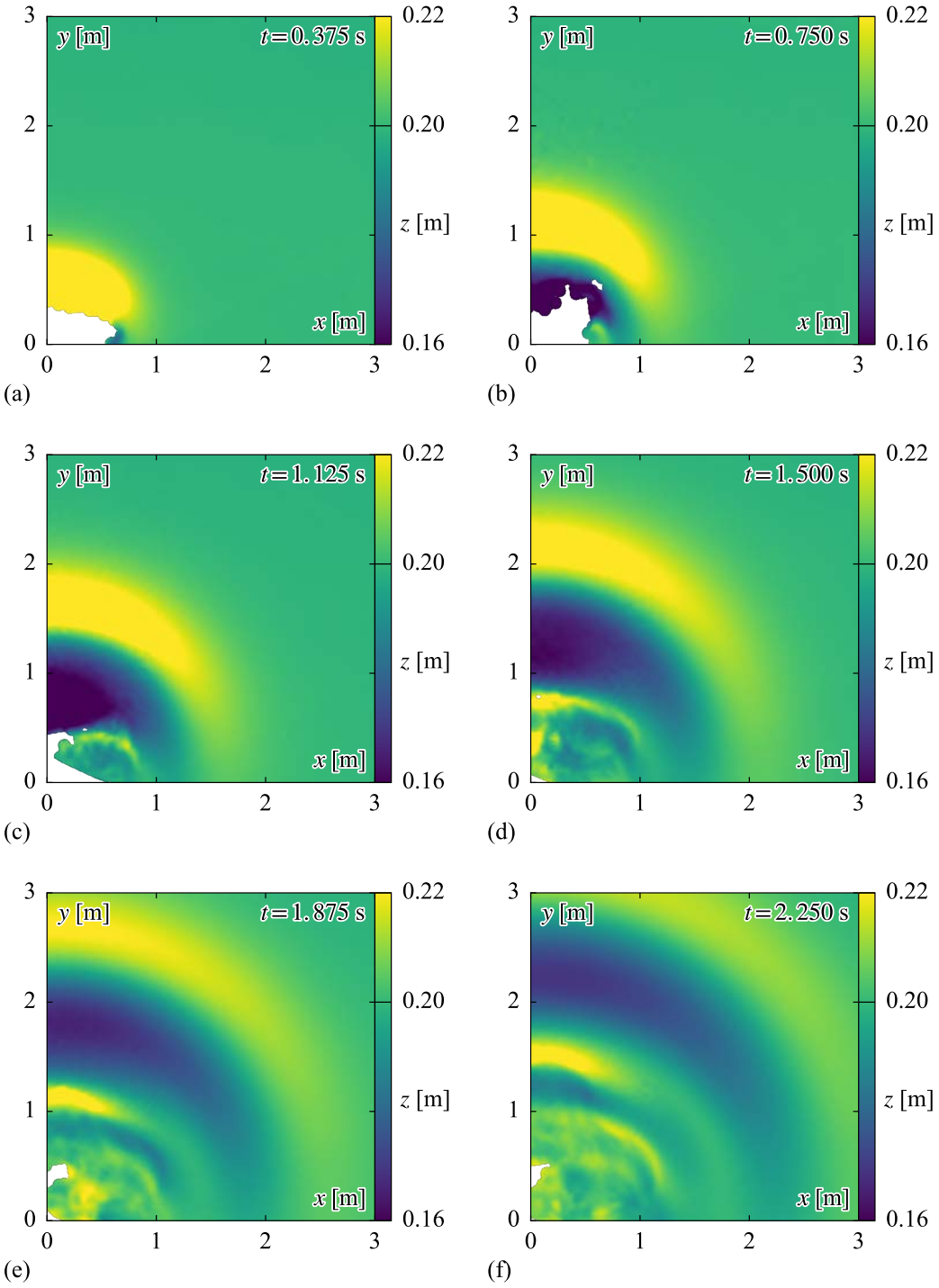

Fig. 4.23 Contour plots for test H at $h = 0.2$ m with $V_s = 2.78$ m/s, $m_s = 40$ kg, $s = 0.06$ m, $b = 1.00$ m, and $\alpha = 60°$ at different times

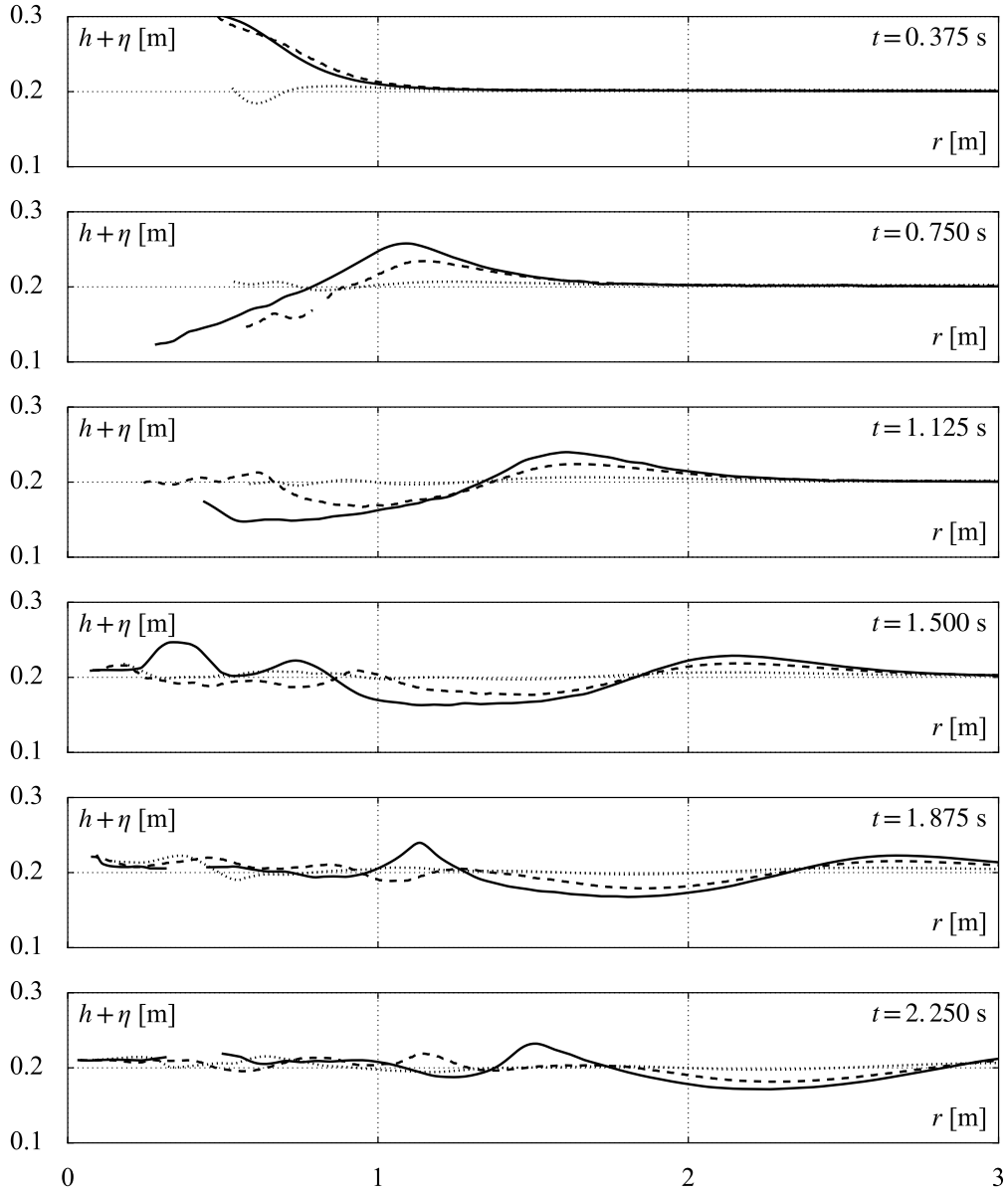

Fig. 4.24 Profile plots for test H at $h = 0.2$ m with $V_s = 2.78$ m/s, $m_s = 40$ kg, $s = 0.06$ m, $b = 1.00$ m, and $\alpha = 60°$ at $\gamma = 0°$ (—), 45° (−−), and 90° ($\cdots$) at different times

Wave crest evolution

In Figure 4.25(a), the the first wave crest amplitude a_{c1} is plotted versus the wave propagation angle γ for different time steps t between 0.38 s and 2.17 s. For all γ, a_{c1} is decreasing over time during propagation. However, the relative decay rate is higher for $\gamma = 0°$ than for 90°. This observation is confirmed by Figure 4.25(b). While a_{c1} at $\gamma = 90°$ accounts for 8% of a_{c1} at $\gamma = 0°$ at $t = 0.38$ s, this ratio increases to 43% at $t = 2.17$ s. These findings indicate a lateral spreading effect on the wave crest normal to the propagation direction. Except for Eq. (2.25) by Heller and Spinneken (2015), all other approaches discussed in Section 2.3.3 feature a constant ratio between $\gamma = 0°$ and 90°.

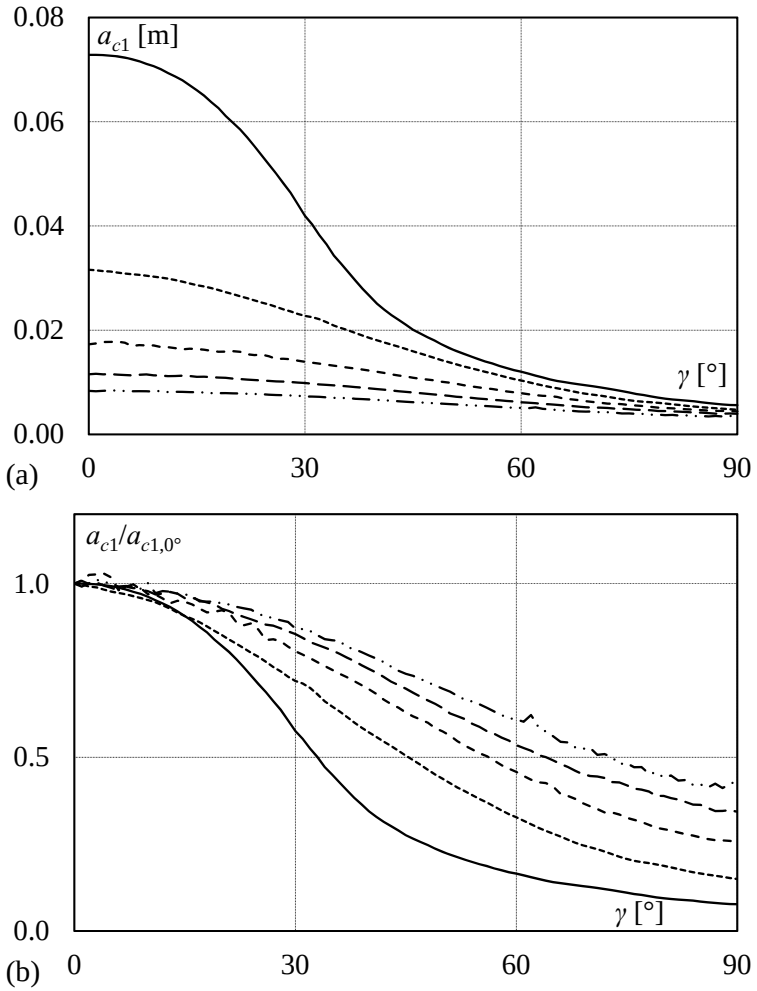

Fig. 4.25 First wave crest elevation profile plots for test G at $h = 0.2$ m with $V_s = 2.70$ m/s, $m_s = 20$ kg, $s = 0.06$ m, $b = 0.50$ m, and $\alpha = 60°$ at $t = 0.38$ s (—), 0.83 s, 1,29 s, 1,75 s, and 2.17 s (—··—) for (a) a_{c1} and (b) $a_{c1}/a_{c1,0°}$ versus γ

4.3.3 Comparative study

The applicability of existing equations for the prediction of spatial impulse wave propagation (Section 2.3.3) is evaluated for the experiments in Table 4.4. In Figure 4.26, the predicted first wave heights $Y_{1,\text{pred}}$ are compared to the measured values $Y_{1,\text{meas}}$. Nine point measurement locations were extracted from the measured water surface contours at radial wave propagation distances $r = 1.0$ m, 1.8 m, and 2.6 m for wave propagation angles $\gamma = 0°$, 30°, and 60° in each case. The prediction equations are intentionally applied outside their apparent ranges of applicability, with the aim to assess their behaviour on an extended parameter range and to obtain a starting point for the development of a novel approach.

Table 4.4 Overview of governing parameters for selected experimental runs (Evers and Hager 2016b)

Test	Symbol	F [-]	M [-]	S [-]	B [-]	l_s/h [-]	α [°]	P [-]
I	△	3.11	1	0.3	2.5	2.49	60	1.34
II	▲	2.16	1	0.6	2.5	1.25	60	1.32
III	◊	2.46	1	0.3	2.5	2.49	45	1.19
IV	♦	1.78	1	0.6	2.5	1.25	45	1.22
V	○	1.37	1	0.3	2.5	2.49	30	0.71
VI	•	1.09	1	0.6	2.5	1.25	30	0.80

The measured wave heights $Y_{1,\text{meas}}$ exceed the wave heights $Y_{1,\text{pred}}$ predicted with the method by Panizzo *et al.* (2005) considerably (Figure 4.26a). For slides with $S = 0.3$, the actual wave heights are two to four times larger. The method by Heller *et al.* (2009) generally overestimates $Y_{1,\text{meas}}$, which are up to 50% smaller (Figure 4.26b). No distinct dependencies on the slide thickness s and the slide impact angle α are observed. Mohammed and Fritz (2012) conducted their experiments at a fixed slide impact angle $\alpha = 27.1°$. Hence, a dependency on this slide parameter is evident in Figure 4.26(c). Contrary to apparent expectations, the prediction is best for $\alpha = 60°$ and increasingly underestimates the actual wave heights for 45° and 30°. However, as Eqs. (2.17) and (2.18) are based on the slide front Froude number F_f, the predicted wave heights for granular slides would be higher (see Section 2.3.3). The equations by Heller and Spinneken (2015) both over- and underestimate the actual wave heights in a scatter range of approximately $\pm 50\%$. While $Y_{1,\text{meas}}$ is overestimated for thicker slides with $S = 0.6$, thinner slides with $S = 0.3$ are underestimated. Furthermore, Figure 4.26 allows for the assessment of the wave height decay rate. While the method by Heller *et al.* (2009) reproduces the initial wave heights close to the impact location well, it tends to underestimate the decay process, i.e. overestimation of the wave height increases with increasing radial wave propagation distance r. The method by Mohammed and Fritz (2012) features a contrary characteristic. As shown in Figure 4.26(d), the decay rate of the wave heights predicted with Heller and Spinneken (2015) appears to be aligned best. Note, that their approach is the only one taking into account a wave crest spreading normal to the propagation direction (Eq. 2.25),

which is also observed in Figure 4.25(b). A more detailed discussion of the comparative study is provided by Evers and Hager (2016b).

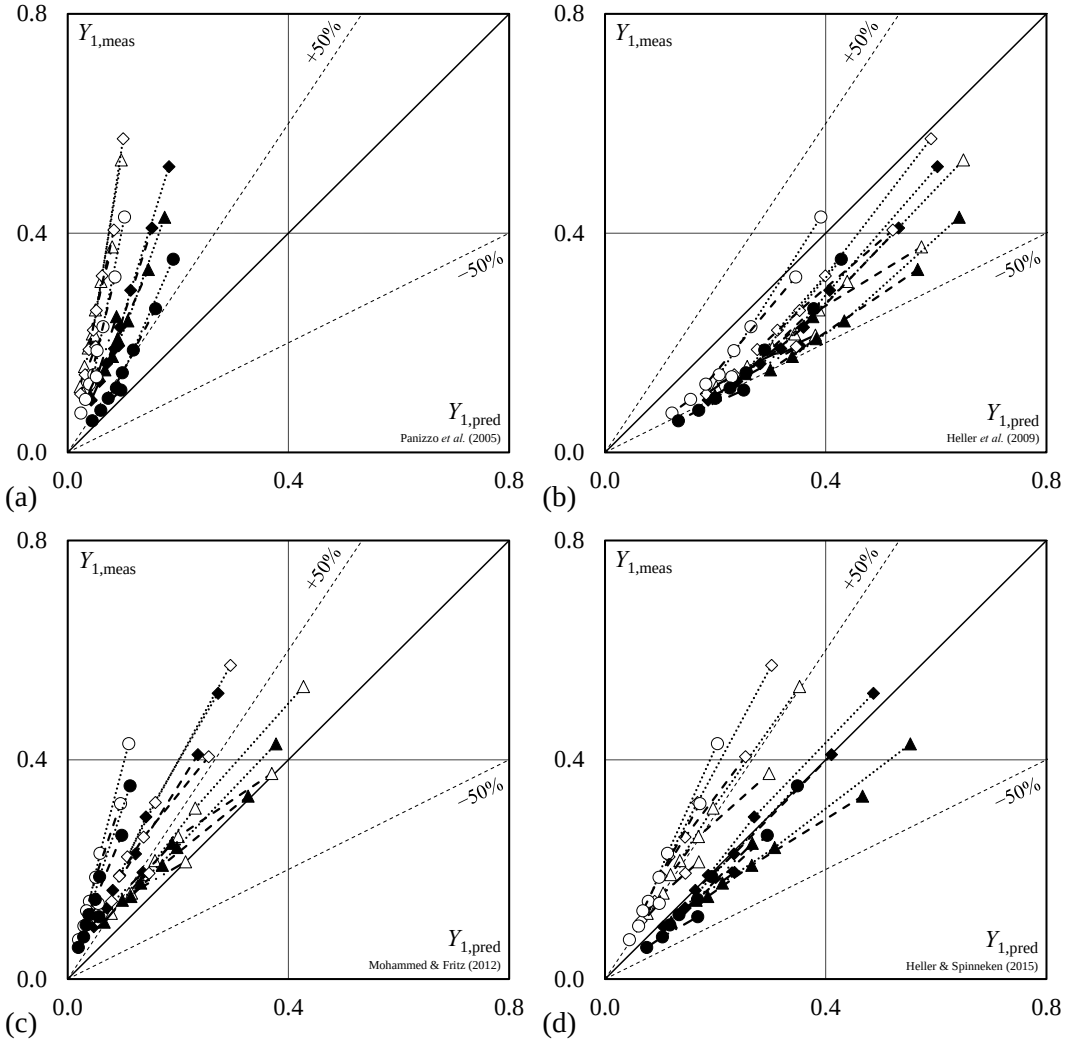

Fig. 4.26 Measured relative wave heights $Y_{1,meas}$ versus predicted $Y_{1,pred}$ with (a) Eq. (2.12), (b) Eq. (2.13), (c) Eq. (2.23), and (d) Eq. (2.24) for slide impact angles $\alpha = 30°$ (●, ○), 45° (♦, ◇), and 60° (▲, △) and relative slide thicknesses $S = 0.6$ (●, ♦, ▲) and 0.3 (○, ◇, △) for wave propagation angles $\gamma = 0°$ (···), 30° (−−), and 60° (−···−)

4.3.4 Slide impact zone

4.3.4.1 Impact radius

Profiles of the water surface during the wave generation process are shown in Figure 4.27. At $t = 0.000$ s the water surface is undisturbed at $h = 0.3$ m. After 0.292 s, the water surface is displaced by the slide impact, which creates an impact crater. The crater starts to collapse at $t = 0.417$ s and the first wave crest forms. At $t = 0.500$ s the crest is fully developed at wave propagation distance defined as the impact radius r_0. The water surface

profiles at $t = 1.000$ s and 1.292 s show that also the initial first wave trough and the second wave crest amplitudes are forming at r_0. Compared to experimental setups with fixed point measurements, the videometric measurement system allows for adaptively tracking of the initial wave features at variable locations.

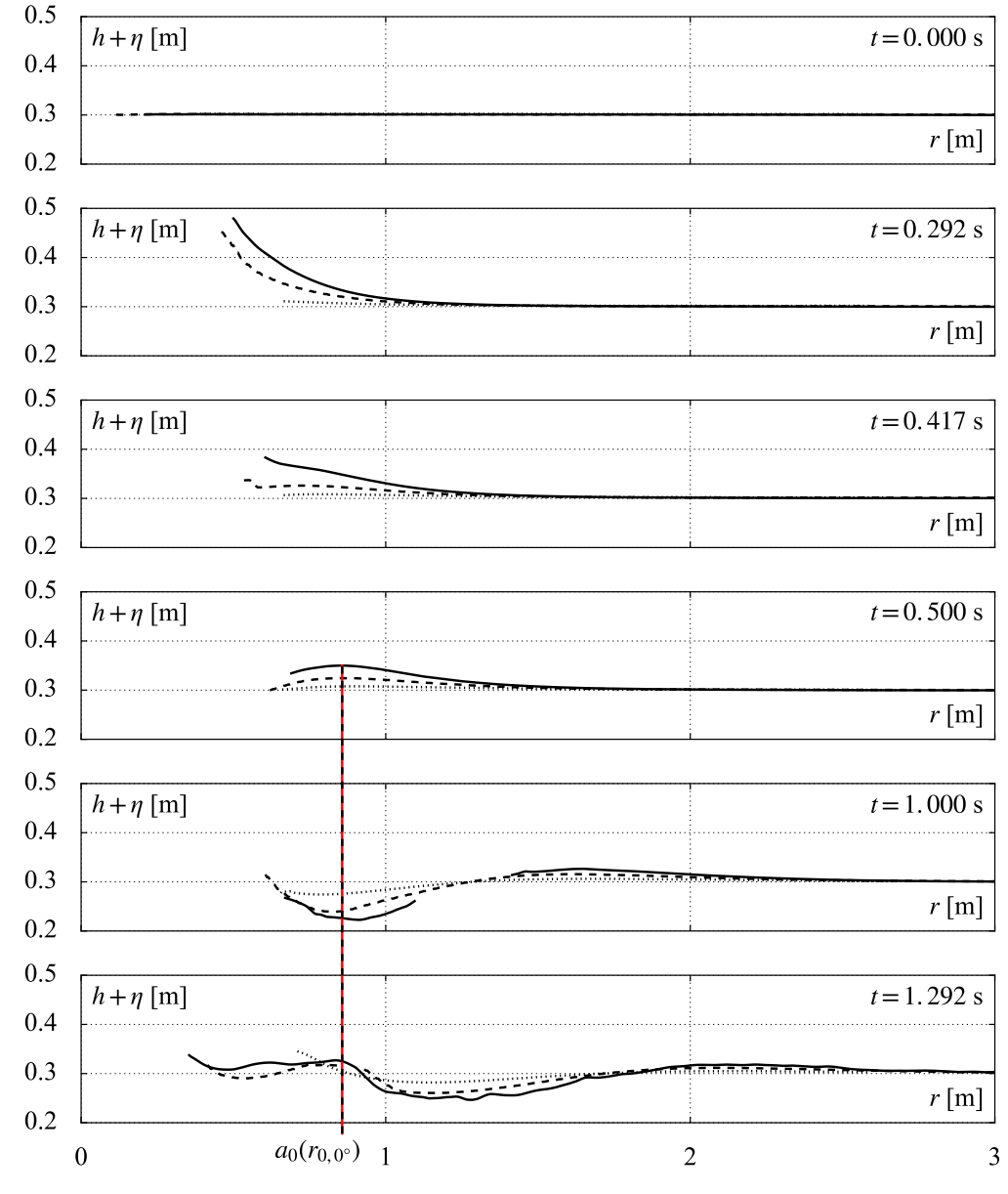

Fig. 4.27 Profile plots including impact radius r_0 and initial first wave crest amplitude $a_{0,c1}$ for $\mathsf{F} = 2.65$, $M = 0.44$, $S = 0.40$, $B = 1.67$, $\alpha_{\text{eff}} = 51.4°$, and $\mathsf{P} = 1.08$ at $\gamma = 0°$ (—), 45° (− −), and 90° (· · ·) at different times

As shown in Figure 4.27, the wave generation and propagation process is divided into a slide impact and a wave propagation zone. The former is strongly affected by the impact of the slide mass as well as the generation and collapse of the impact crater, involving turbulence and air entrainment. In the latter, wave characteristics, e.g. wave

amplitudes, are observable and consequently quantifiable (Figure 4.28). While no distinct wave characteristics may be traced within the impact zone, its boundary to the wave propagation zone represents the location where spatial wave propagation starts. Beyond r_0, wave characteristics are described based on the surrogate radial wave propagation distance

$$r^* = r - r_0. \tag{4.1}$$

The equations for predicting key wave characteristics presented hereinafter are exclusively defined for $r^* \geq 0$.

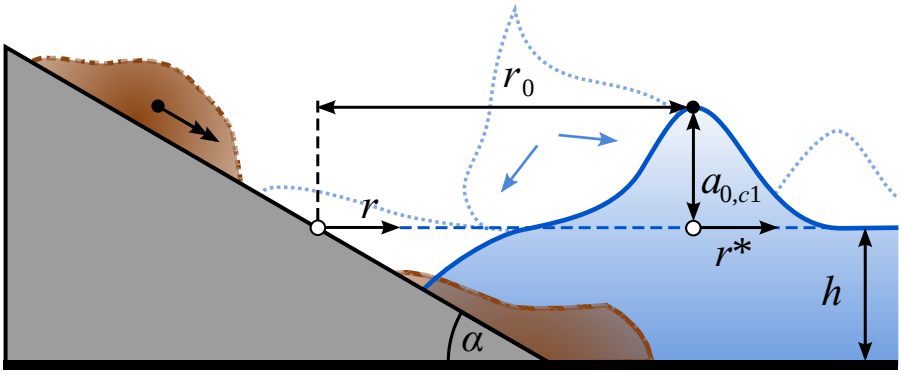

Fig. 4.28 Definition plot of impact radius r_0 and initial wave amplitude of the first wave crest $a_{0,c1}$

The relative radial wave propagation distance r/h is the sum of the relative impact radius R_0 and the relative surrogate radial wave propagation distance R^*

$$\frac{r}{h} = \frac{r_0}{h} + \frac{r^*}{h} = R_0 + R^*. \tag{4.2}$$

For spatial wave propagation, R_0 varies with the wave propagation angle γ (Figure 4.29) and is governed by the impulse product parameter P, the relative slide width B, and the effective slide impact angle $\alpha_{\text{eff}} = (6/7)\alpha$. For $\gamma = 0°$ and $90°$ the measured relative impact radii R_0 are fitted with

$$R_{0,0°} = \frac{r_{0,0°}}{h} = 2.5\,(\mathsf{P}B\cos\alpha_{\text{eff}})^{0.25} \tag{4.3}$$

$$R_{0,90°} = \frac{r_{0,90°}}{h} = \left(\frac{B}{2}\right) + 1.5\,(\mathsf{P}\cos\alpha_{\text{eff}})^{0.25}. \tag{4.4}$$

$R_{0,0°}$ follows the same orientation as the propagation direction of the slide at impact with the water surface (Figure 4.29).

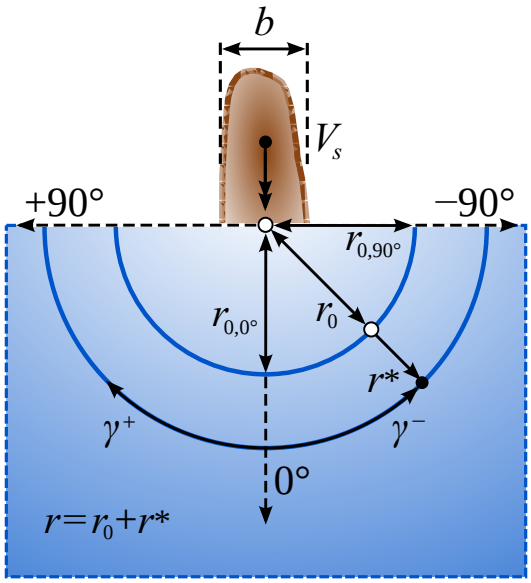

Fig. 4.29 Definition plot of impact radius r_0 and r^* for spatial impulse wave propagation

In both equations, the cosine of the effective slide impact angle α_{eff} is included twice, since it is already part of P. P is taken into account as a purely 2D parameter, which describes the momentum transfer from the slide to the water column, and α_{eff} is therefore included twice to take 3D effects into account. Compared with the dimensionless parameters included in P, the cosine of α_{eff} has the strongest influence on the impact radius with an overall exponent of 0.75. Note, that B is only included as a summand in $R_{0,90°}$ and represents its lower boundary. For arbitrary values of γ between 0° and 90°, the relative impact radius R_0 is defined by an ellipse in polar form as

$$R_0(\gamma) = \sqrt{\frac{R_{0,0°}^2 R_{0,90°}^2}{R_{0,0°}^2 \sin^2\gamma + R_{0,90°}^2 \cos^2\gamma}}. \tag{4.5}$$

In Figure 4.30, the measured relative impact radii $R_{0,\text{meas}}$ for all γ are plotted versus predicted $R_{0,\text{pred}}$ with an coefficient of determination of $R^2 = 0.71$.

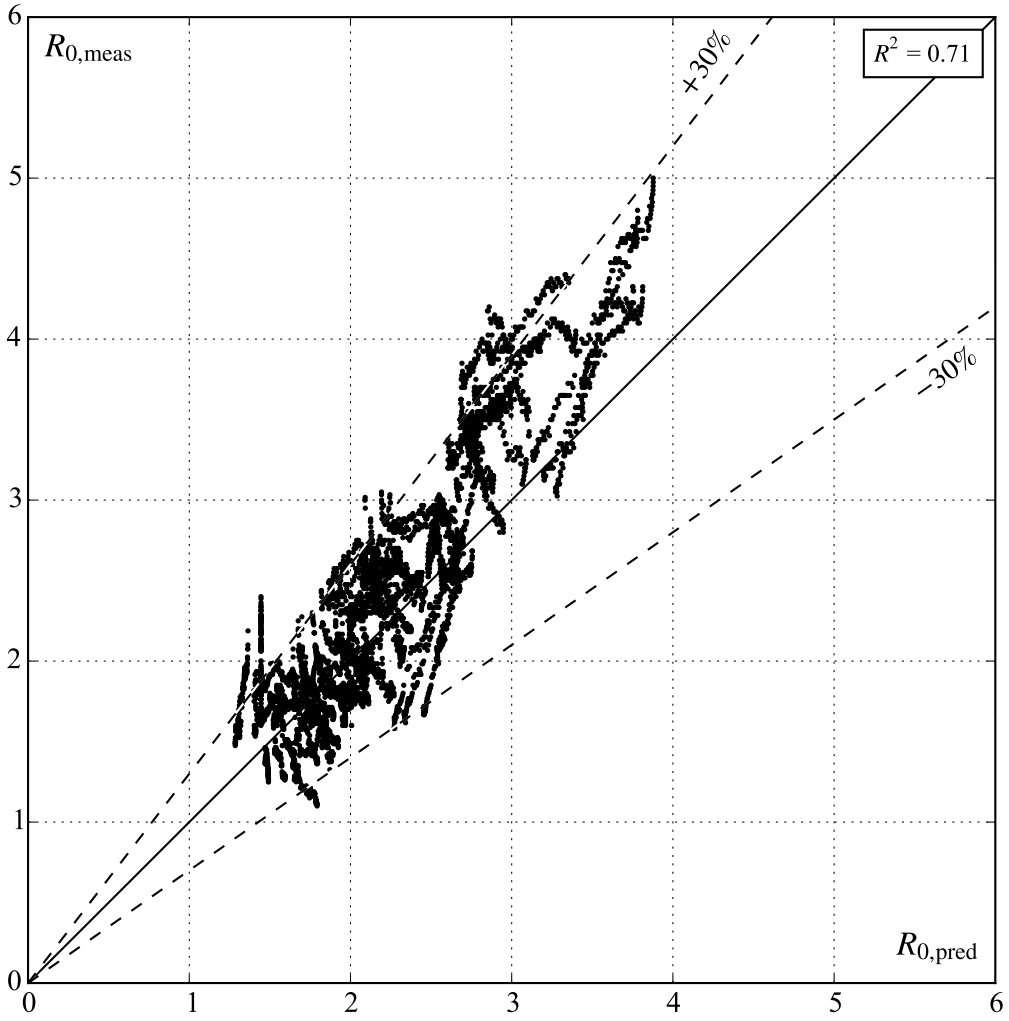

Fig. 4.30 Measured impact radii $R_{0,\text{meas}}$ versus predicted $R_{0,\text{pred}}$ based on Eq. (4.5)

4.3.4.2 Initial wave crest amplitude

The initial first wave crest amplitude $a_{0,c1}$ represents the maximum wave crest elevation for $\gamma = 0°$ (Figure 4.28). The relative initial first wave crest amplitudes $a_{0,c1}/a_{c1}(r_0, \gamma)$ are plotted versus the wave propagation angle γ in Figure 4.31. The radial gradient of the wave crest is 0 for $\gamma = 0°$ and increases up to an inflection point at γ between 30° and 50°. For further increasing values of γ, the gradient decreases again. For the experiments with slide impact angles $\alpha = 30°$, 45°, and 60°, a_{c1} at $\gamma = 90°$ accounts for 5% to 20% of $a_{0,c1}$. Only the experiments with $\alpha = 90°$ feature a smaller relative decrease to approximately 35% to 50% of $a_{0,c1}$.

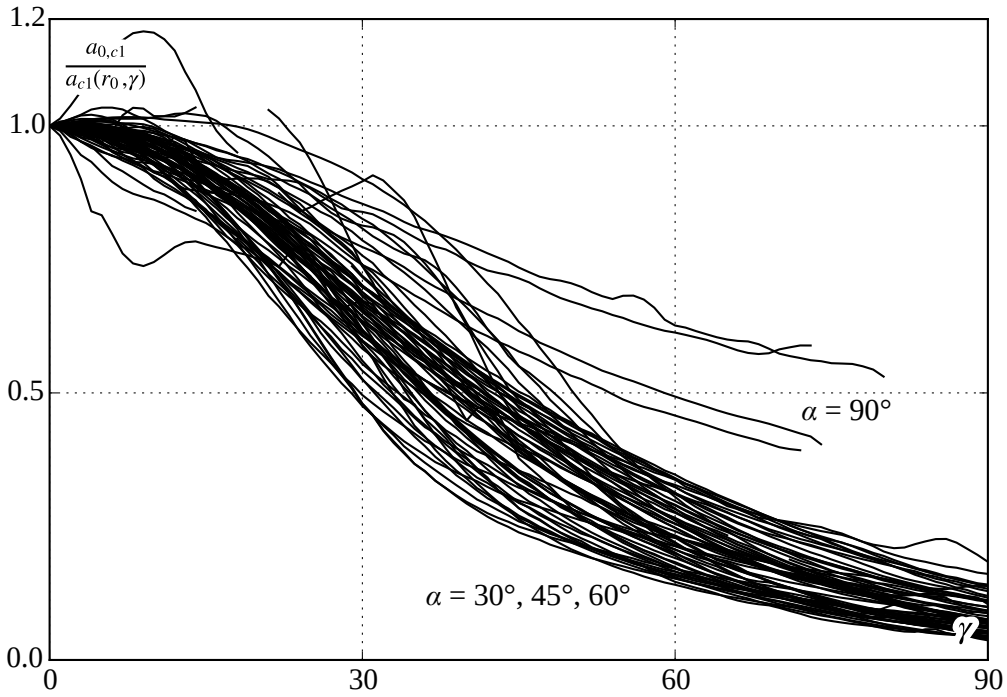

Fig. 4.31 Relative initial wave crest amplitudes $a_{0,c1}/a_{c1}(r_0,\gamma)$ versus wave propagation angle γ

The relative initial first wave crest amplitude $A_{0,c1}$ for $\gamma = 0°$ is governed by the impulse product parameter P, the relative slide width B, and effective slide impact angle α_{eff}. It is defined as

$$A_{0,c1} = \frac{a_{0,c1}}{h} = 0.2\mathsf{P}^{0.5} B^{0.75} \left(\cos\alpha_{\text{eff}}\right)^{0.25}. \tag{4.6}$$

By analogy with the impact radius R_0, the cosine of the effective slide impact angle α_{eff} is included twice into Eq. (4.6) to take spatial effects into account. With an exponent of 0.75, the relative slide width B has the strongest influence. For arbitrary γ between 0° and 90°, the relative initial wave crest amplitude $A_{c1} = a_{c1}/h$ at R_0 is defined as

$$A_{c1}(R_0) = A_{0,c1}\left[\operatorname{sech}\left(3.2\frac{\gamma}{90°}\right)\right]^{\cos\alpha_{\text{eff}}}. \tag{4.7}$$

Eq. (4.7) retraces the elevation of the initial first wave crest by accounting for the inflection point with a hyperbolic secant function. The effect of the slide impact angle α on the crest elevation (Section 4.3.2 and Figure 4.31) is included in the exponent. In Figure 4.7, the measured initial first wave crest amplitudes $A_{c1,\text{meas}}(R_0)$ for all γ are plotted versus predicted $A_{c1,\text{pred}}(R_0)$ with an coefficient of determination of $R^2 = 0.91$.

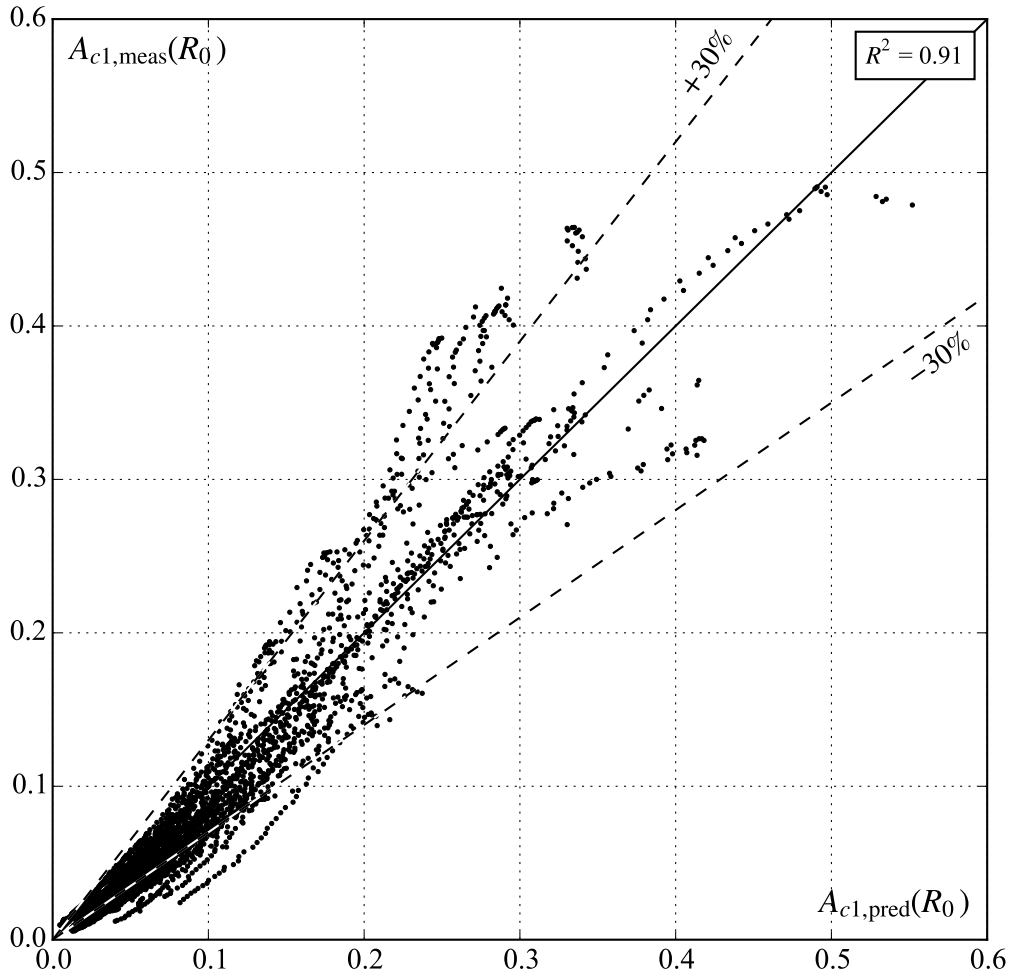

Fig. 4.32 Measured initial first wave crest amplitudes $A_{c1,\mathrm{meas}}(R_0)$ versus predicted $A_{c1,\mathrm{pred}}(R_0)$ based on Eq. (4.7)

4.3.5 Wave propagation zone

4.3.5.1 Wave amplitude decay

First wave crest amplitude

The first wave crest amplitude a_{c1} is defined as the crest elevation above the still water surface of the first outgoing wave as shown in Figure 4.5. In prototype scenarios, a_{c1} is the first part of the the wave train to impact the shoreline or dam structure. With a coefficient of determination of $R^2 = 0.89$, the relative first wave crest amplitudes $A_{c1} = a_{c1}/h$ measured in the experiments can be approximated by

$$A_{c1}\left(R^*, \gamma\right) = A_{0,c1} \exp\left(-0.4 A_{0,c1}^{-0.3} \sqrt{R^*}\right) \left[\operatorname{sech}\left(3.2 \frac{\gamma}{90°}\right)\right]^{\cos\alpha_{\text{eff}} \exp\left(-0.15\sqrt{R^*}\right)}. \quad (4.8)$$

Eq. (4.8) is an extended version of Eq. (4.7) including the relative surrogate wave propagation distance R^* to describe the wave decay effect. While the first exponential function accounts for the amplitude decay in propagation direction, the second exponential function, contained in the exponent of the hyperbolic secant function, includes the wave crest spreading normal to the propagation direction discussed in Section 4.3.2. Figures 4.33 and 4.34 show measured data in relation to Eq. (4.8). In total, $n = 208{,}685$ data points were included into the analysis. The histogram in Figure 4.33 shows the distribution of the measured wave amplitudes over the predicted values. In the box plot underneath, the box defines the first and the third quartiles, with the band inside as the second quartile. The whiskers depict the 5^{th} and 95^{th} percentiles, i.e. 90% of the data points scatter between -45% and $+25\%$. Overall, Eq. (4.8) is slightly overestimating the measured wave amplitudes. Outliers include data points affected by measurement errors or inaccuracies related to the wave feature tracking process as well as correctly captured wave amplitudes. Therefore, no outliers were excluded for the plots. In Figure 4.34, box plots are shown for the relative wave propagation distance r/h between 1.5 and 16.1 as well as wave propagation angles γ between 0° and 90°. The deviation scatter is largest close to the impact location up to $r/h = 9$. However, note that this section contains most measured data. Wave amplitudes for $\gamma > 60°$ are slightly more overestimated, while the scatter increases too.

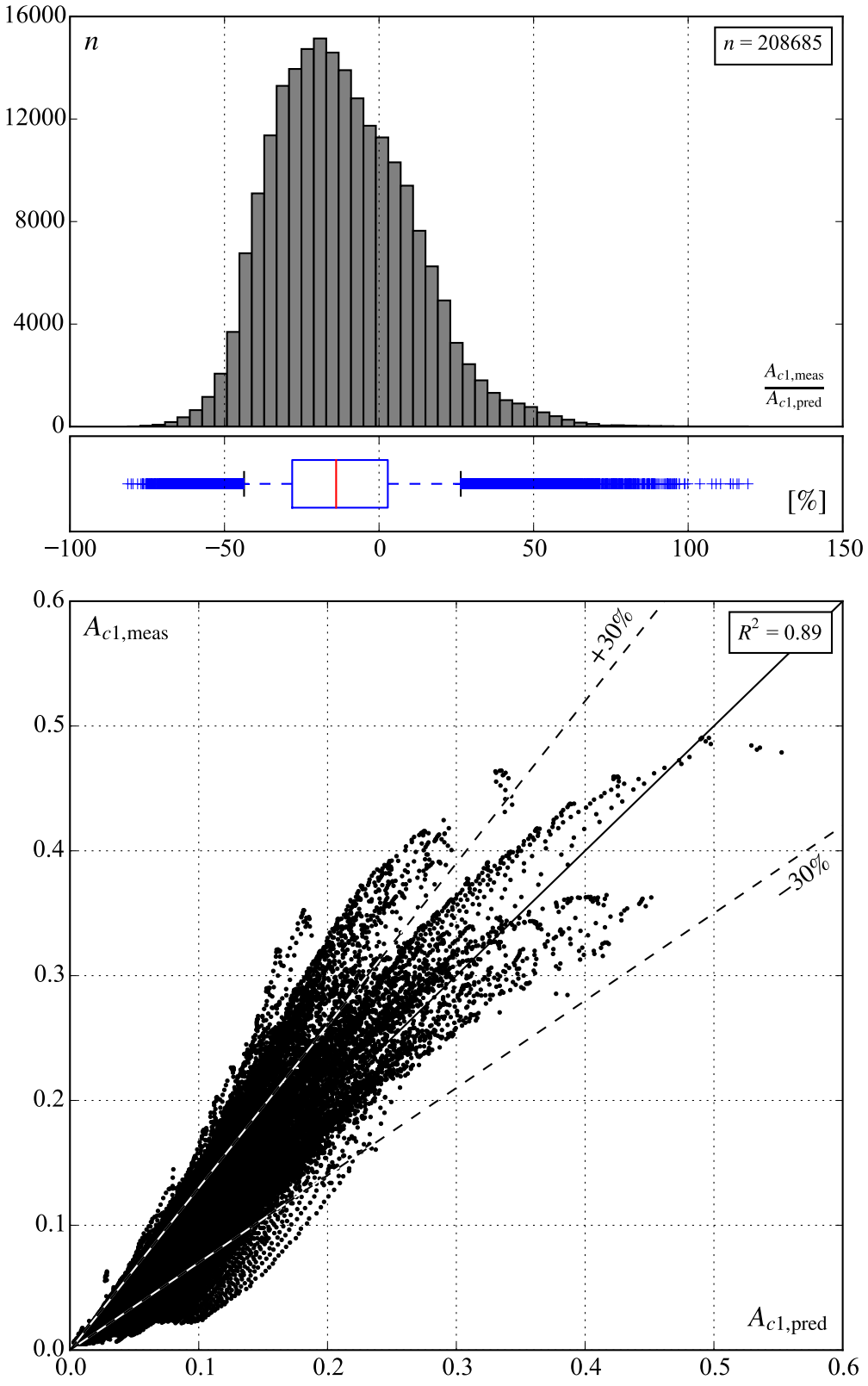

Fig. 4.33 Histogram, box plot with whiskers at 5th and 95th percentiles, and scatter plot of measured relative first wave crest amplitude $A_{c1,meas}$ versus predicted $A_{c1,pred}$ based on Eq. (4.8)

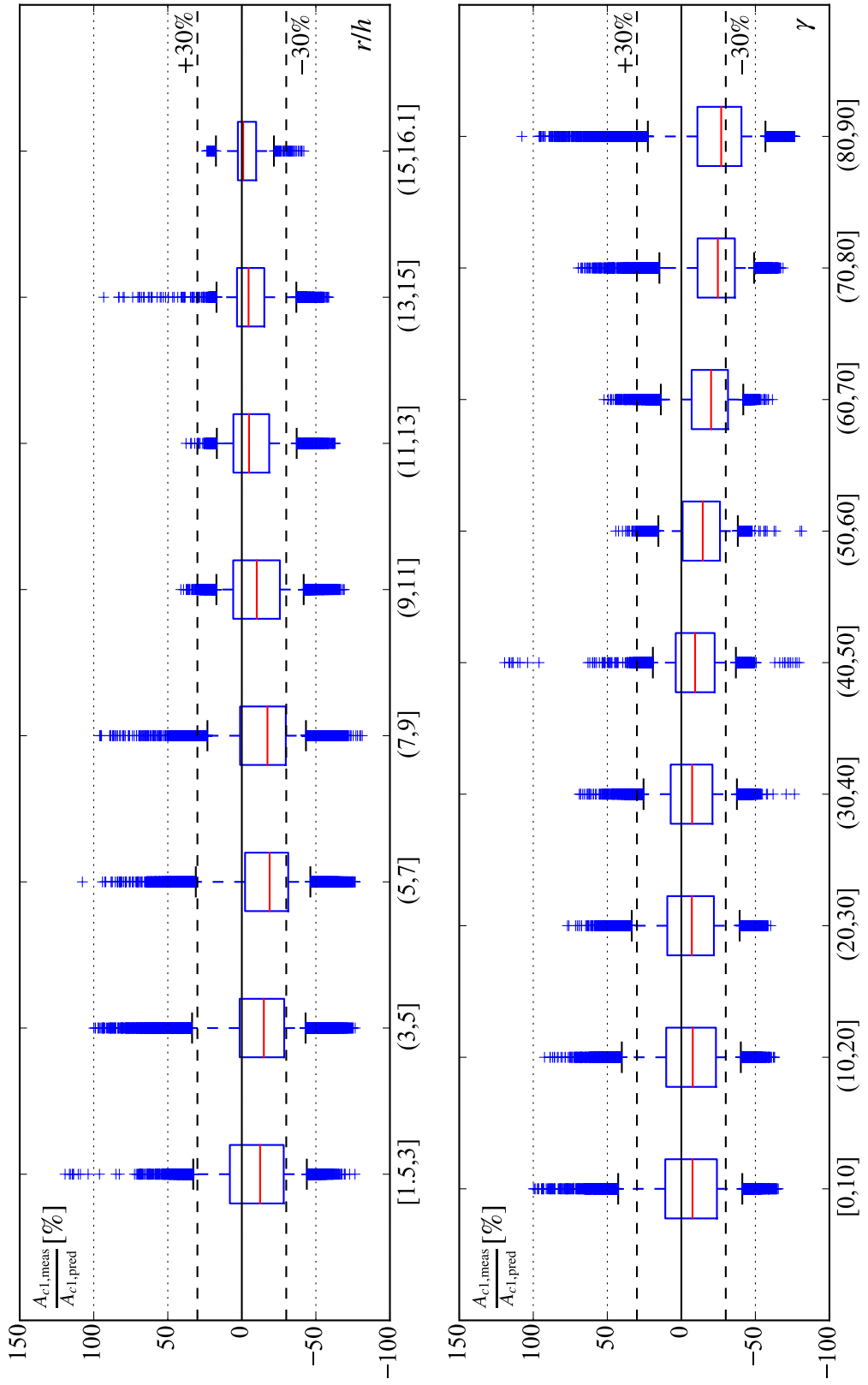

Fig. 4.34 Box plots with whiskers at 5$^{\mathrm{th}}$ and 95$^{\mathrm{th}}$ percentiles for measured relative first wave crest amplitude $A_{c1,\mathrm{meas}}$ over predicted $A_{c1,\mathrm{pred}}$ versus relative propagation distance r/h and wave propagation angle γ based on Eq. (4.8)

First wave trough amplitude

The first wave trough amplitude a_{t1} is defined as the depression below the still water surface of the first outgoing wave as shown in Figure 4.5. In analogy with a_{c1}, the relative initial first wave trough amplitude $A_{0,t1}$ at R_0 and $\gamma = 0°$ is defined as

$$A_{0,t1} = \frac{a_{0,t1}}{h} = 0.35 \left(\mathsf{P} B \cos \alpha_{\text{eff}}\right)^{0.5}. \tag{4.9}$$

The impulse product parameter P has the same influence as in Eq. (4.6). The effect of B is slightly reduced, while the cosine of α_{eff} has the highest exponent with 0.75 considering it is also included in P. With a coefficient of determination of $R^2 = 0.91$, the relative first wave trough amplitudes $A_{t1} = a_{t1}/h$ measured in the experiments are approximated by

$$A_{t1}\left(R^*, \gamma\right) = A_{0,t1} \exp\left(-0.4 A_{0,t1}^{-0.3} \sqrt{R^*}\right) \left[\operatorname{sech}\left(3.6 \frac{\gamma}{90°}\right)\right]^{\cos \alpha_{\text{eff}} \exp\left(-0.15 \sqrt{R^*}\right)}. \tag{4.10}$$

In total, $n = 186{,}145$ data points were included into the analysis. The measured amplitudes tend to be slightly underestimated by Eq. (4.10) and 90% of the data points scatter between -25% and $+40\%$. Besides replacing $A_{0,c1}$ with $A_{0,t1}$, the only difference between Eqs. (4.8) and (4.10) is a higher factor in the hyperbolic secant function. Figure 4.36 shows the deviation of the measured values plotted versus the relative wave propagation distance r/h and the wave propagation angle γ. The underestimation is highest close to the impact location and is slightly increasing again for $r/h > 7$ as well as predominant at γ between 40° and 60°.

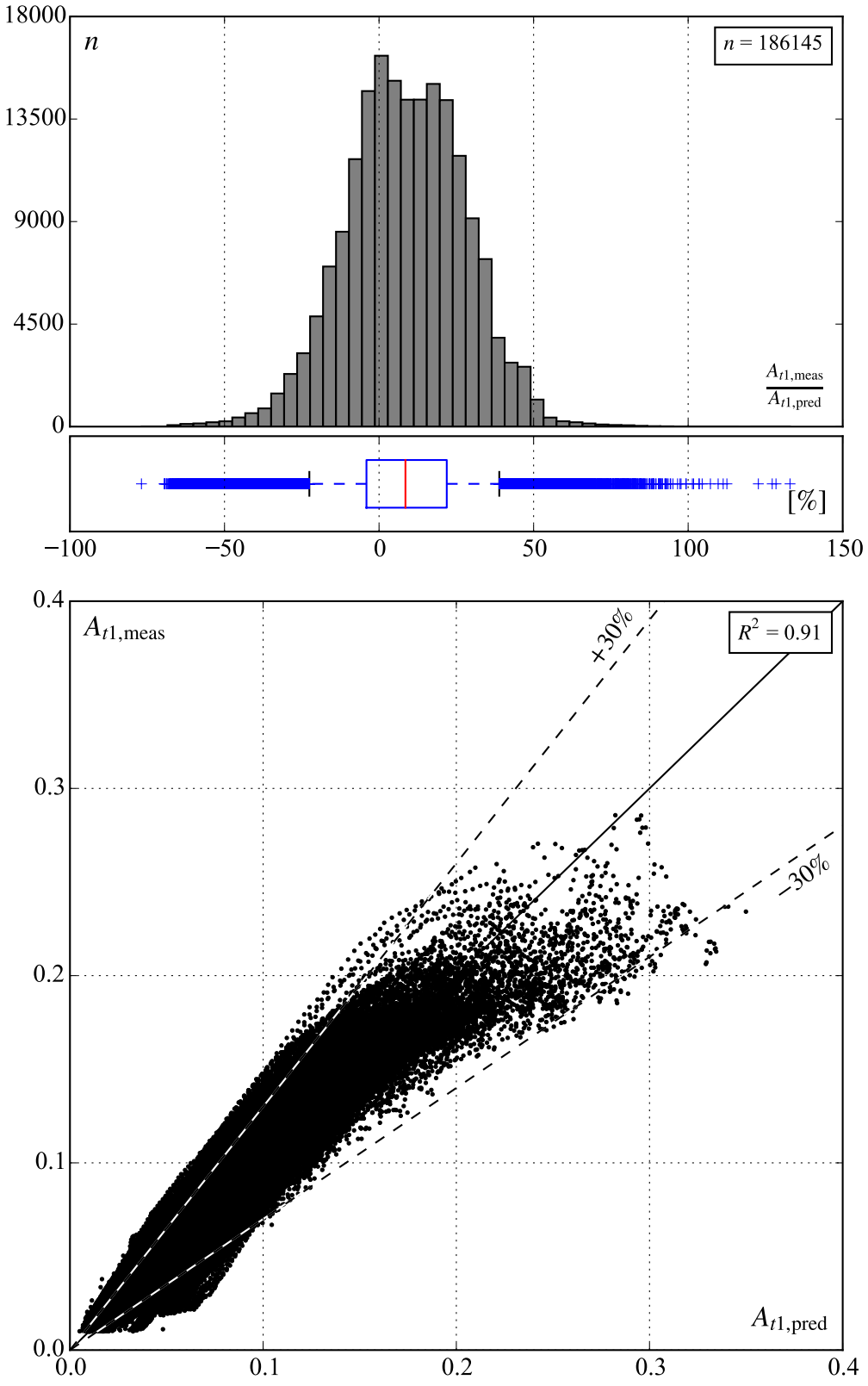

Fig. 4.35 Histogram, box plot with whiskers at 5$^{\mathrm{th}}$ and 95$^{\mathrm{th}}$ percentiles, and scatter plot of measured relative first wave trough amplitude $A_{t1,\mathrm{meas}}$ versus predicted $A_{t1,\mathrm{pred}}$ based on Eq. (4.10)

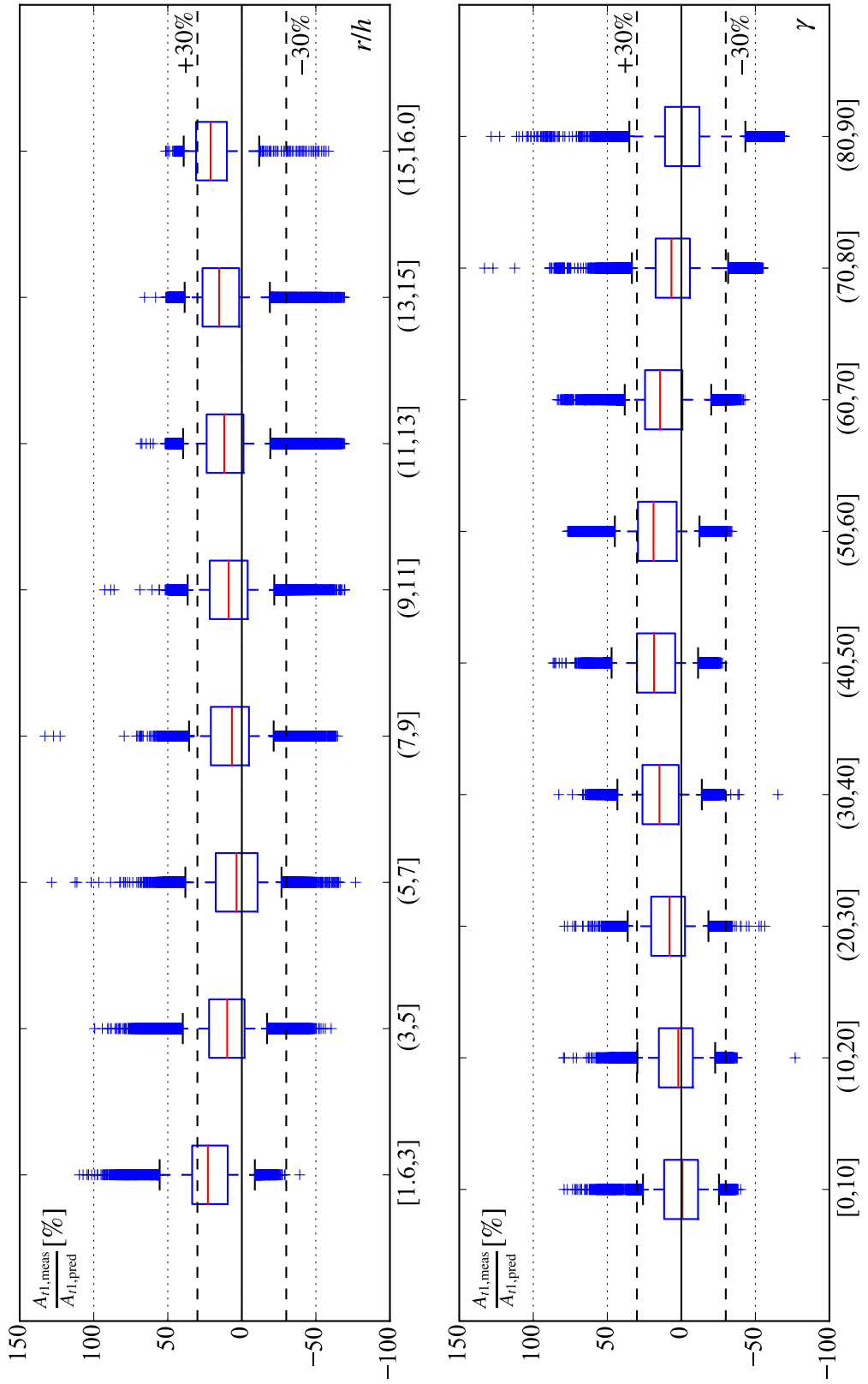

Fig. 4.36 Box plots with whiskers at 5$^{\mathrm{th}}$ and 95$^{\mathrm{th}}$ percentiles for measured relative first wave trough amplitude $A_{t1,\mathrm{meas}}$ over predicted $A_{t1,\mathrm{pred}}$ versus relative propagation distance r/h and wave propagation angle γ based on Eq. (4.10)

Second wave crest amplitude

The second wave crest amplitude a_{c2} is defined as the crest elevation above the still water surface of the second outgoing wave as shown in Figure 4.5. The relative initial second wave crest amplitude $A_{0,c2}$ at R_0 and $\gamma = 0°$ is defined as

$$A_{0,c2} = \frac{a_{0,c2}}{h} = 0.14 \left(\mathsf{P} B \cos \alpha_{\text{eff}}\right)^{0.25}. \tag{4.11}$$

The overall exponent of all parameters is reduced by half compared to Eq. (4.9), with the cosine of α_{eff} having the highest exponent with 0.5 considering it is also included in P. With a coefficient of determination of $R^2 = 0.69$, the relative second wave crest amplitudes $A_{c2} = a_{c2}/h$ measured in the experiments are approximated by

$$A_{c2}\left(R^*, \gamma\right) = A_{0,c2} \exp\left(-0.1 A_{0,c2}^{-0.3} \sqrt{R^*}\right) \left[\operatorname{sech}\left(3 \frac{\gamma}{90°}\right)\right]^{\cos \alpha_{\text{eff}} \exp\left(-0.15 \sqrt{R^*}\right)}. \tag{4.12}$$

In total, $n = 211{,}960$ data points were included into the analysis. Compared to the amplitudes of the first wave, the fit is subject to larger scatter and 90% of the data points lie within -60% to $+50\%$ (Figure 4.37). The first exponential function describes a lower decay rate than Eqs. (4.8) and (4.10). Also the factor contained within the hyperbolic secant function is slightly lower. Figure 4.38 shows, that the largest scatter is found close to the slide impact zone with $r/h \leq 5$ and for wave propagation angles $\gamma > 60°$. Although the scatter for $\gamma > 60°$ increases significantly above the $+30\%$ line, most of the data points are overestimated by Eq. (4.12). While the first wave crest is generated directly by the slide, the second wave crest results from the collapse of the impact crater, which is subject to strong turbulence and air entrainment. The increased uncertainty in the prediction of a_{c2} relates to its unsteady generation process.

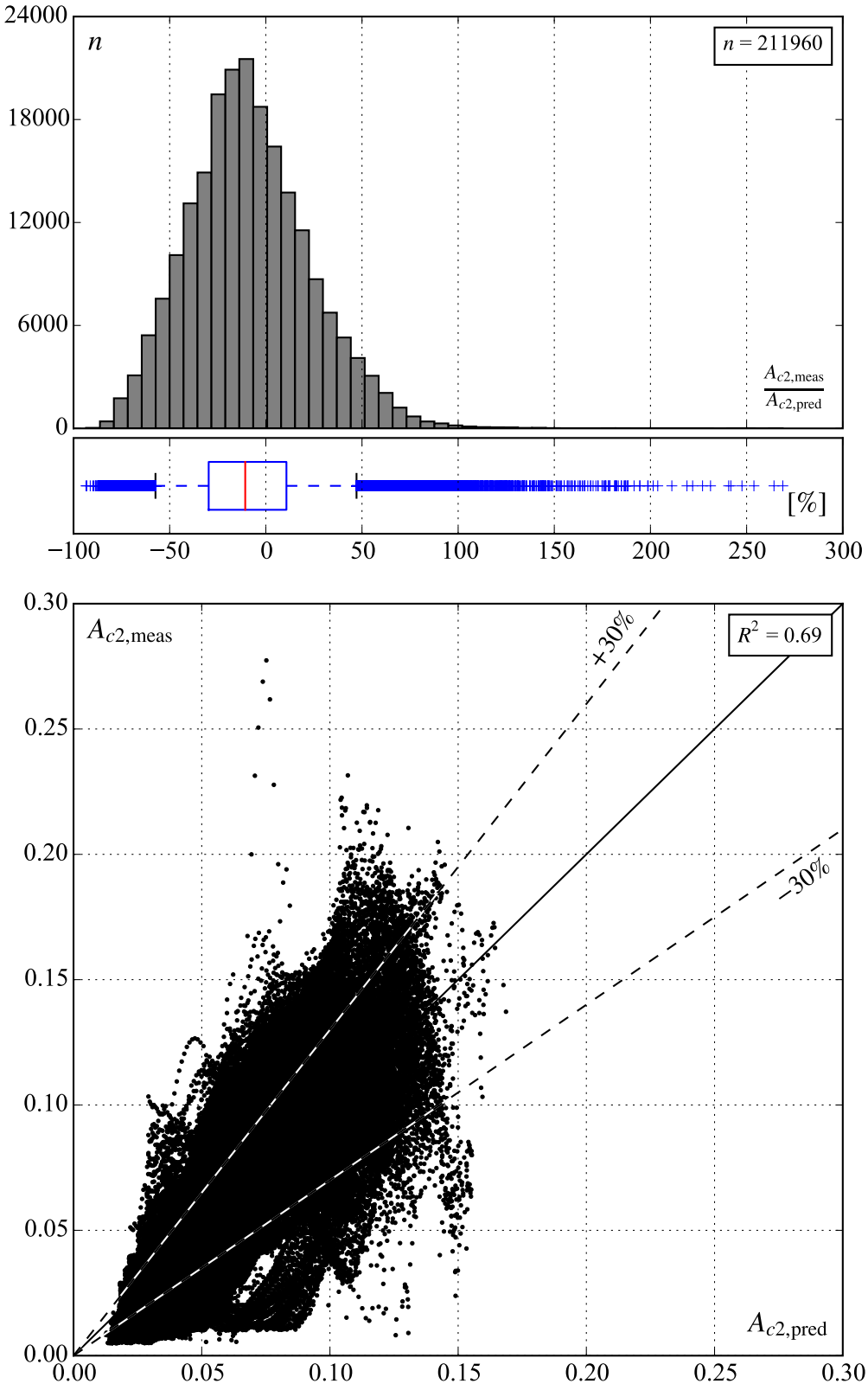

Fig. 4.37 Histogram, box plot with whiskers at 5th and 95th percentiles, and scatter plot of measured relative second wave crest amplitude $A_{c2,meas}$ versus predicted $A_{c2,pred}$ based on Eq. (4.12)

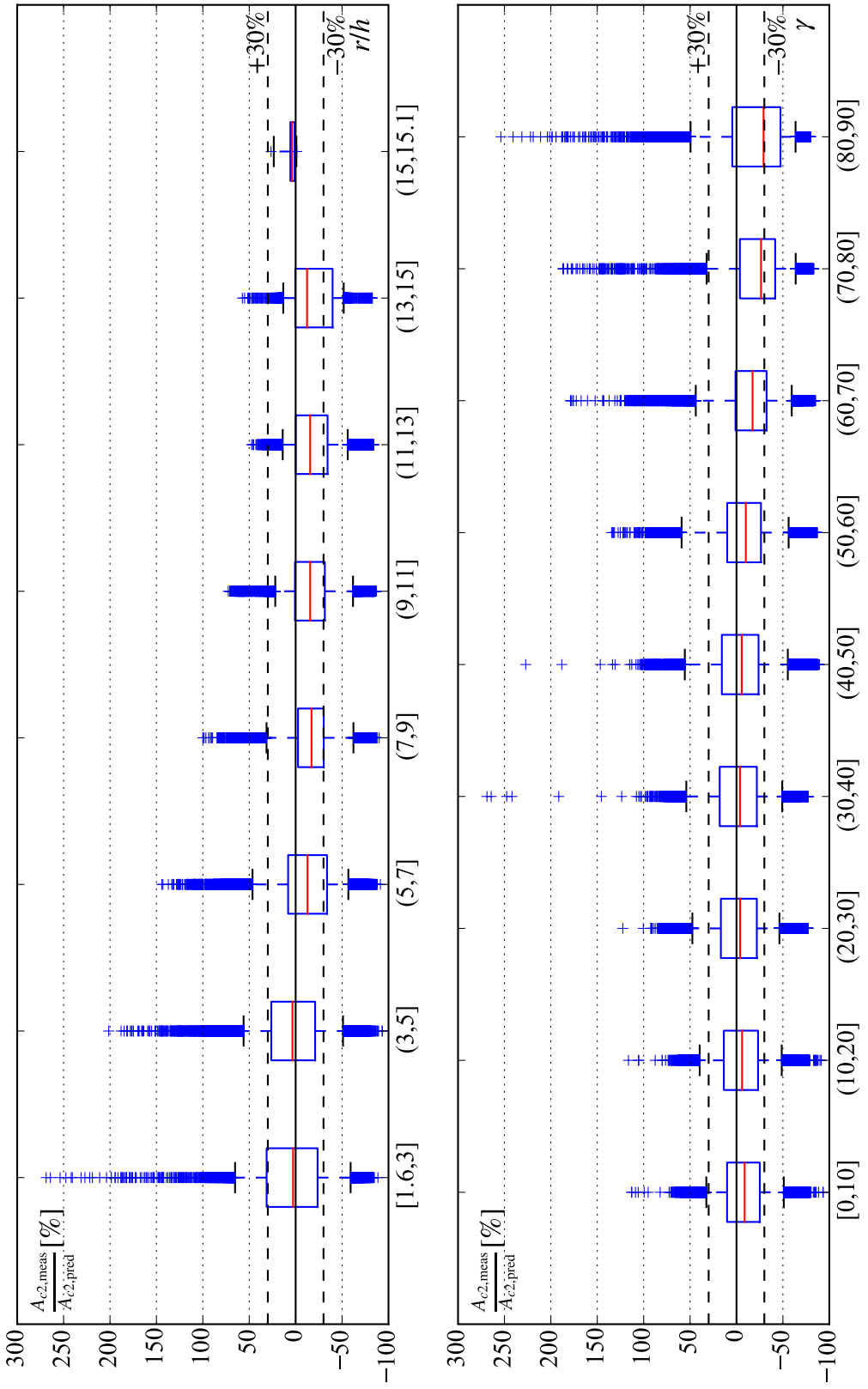

Fig. 4.38 Box plots with whiskers at 5$^{\mathrm{th}}$ and 95$^{\mathrm{th}}$ percentiles for measured relative second wave crest amplitude $A_{c2,\mathrm{meas}}$ over predicted $A_{c2,\mathrm{pred}}$ versus relative propagation distance r/h and wave propagation angle γ based on Eq. (4.12)

4.3.5.2 Wave height decay

The first wave height H_1 is defined as the distance between the water surface levels of the first wave crest and trough amplitude at the same location as shown in Figure 4.5. With a coefficient of determination of $R^2 = 0.93$, the relative first wave heights $Y_1 = H_1/h$ measured in the experiments are approximated by

$$Y_1\left(R^*, \gamma\right) = A_{c1} + A_{t1}. \tag{4.13}$$

In total, $n =$ 124,628 data points were included into the analysis with 90% scattering between -30% and $+25\%$ (Figure 4.39). Compared to its summands A_{c1} and A_{t1} (Eqs. 4.8 and 4.12), Y_1 features a smaller scatter. Figure 4.40 shows, that the highest scatter is found close to the impact location and for large γ.

4.3.5.3 Wave period

The first wave period T_1 is defined as the time difference between the initial uplifting of the first wave crest and the still water level intersection following the first wave trough at a certain position on the water surface (Figure 4.5). The relative first wave periods $T_1/(g/h)^{0.5}$ measured in the experiments are approximated with a coefficient of determination of $R^2 =$ 0.86 by

$$T_1\left(R^*, \gamma\right)(g/h)^{0.5} = 10\left(Y_1\right)^{0.2} + \frac{R^*}{2}. \tag{4.14}$$

In total, $n =$ 86,243 data points were included into the analysis with 90% scattering between -10% and $+15\%$ (Figure 4.41). At the impact radius R_0, T_1 is governed exclusively by the relative first wave height Y_1 (Eq. 4.13). During propagation Y_1 decreases and the linear term including R^* increases. Figure 4.42 shows, that Eq. (4.14) tends to slightly underestimate T_1 for increasing γ, while it has a minimal trend of overestimation for increasing r/h.

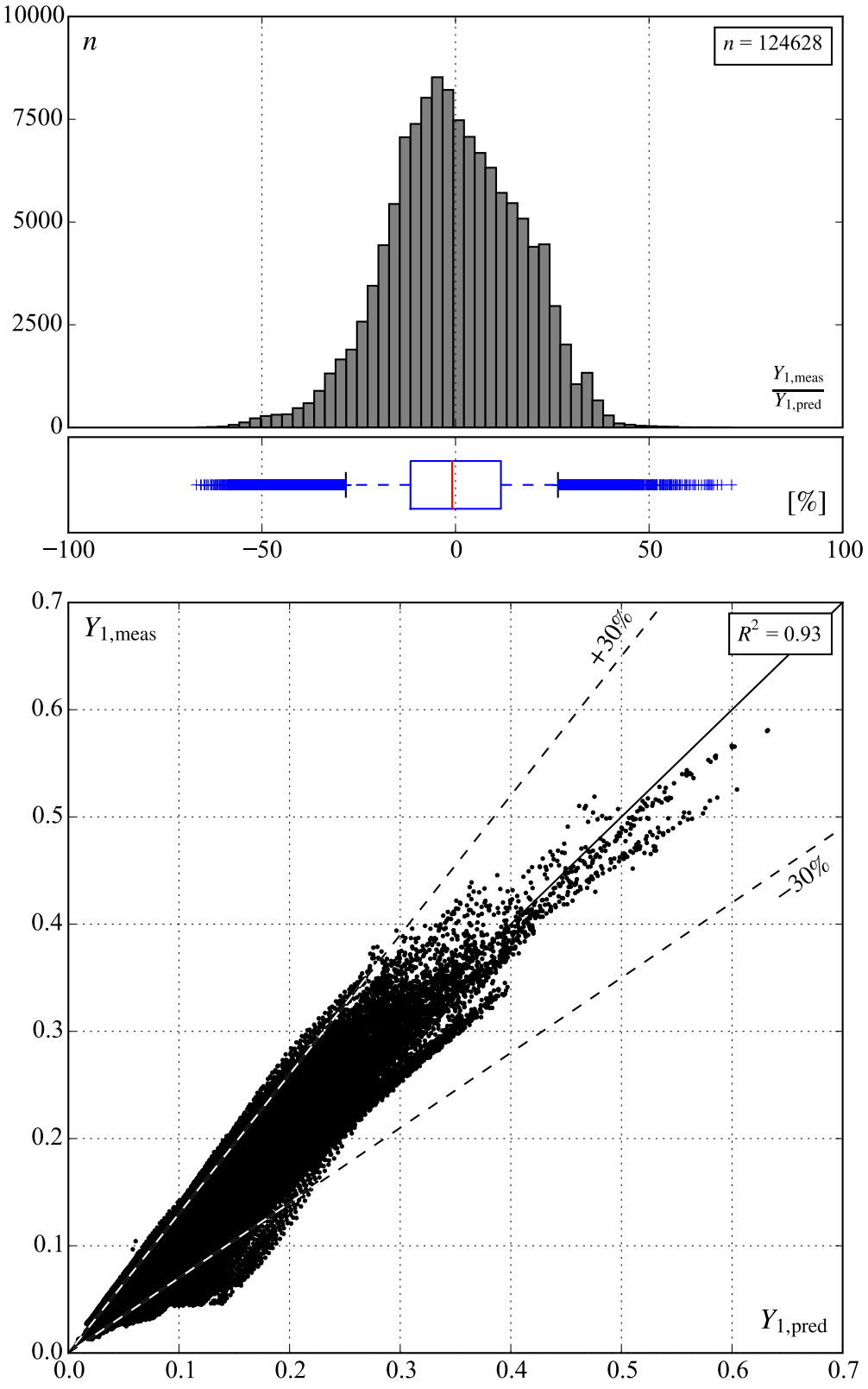

Fig. 4.39 Histogram, box plot with whiskers at 5th and 95th percentiles, and scatter plot of measured relative first wave height $Y_{1,meas}$ versus predicted $Y_{1,pred}$ based on Eq. (4.13)

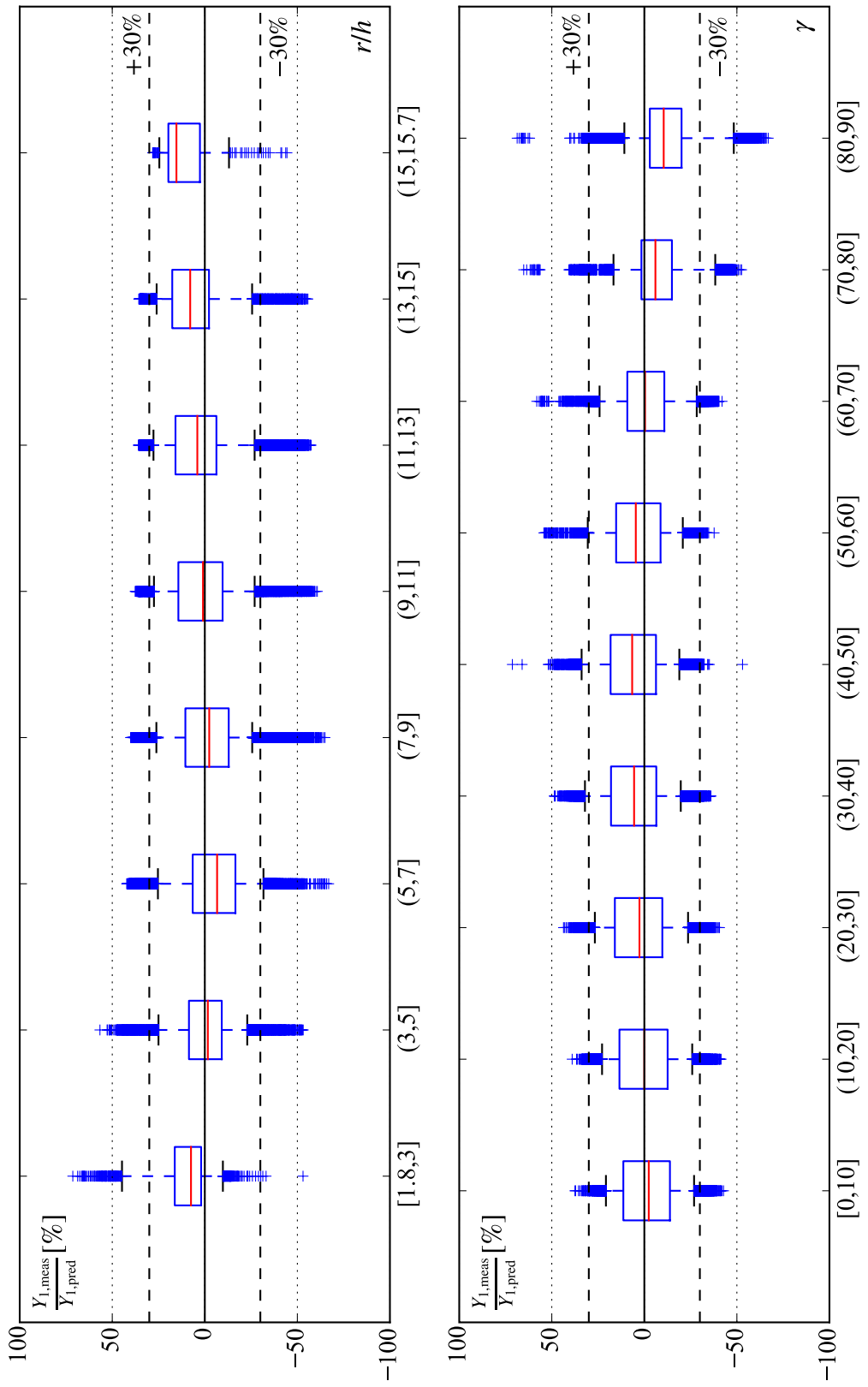

Fig. 4.40 Box plots with whiskers at 5$^{\text{th}}$ and 95$^{\text{th}}$ percentiles for measured relative first wave height $Y_{1,\text{meas}}$ over predicted $Y_{1,\text{pred}}$ versus relative propagation distance r/h and wave propagation angle γ based on Eq. (4.13)

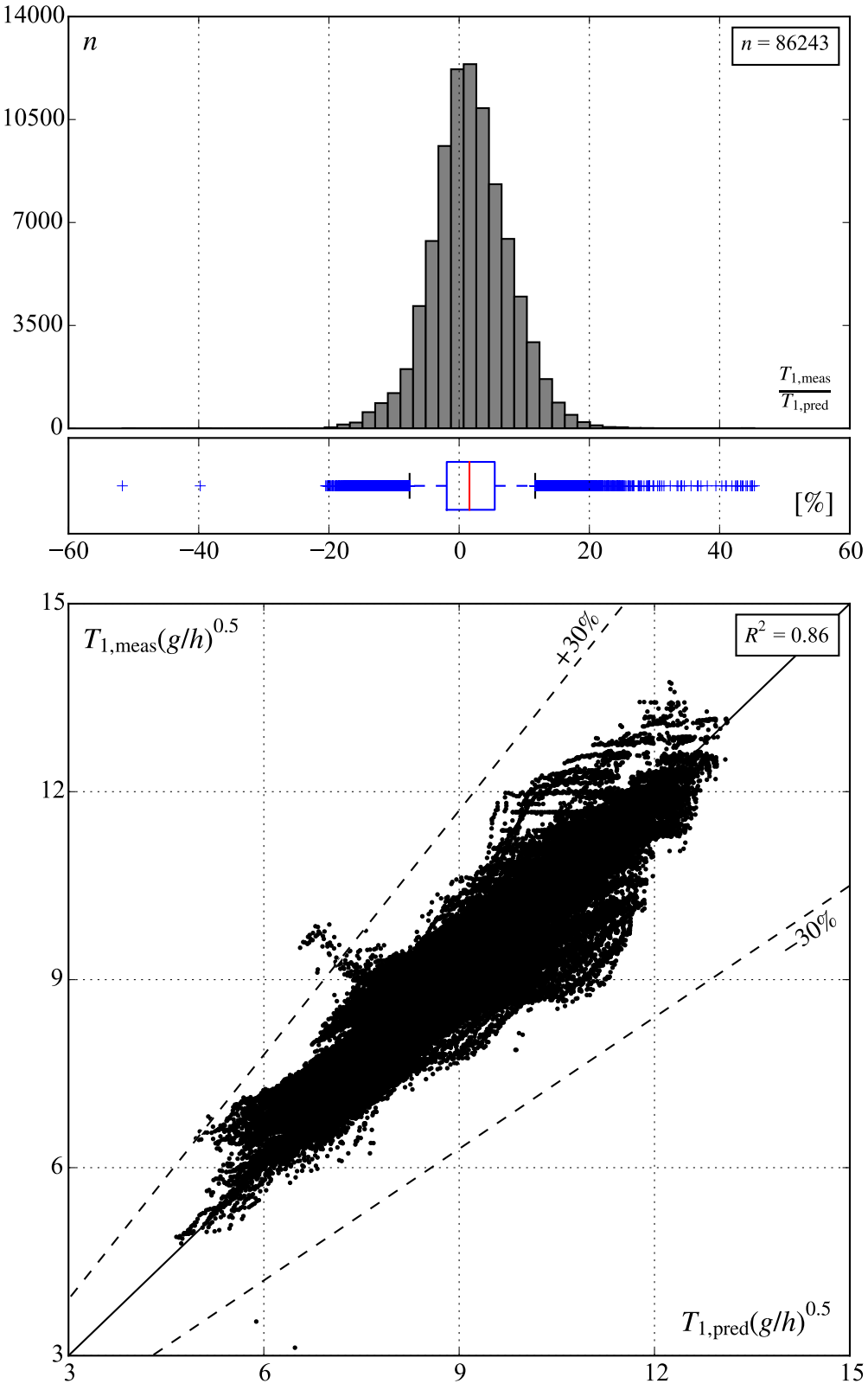

Fig. 4.41 Histogram, box plot with whiskers at 5$^{\text{th}}$ and 95$^{\text{th}}$ percentiles, and scatter plot of measured relative first wave period $T_{1,\text{meas}}(g/h)^{0.5}$ versus predicted $T_{1,\text{pred}}(g/h)^{0.5}$ based on Eq. (4.14)

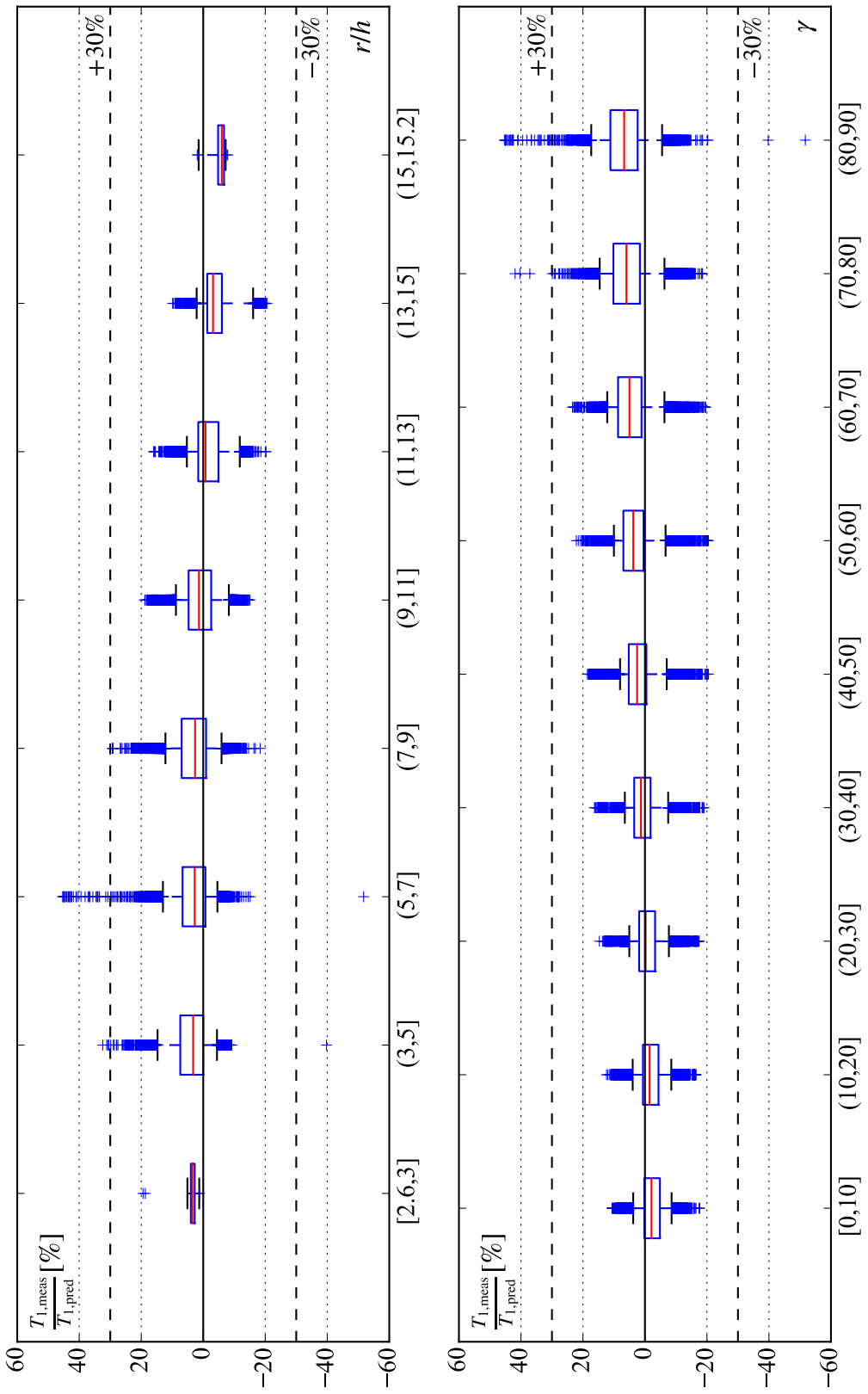

Fig. 4.42 Box plots with whiskers at 5$^{\mathrm{th}}$ and 95$^{\mathrm{th}}$ percentiles for measured relative first wave period $T_{1,\mathrm{meas}}(g/h)^{0.5}$ over predicted $T_{1,\mathrm{pred}}(g/h)^{0.5}$ versus relative propagation distance r/h and wave propagation angle γ based on Eq. (4.14)

4.3.5.4 Wave celerity

First wave crest celerity

The first wave crest celerity c_{c1} is defined as the propagation celerity of the first wave crest (Figure 4.5). The relative first wave crest celerities $c_{c1}/\sqrt{gh}$ measured in the experiments are approximated with a coefficient of determination of $R^2 = -0.06$ by

$$\frac{c_{c1}}{\sqrt{gh}} = 0.95\sqrt{1+A_{c1}}. \tag{4.15}$$

In total, $n = 131{,}217$ data points were included into the analysis with 90% scattering between -15% and $+10\%$ (Figure 4.43). Eq. (4.15) corresponds to 95% of the solitary wave celerity (Russell 1844). Figure 4.44 shows that c_{c1} is overestimated close to the impact location of the slide. No significant trend is observed for increasing wave propagation angles γ. Single tracked values of c_{c1} are strongly overestimated for $3 < r/h \leq 7$ and $\gamma > 70°$, which are regarded as defective outliers.

Second wave crest celerity

The second wave crest celerity c_{c2} is defined as the propagation celerity of the second wave crest (Figure 4.5). The relative second wave crest celerities $c_{c2}/\sqrt{gh}$ measured in the experiments are approximated with a coefficient of determination of $R^2 = -0.03$ with

$$\frac{c_{c2}}{\sqrt{gh}} = 0.7\sqrt{1+A_{c2}}. \tag{4.16}$$

In total, $n = 139{,}457$ data points were included into the analysis with 90% scattering between -25% and $+15\%$ (Figure 4.45). Eq. (4.16) corresponds to 70% of the solitary wave celerity (Russell 1844). Equally to c_{c1}, c_{c2} is overestimated close to the impact location as shown in Figure 4.46. However, for increasing r/h, c_{c2} is slightly underestimated. While the second quartile remains almost constant for increasing γ, the scatter range below -30% extends for $\gamma < 50°$.

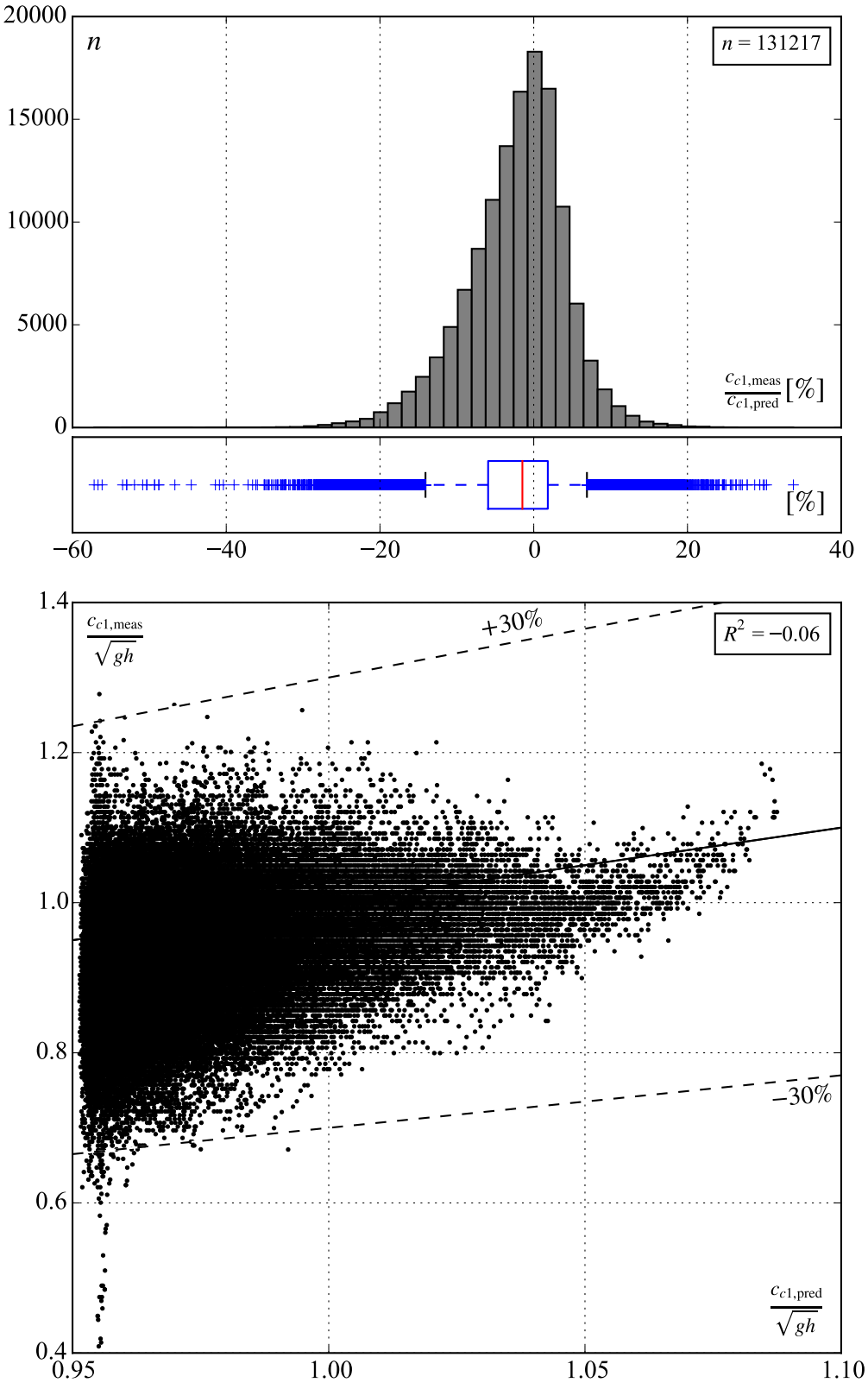

Fig. 4.43 Histogram, box plot with whiskers at 5$^{\mathrm{th}}$ and 95$^{\mathrm{th}}$ percentiles, and scatter plot of measured relative first wave crest celerity $c_{c1,\mathrm{meas}}/\sqrt{gh}$ versus predicted $c_{c1,\mathrm{pred}}/\sqrt{gh}$ based on Eq. (4.15)

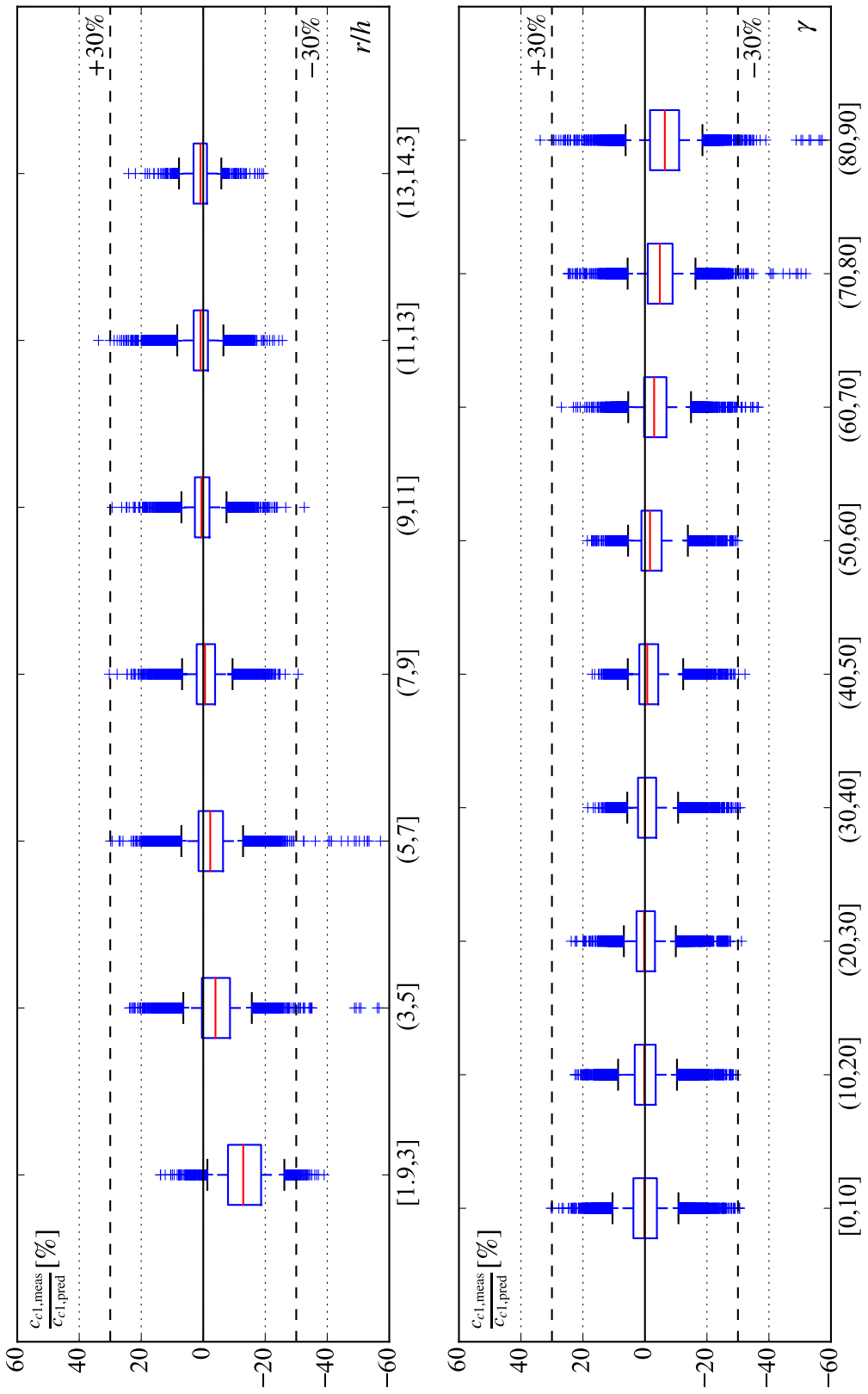

Fig. 4.44 Box plots with whiskers at 5$^{\mathrm{th}}$ and 95$^{\mathrm{th}}$ percentiles for measured relative first wave crest celerity $c_{c1,\mathrm{meas}}/\sqrt{gh}$ over predicted $c_{c1,\mathrm{pred}}/\sqrt{gh}$ versus relative propagation distance r/h and wave propagation angle γ based on Eq. (4.15)

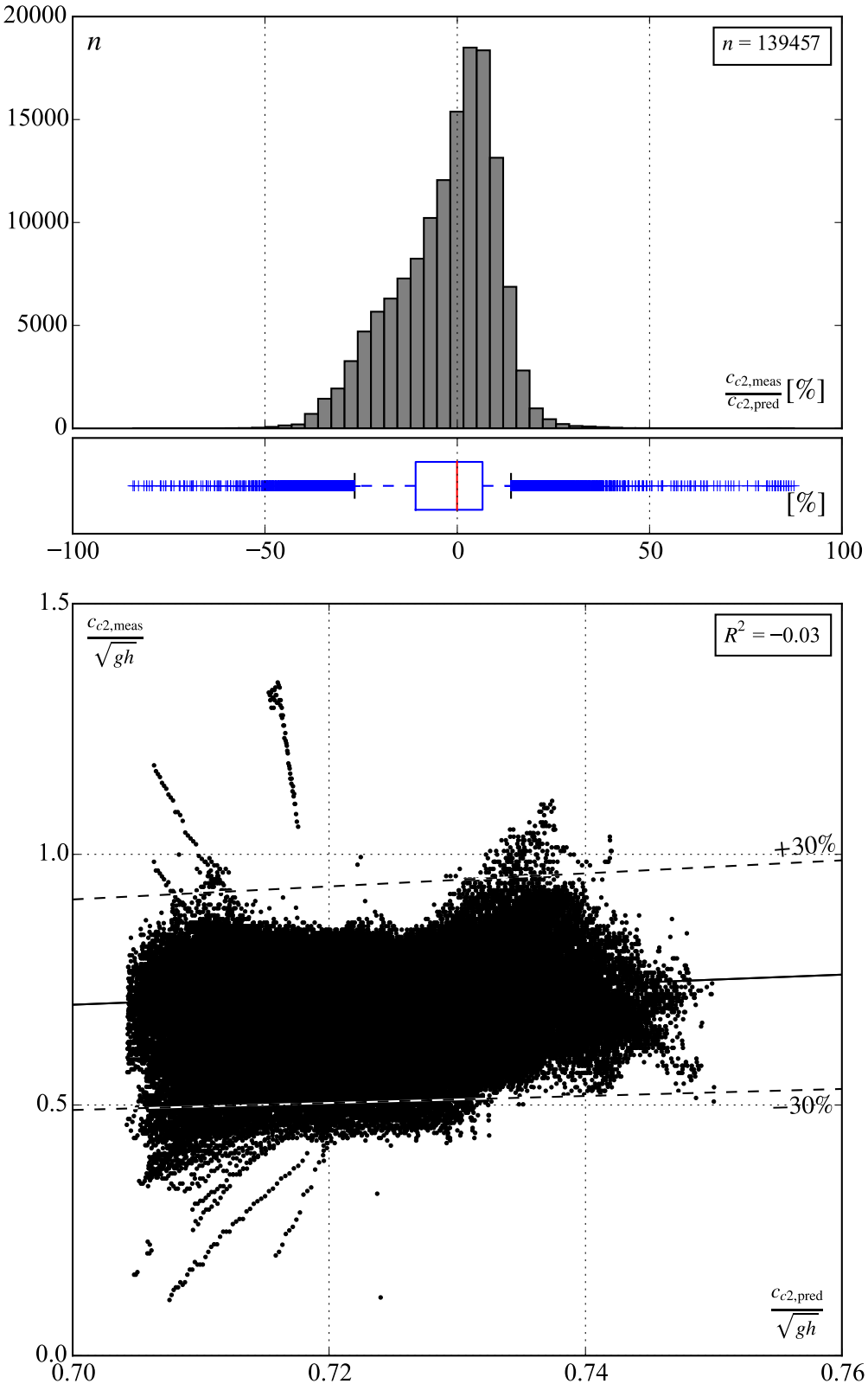

Fig. 4.45 Histogram, box plot with whiskers at 5$^{\mathrm{th}}$ and 95$^{\mathrm{th}}$ percentiles, and scatter plot of measured relative second wave crest celerity $c_{c2,\mathrm{meas}}/\sqrt{gh}$ versus predicted $c_{c2,\mathrm{pred}}/\sqrt{gh}$ based on Eq. (4.16)

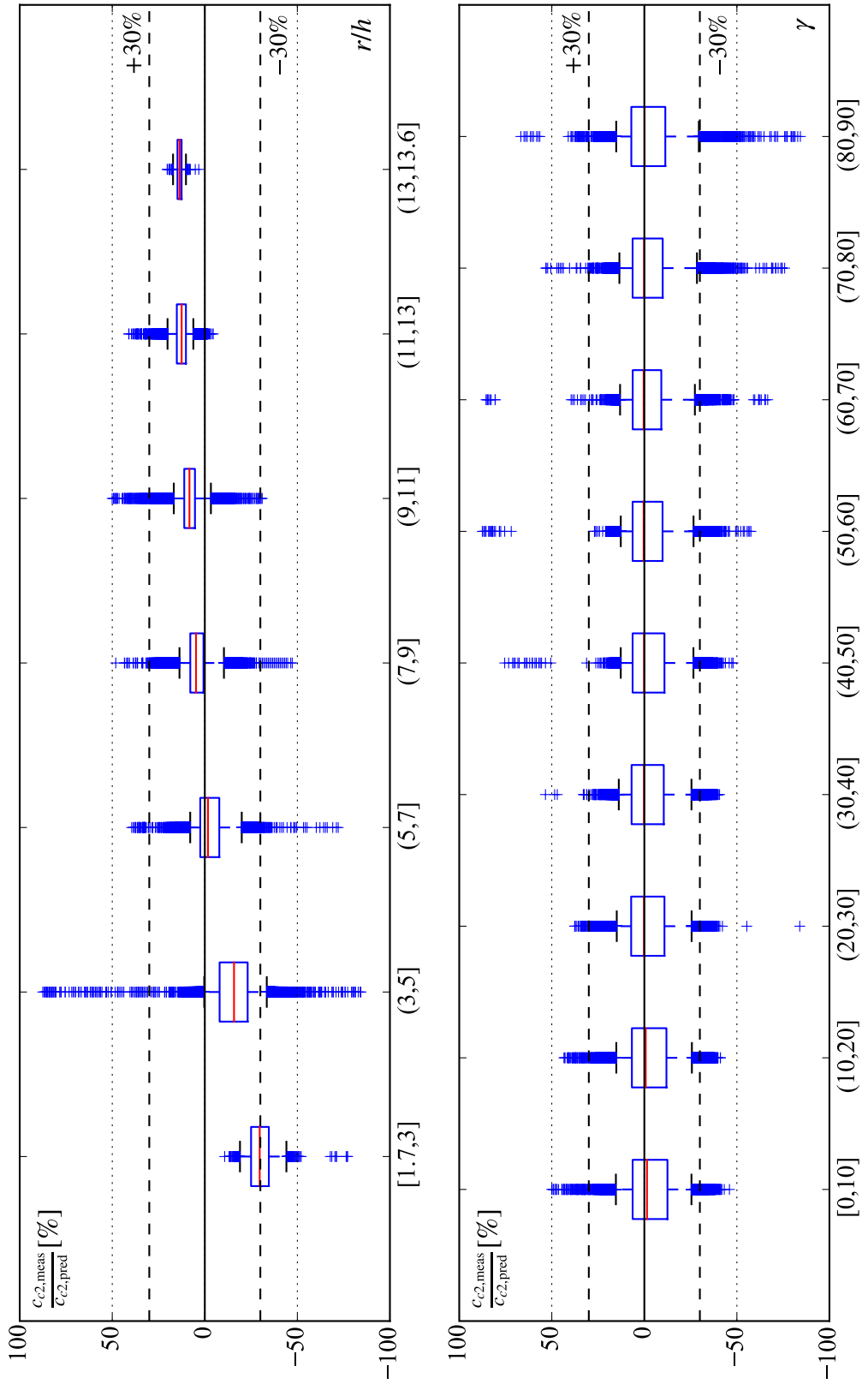

Fig. 4.46 Box plots with whiskers at 5$^{\mathrm{th}}$ and 95$^{\mathrm{th}}$ percentiles for measured relative second wave crest celerity $c_{c2,\mathrm{meas}}/\sqrt{gh}$ over predicted $c_{c2,\mathrm{pred}}/\sqrt{gh}$ versus relative propagation distance r/h and wave propagation angle γ based on Eq. (4.16)

4.4 Summary

Landslide generated impulse wave generation and propagation were experimentally investigated in a 2D wave channel and a 3D wave basin. The 42 2D tests provided the proof-of-concept, that mesh-packed slides generate wave features similar to free granular slides. The application of a videometric measurement system for tracking the wave propagation of 74 3D tests allowed for detailed insights into the spatial impulse wave propagation. In particular, the transition from the impact zone, which is affected by turbulence and air entrainment, to the wave propagation zone, where key wave characteristics become quantifiable, was studied and integrated into novel prediction equations. The impact radius r_0 represents the boundary between these two zones and its extent is governed by the slide parameters. The wave characteristics are governed by the impulse product parameter P, as a quantity for the 2D momentum transfer to the water column per unit slide width, the relative slide width B, and the slide impact angle α. Approximations were provided for the first wave crest amplitude, the first wave trough amplitude, the second wave crest amplitude, the first wave height, the first wave period, and the celerities of the first and the second wave crests. The evolution of the wave characteristics during propagation was presented separately for the wave propagation distance and the wave propagation angle. A more detailed discussion of the results is provided in the following chapter.

5 Discussion

5.1 Overview

The experimental results obtained in the previous chapter are discussed within this chapter. It highlights the main findings and states the limitations of the derived empirical equations, both based on experimental constraints as well as theoretical considerations. While the section on the 2D wave channel experiments is kept brief, a comparison between 2D and 3D wave propagation is provided in the section about the 3D wave basin experiments. The equations describing spatial wave propagation are discussed in detail and compared to existing 3D methods. The advantages and limitations related to the application of the videometric measurement system are summarized thereafter. The last part of this chapter covers the practical application of the derived spatial wave propagation equations for hazard assessment purposes. An example deschribes the computational procedure of a fictitious test case on a step-by-step basis. The equations of the present study are then applied to the 2007 impulse wave event at Chehalis Lake.

5.2 2D wave generation and propagation

The objective of the 2D experiments was to provide a proof-of-concept that mesh-packed slides generate wave characteristics similar to free granular slides. Despite the confirming results demonstrated in Chapter 4, the application of mesh-packed slides represents a significant modification of the slide properties. Lindstrøm (2016) found that the slide permeability has a significant effect on the wave generation process. At impact, the water infiltrates the porous sliding mass, so that the efficiency of the momentum transfer is reduced with increasing permeability. The granular material applied for the 2D and 3D experiments has a porosity of 45% (Heller 2008). With 47%, the mesh material has an only slightly higher porosity than the granular material. Besides the porosity, the permeability is also influenced by the pore diameter. While the granular pore diameter is estimated between 1 mm and 3 mm (Figure 3.5a), the mesh opening is 0.5 mm. However, since the flow length of the mesh material is small, this effect appears negligible. A direct comparison with equations derived from experiments with free granular slides is presented in Chapter 4. The major wave characteristics are well predicted by the equations based on the impulse product parameter P. Therefore, the velocity V_s of mesh-packed slides substitutes rather the centroid velocity of free granular slides than the faster front velocity. Note, that only granular material with a density substantially higher than that of water was used for both the 2D and the 3D experiments. The simplification involving mesh-packed slides may not be applicable for granular material of density lower than water, therefore.

5.3 3D wave generation and propagation

Table 5.1 recapitulates the relevant parameter ranges presented in Chapter 3. The range of the slide Froude number F covers both the sub- as well as the supercritical regimes. In addition to the relative bulk slide volume V and relative slide density D, the relative bulk slide mass $M = VD$ is also included. These parameters represent the general limitations for the equations proposed in Chapter 4. As for the 2D wave experiments, all governing parameters were varied except for D. Therefore, the effect of D on the wave generation process was not studied directly. Since D is indirectly included in the impulse product parameter P, representing the momentum transfer per slide width unit, its application range may be extended according to the 2D parameter range of P with $0.590 \leq D \leq 1.720$ (Heller 2008). However, note that this extended parameter range is not covered by the experiments in Chapter 4. The limitations of the wave propagation angle γ have to be assessed based on the wave basin geometry. While e.g. Mohammed and Fritz (2012) studied the edge wave propagation along a straight beach extending the sliding plane for $\gamma = 90°$, the wave propagation in this study was not bounded by a shoreline. Therefore, the 3D wave basin setup resembles rather the tip of a headland (Figure 3.7). Heller *et al.* (2012) conducted experiments with confining side walls and found no effect on the maximum wave features at $\gamma = 0°$, when the basin side angle θ is between 30° and 90° with $\theta = 0°$ representing the 2D wave channel. The maximum measured relative radial wave propagation distance r/h = 16.3 is shorter than the long wave criterion $L/h > 20$ (Dean and Dalrymple 1991), which is based on the wave length L. While this limitation is not sufficient for covering wave propagation over long distances in oceans, it is valid for smaller confined basins, e.g. fjords or lakes (see Section 5.6). The videometric measurement system yields a quasi-continuous representation of the free water surface, allowing for an adaptive localization of the initial wave features. The lower limit of the relative radial wave propagation distance r/h is thereby directly defined by the impact radius R_0 (Eq. 4.5). The measurement technique applied by Bregoli *et al.* (2017) allows for a similar approach. The composition of their prediction method also includes a slide parameter-dependent position of the maximum wave amplitude, which is directly integrated into an exponential amplitude decay function for $\gamma = 0°$. Eq. (2.13) by Heller *et al.* (2009) involves $r/h = 5$ as the lower limit. Therefore, R_0 allows for a prediction closer to the slide impact location for different propagation angles γ compared to already existing methods.

Table 5.1 Limitations of governing dimensionless parameters for spatial impulse waves

Symbol	Description	Test range
F	Slide Froude number	0.40 - 3.40
V	Relative bulk slide volume	0.187 - 0.750
D	Relative bulk slide density	1.338
M	Relative bulk slide mass	0.25 - 1.00
S	Relative slide thickness	0.15 - 0.60
P	Impulse product parameter	0.13 - 2.08
B	Relative slide width	0.83 - 5.00
α	Slide impact angle	30 - 90
r/h	Relative radial wave propagation distance	1.1 - 16.3
γ	Wave propagation angle	0 - 90

A direct comparison between existing equations to predict spatial wave propagation is provided in the comparative study in Section 4.3.3. These findings were incorporated into setting up the following equations for predicting the relative first wave crest amplitude A_{c1}, first wave trough amplitude A_{t1}, and the second wave crest amplitude A_{c2}:

$$A_{0,c1} = 0.2\mathsf{P}^{0.5} B^{0.75} \left(\cos\alpha_{\text{eff}}\right)^{0.25} \tag{Eq. 4.6}$$

$$A_{0,t1} = 0.35\mathsf{P}^{0.5} B^{0.5} \left(\cos\alpha_{\text{eff}}\right)^{0.5} \tag{Eq. 4.9}$$

$$A_{0,c2} = 0.14\mathsf{P}^{0.25} B^{0.25} \left(\cos\alpha_{\text{eff}}\right)^{0.25} \tag{Eq. 4.11}$$

$$A_{c1}\left(R^*,\gamma\right) = A_{0,c1} \exp\left(-0.4 A_{0,c1}^{-0.3}\sqrt{R^*}\right)\left[\operatorname{sech}\left(3.2\frac{\gamma}{90°}\right)\right]^{\cos\alpha_{\text{eff}}\exp\left(-0.15\sqrt{R^*}\right)} \tag{Eq. 4.8}$$

$$A_{t1}\left(R^*,\gamma\right) = A_{0,t1} \exp\left(-0.4 A_{0,t1}^{-0.3}\sqrt{R^*}\right)\left[\operatorname{sech}\left(3.6\frac{\gamma}{90°}\right)\right]^{\cos\alpha_{\text{eff}}\exp\left(-0.15\sqrt{R^*}\right)} \tag{Eq. 4.10}$$

$$A_{c2}\left(R^*,\gamma\right) = A_{0,c2} \exp\left(-0.1 A_{0,c2}^{-0.3}\sqrt{R^*}\right)\left[\operatorname{sech}\left(3\frac{\gamma}{90°}\right)\right]^{\cos\alpha_{\text{eff}}\exp\left(-0.15\sqrt{R^*}\right)}. \tag{Eq. 4.12}$$

Eqs. (4.6), (4.9), and (4.11) describe the initial wave amplitudes at the impact radius R_0 for $\gamma = 0°$. All three include the impulse product parameter P (Eq. 2.4) originally introduced by Heller (2008) and Heller and Hager (2010) based on 2D experiments. The

experimental results of this study indicate that P is also suitable to predict spatial impulse wave generation and propagation in 3D. Since P solely accounts for the momentum transfer from the slide to the water column per slide unit width, the relative slide width B is included as an additional governing parameter. Although the effective slide impact angle α_{eff} is already included in P, it has a stronger influence on the impulse wave generation in spatial environments, and is therefore included a second time as an additional parameter.

Eqs. (4.8), (4.10), and (4.12) include the initial wave amplitudes and describe the spatial wave propagation process with the relative surrogate wave propagation radius R^* and the wave propagation angle γ as polar coordinates. The equations are defined for $R^* \geq 0$, with $R^* = 0$ equivalent to the impact radius R_0. Note, that R_0 represents the boundary between the impact zone and the wave generation zones. For $r/h < R_0$ the splash screen created by the impacting slide reaches higher elevations. However, the splash screen is not regarded as a quantifiable wave featuring a crest (Figure 4.27). Exponential functions describe the wave amplitude decay processes. Hughes (1993) presents different wave attenuation equations featuring exponential functions and Bregoli *et al.* (2017) included this type of function for impulse wave propagation. Hyperbolic secant functions describing the vertical wave crest and trough shapes along γ are part of all three functions. Their exponents feature α_{eff} and R^* as governing parameters. The exponent accounts for the transformation of the wave crest and trough shapes along γ due to lateral spreading during propagation as presented in Section 4.3.2. A similar exponent was originally introduced by Heller and Spinneken (2015). If the amplitudes of a particular wave crest at different wave propagation angles γ are abstracted as communicating vessels, the hyperbolic secant shape of the total wave crest will be levelled out over time and the wave amplitude becomes independent of γ. In the context of wave propagation, the temporal factor may be replaced by the radial wave propagation distance r. Therefore, the wave amplitude will theoretically become independent of γ after the wave has propagated beyond a certain value of r. This effect is accounted for by the exponential function contained in the exponent of the hyperbolic secant functions in Eqs. (4.8), (4.10), and (4.12). For an increasing relative surrogate wave propagation distance R^*, the exponential function approaches 0 and the hyperbolic secant function yields 1 independent of γ. For a slide impact angle $\alpha = 30°$, the theoretical values of R^* needed to attain an amplitude of 90% at $\gamma = 90°$ compared to $\gamma = 0°$ are 418 for A_{c1}, 459 for A_{t1}, and 396 for A_{c2}. For $\alpha = 90°$, these limits are $R^* = 124$ for A_{c1}, 147 for A_{t1}, and 112 for A_{c2}. This depicts also the influence of the effective slide impact angle α_{eff} governing the initial shape of the wave crest (see Figure 4.31). However, all these values are well beyond the application limits of the equations with $r/h < 16.3$.

Besides an omnidirectional wave propagation pattern, spatial impulse waves are also characterized by an unconfined slide impact zone, where the slide impact energy is transferred to the water column. These conditions are met by the 3D wave basin setup. In contrast, the energy transfer and wave propagation in the 2D wave channel are unidirectional. While the wave characteristics in the 2D experiments are independent of the slide or channel

widths, respectively, as long as slide bulk mass m_s is scaled to keep the relative slide mass M constant, the slide width b has a major effect in the 3D environment as described in Section 4.3.2 as well as by Evers and Hager (2016a). Especially the relative initial first wave crest amplitude $A_{0,c1}$ (Eq. 4.6) is substantially influenced by the relative slide width B. Within the parameter range of the 3D wave basin experiments, $A_{0,c1}$ is strictly increasing with B for constant M. However, regarding the 2D experiments as the extreme case, there is theoretically an upper boundary to this increase. Similar considerations apply to the relative impact radius R_0. Table 5.2 compares computed values for A_{c1} (Eq. 4.8) with A_{2D} (Eq. 2.8, Heller 2008). The relative distance X_M (Eq. 2.6) of the 2D maximum wave amplitude A_M (Eq. 2.5) acts as the reference position. While X_M is not explicitly accounted for in A_{2D}, Heller *et al.* (2009) regard it as the point closest to the impact location, where Eq. (2.8) is valid. The impulse product parameter P and the slide impact angle α are kept constant in both the 2D and the 3D computations. Solely B was increased in the 3D computation to attain equal wave amplitudes $A_{c1} = A_{2D}$ at $r/h = X_M$ for $\gamma = 0°$. Note that m_s increases linearly with b to keep P and M constant. In both examples, the required relative slide width B is larger than the experimental test range between 0.83 and 5.00 (Table 3.2). In addition, the relative impact radii R_0 are smaller than X_M. The results of Table 5.2 are plotted in Figure 5.1. At a wave propagation distance $r/h = X = 15$, $A_{0,c1}$ has been subject to stronger decay than A_{2D}.

Table 5.2 Comparison between 2D (Heller and Hager 2010) and 3D cases for $A_{2D}(X_M) = A_{c1}(X_M - R_0, \gamma)$ at $\gamma = 0°$ with fixed slide parameters F = 2, $S = 0.25$, and $M = 1$

P	B	α	X_M	R_0	$A_{2D}(X_M) = A_{c1}(X_M - R_0, \gamma)$	$A_{2D}(15)$	$A_{c1}(15 - R_0, \gamma)$
0.95	5.3	30°	5.4	3.7	0.37	0.28	0.14
0.47	7.5	90°	3.8	2.4	0.23	0.16	0.07

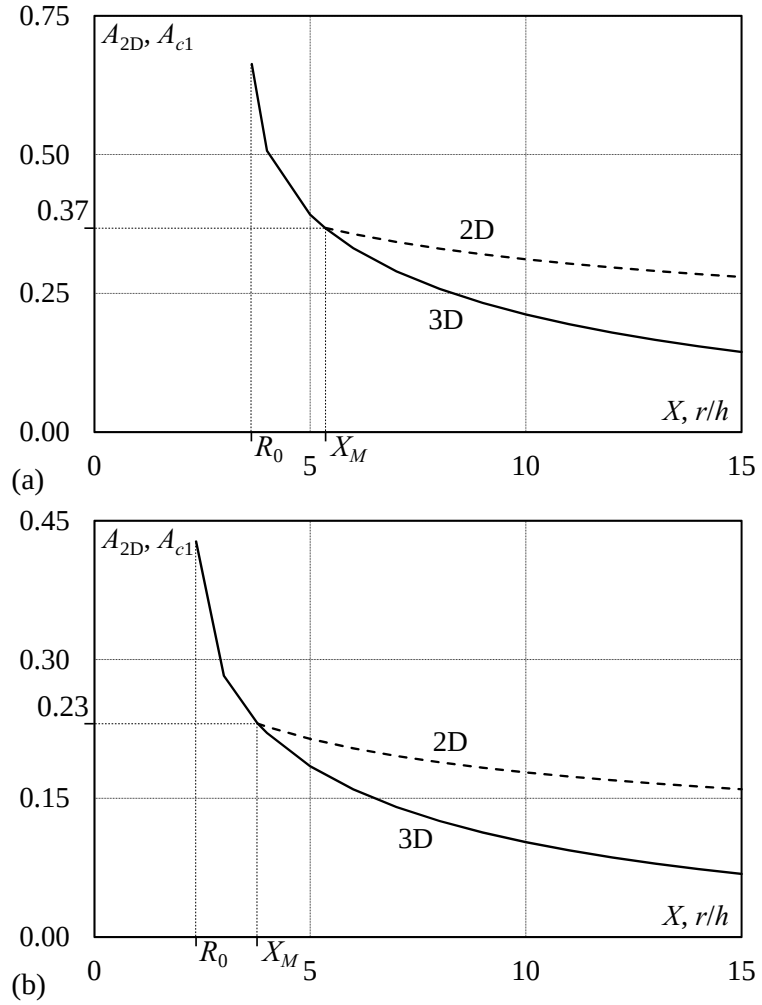

Fig. 5.1 Comparison between 2D (Eq. 2.8) and 3D (Eq. 4.8) wave decays at $\gamma = 0°$ for (a) $\mathsf{P} = 0.95$, $B = 5.3$, and $\alpha = 30°$, and (b) $\mathsf{P} = 0.47$, $B = 7.5$, and $\alpha = 90°$ (Table 5.2)

In the context of hazard assessment, the predicted wave characteristics act as input parameters to estimate the impact at the shoreline. One of the major impact characteristics is the runup height R, defined as the vertical distance between the still water surface and the highest elevation reached by the surging wave on the runup plane. Among the various water wave types (Heller 2008), the solitary wave causes the highest runup heights (Synolakis 1989). Impulse waves generated by subaerial landslides exhibit features of wave types within the range of intermediate-water to shallow-water waves depending on the generation process (Heller and Hager 2011). In Section 4.3.5.4, the celerities of the first and the second wave crests are presented in relation to the solitary wave celerity. The first wave crest propagates at approximately 95% of the solitary wave celerity, while the second propagates at 70%. This implies that the second wave crest propagates on average 26% slower than the first wave crest, a slightly higher reduction than 18% to 23% observed by Mohammed and Fritz (2012). Regarding hazard assessment, runup predictions based on solitary wave experiments seem to be appropriate for the first wave crest, whereas runup

heights caused by the second wave crest might be assessed too conservative.

5.4 Videometric water surface tracking

The application of the videometric measurement system yielded a quasi-continuous representation of the water surface allowing for the extraction of single water surface profiles. Therefore, this technique offered considerable advantages in adaptively tracking extreme wave features with variable locations in a spatial environment compared to point measurements. However, to automatically track a sufficient number of grid intersections, the water surface has to be smooth enough. The high turbulence within the slide impact zone caused too much distortion to the water surface and no grid intersections were detected right after the collapse of the splash screen (Figure 4.8). Furthermore, for an impact angle $\alpha = 90°$, camera 1 (Figure 3.7) was masked by the chute, which led to deficient tracking results within the impact zone and for wave propagation angles γ between 70° and 90° (Figure 4.16). Also strong spilling feature along the second wave crest and splashing drops caused occasional gaps within the water surface contours. Nonetheless, a temporal resolution of 24 Hz allowed for skipping single frames while still obtaining a sound data set for evaluation. The grid projection required an opaque white water surface, which was attained by adding TiO_2. In combination with deionized water, a suspension was created, which featured the required opacity. Although the wave basin was coated with PVC sheets, a reionization of the suspension over time could not be entirely prevented so that the opacity eventually decreased, finally leading to a poor projection quality. For the test setup described in Chapter 3, sufficient opacity was maintained over 3 months. A slight improvement of the opacity was attained after each increase of the still water depth due to the fresh deionized water. Environmental regulations as well as considerations do not allow the disposal of TiO_2 via the public sewage system; the suspension had to be collected by a certified waste management company. Depending on the size of the wave basin, the disposal may cause substantial cost. Also the availability of sufficient quantities of deionized water may limit the application of the videometric measurement system in larger wave basins.

5.5 Computational example

The practical application of the equations presented in Chapter 4 is demonstrated by means of a computational example. The scenario is adapted from Example 1 in Heller *et al.* (2009). The reservoir shown in Figure 5.2 is adjacent to an instable slope. A slope failure would result in a rock avalanche, which impacts the water surface with the slide characteristics listed in Table 5.3. The reservoir is impounded by a dam structure at a distance of 280 m from the slide impact location. The center of the dam crest is located at an angle of $-59°$ relative to the slide impact direction. The still water depth in this part of the reservoir is quasi-constant at 30 m. The wave magnitude at the dam site will be assessed below.

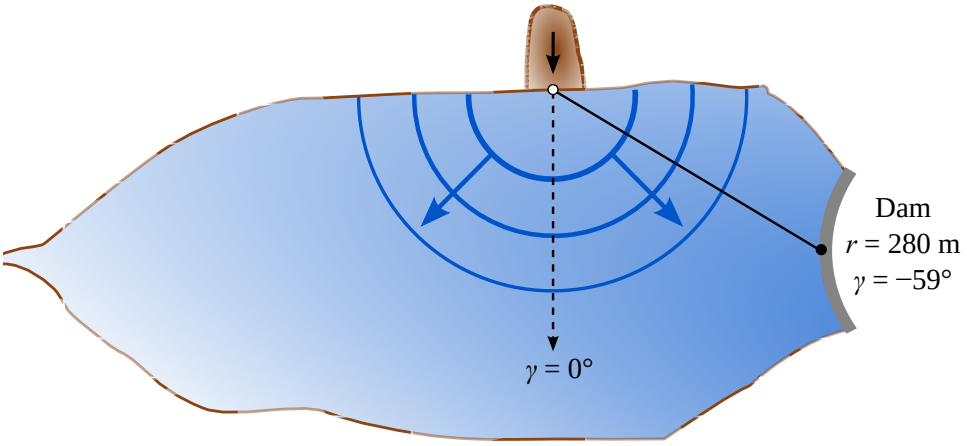

Fig. 5.2 Position plan of the reservoir (adapted from Heller *et al.* 2009)

Table 5.3 Governing parameters for computational example

Symbol	Unit	Description	Value
V_s	[m/s]	Slide impact velocity	37
$\forall_s$	[m^3]	Bulk slide volume	22,000
ρ_s	[kg/m^3]	Bulk slide density	1,700
s	[m]	Slide thickness	12
b	[m]	Slide width	45
α	[°]	Slide impact angle	40
h	[m]	Still water depth	30
r	[m]	Radial wave propagation distance	280
γ	[°]	Wave propagation angle	−59°

The following computations are rounded at each step for an easier understanding. In addition, units are only specified for the results. The impulse product parameter

$$\mathsf{P} = \mathsf{F} S^{0.5} M^{0.25} \left\{\cos\left([6/7]\,\alpha\right)\right\}^{0.5} = \left(\frac{V_s}{\sqrt{gh}}\right)\left(\frac{s}{h}\right)^{0.5}\left(\frac{m_s}{\rho_w b h^2}\right)^{0.25}\left(\cos\alpha_{\text{eff}}\right)^{0.5} \tag{Eq. 2.4}$$

results with $m_s = \forall_s \rho_s$, $\rho_w = 1{,}000$ kg/m^3, $g = 9.81$ m/s^2, and $\cos\alpha_{\text{eff}} = \cos[6/7]\alpha \approx 0.83$ in

$$\mathsf{P} = \left(\frac{37}{\sqrt{9.81 \cdot 30}}\right)\left(\frac{12}{30}\right)^{0.5}\left(\frac{22{,}000 \cdot 1{,}700}{1000 \cdot 45 \cdot 30^2}\right)^{0.25}(0.83)^{0.5} \approx 1.22.$$

The governing dimensionless quantities include the slide Froude number $\mathsf{F} \approx 2.16$, the relative slide thickness $S = 0.4$, and the relative slide mass $M \approx 0.92$. By introducing the relative slide width $B = b/h = 45/30 = 1.5$, the impact radii R_0 and r_0 are computed for a wave propagation angle $\gamma = -59°$ as

$$R_{0,0^\circ} = 2.5\left(\mathrm{P}B\cos\alpha_{\text{eff}}\right)^{0.25} = 2.5\left(1.22\cdot 1.5\cdot 0.83\right)^{0.25} \approx 2.78 \qquad \text{(Eq. 4.3)}$$

$$R_{0,90^\circ} = \left(\frac{B}{2}\right) + 1.5\left(\mathrm{P}\cos\alpha_{\text{eff}}\right)^{0.25} = \left(\frac{1.5}{2}\right) + 1.5\left(1.22\cdot 0.83\right)^{0.25} \approx 2.25 \qquad \text{(Eq. 4.4)}$$

$$R_0(\gamma) = \sqrt{\frac{R_{0,0^\circ}^2 R_{0,90^\circ}^2}{R_{0,0^\circ}^2\sin^2\gamma + R_{0,90^\circ}^2\cos^2\gamma}} \qquad \text{(Eq. 4.5)}$$

$$R_0(-59^\circ) = \sqrt{\frac{2.78^2\cdot 2.25^2}{2.78^2\sin^2(-59^\circ) + 2.25^2\cos^2(-59^\circ)}} \approx 2.36$$

$$r_0 = R_0 h = 2.36\cdot 30 \approx 71\,\text{m}.$$

Consequently, the relative surrogate wave propagation radius is

$$R^* = \frac{r}{h} - R_0 = \frac{280}{30} - 2.36 \approx 7.$$

The initial first wave crest amplitude at $\gamma = 0^\circ$ is

$$A_{0,c1} = 0.2\mathrm{P}^{0.5}B^{0.75}\left(\cos\alpha_{\text{eff}}\right)^{0.25} = 0.2\cdot 1.22^{0.5}\cdot 1.5^{0.75}\cdot 0.83^{0.25} \approx 0.29 \qquad \text{(Eq. 4.6)}$$

$$a_{0,c1} = A_{0,c1} h = 0.29\cdot 30 = 8.7\,\text{m}.$$

The first wave crest amplitude at the dam for $\gamma = -59^\circ$ is

$$A_{c1}(R^*,\gamma) = A_{0,c1}\exp\left(-0.4A_{0,c1}^{-0.3}\sqrt{R^*}\right)\left[\operatorname{sech}\left(3.2\frac{\gamma}{90^\circ}\right)\right]^{\cos\alpha_{\text{eff}}\exp\left(-0.15\sqrt{R^*}\right)} \qquad \text{(Eq. 4.8)}$$

$$A_{c1} = 0.29\exp\left(-0.4\left(0.29\right)^{-0.3}\sqrt{7}\right)\left[\operatorname{sech}\left(3.2\frac{-59^\circ}{90^\circ}\right)\right]^{0.83\exp\left(-0.15\sqrt{7}\right)} \approx 0.04$$

$$a_{c1} = A_{c1} h = 0.04\cdot 30 = 1.2\,\text{m}.$$

The initial first wave trough amplitude at $\gamma = 0°$ is

$$A_{0,t1} = 0.35\left(\mathrm{P}B\cos\alpha_{\text{eff}}\right)^{0.5} = 0.35\left(1.22\cdot 1.5\cdot 0.83\right)^{0.5} \approx 0.43 \qquad \text{(Eq. 4.9)}$$

$$a_{0,t1} = A_{0,t1}h = 0.43\cdot 30 = 12.9\,\text{m}.$$

The first wave trough amplitude at the dam for $\gamma = -59°$ is

$$A_{t1}\left(R^*,\gamma\right) = A_{0,t1}\exp\left(-0.4A_{0,t1}^{-0.3}\sqrt{R^*}\right)\left[\operatorname{sech}\left(3.6\frac{\gamma}{90°}\right)\right]^{\cos\alpha_{\text{eff}}\exp\left(-0.15\sqrt{R^*}\right)} \qquad \text{(Eq. 4.10)}$$

$$A_{t1} = 0.43\exp\left(-0.4\left(0.43\right)^{-0.3}\sqrt{7}\right)\left[\operatorname{sech}\left(3.6\frac{-59°}{90°}\right)\right]^{0.83\exp\left(-0.15\sqrt{7}\right)} \approx 0.07$$

$$a_{t1} = A_{t1}h = 0.07\cdot 30 = 2.1\,\text{m}.$$

Therefore, the first wave height at the dam is

$$Y_1 = A_{c1} + A_{t1} = 0.07 + 0.04 = 0.11 \qquad \text{(Eq. 4.13)}$$

$$H_1 = Y_1 h = 0.11\cdot 30 = 3.3\,\text{m}.$$

The first wave period at the dam is

$$T_1\left(R^*,\gamma\right)\left(g/h\right)^{0.5} = 10\left(Y_1\right)^{0.2} + \frac{R^*}{2} = 10\left(0.11\right)^{0.2} + \frac{7}{2} \approx 9.9 \qquad \text{(Eq. 4.14)}$$

$$T_1 = T_1\left(g/h\right)^{0.5}\left(h/g\right)^{0.5} = 9.9\left(30/9.81\right)^{0.5} \approx 17\,\text{s}.$$

The first wave crest celerity at the dam is

$$\frac{c_{c1}}{\sqrt{gh}} = 0.95\sqrt{1+A_{c1}} = 0.95\sqrt{1+0.04} \approx 0.97 \qquad \text{(Eq. 4.15)}$$

$$c_{c1} = \frac{c_{c1}}{\sqrt{gh}}\sqrt{gh} = 0.97\sqrt{9.81\cdot 30} \approx 17\,\text{m/s}.$$

The initial second wave crest amplitude at $\gamma = 0°$ is

$$A_{0,c2} = 0.14\,(\mathsf{P}B\cos\alpha_{\text{eff}})^{0.25} = 0.14\,(1.22\cdot 1.5\cdot 0.83)^{0.25} \approx 0.16 \qquad \text{(Eq. 4.11)}$$

$$a_{0,c2} = A_{0,c2}h = 0.16\cdot 30 = 4.8\,\text{m}.$$

The second wave crest amplitude at the dam for $\gamma = -59°$ is

$$A_{c2}\,(R^*,\gamma) = A_{0,c2}\exp\left(-0.1A_{0,c2}^{-0.3}\sqrt{R^*}\right)\left[\text{sech}\left(3\frac{\gamma}{90°}\right)\right]^{\cos\alpha_{\text{eff}}\exp\left(-0.15\sqrt{R^*}\right)} \qquad \text{(Eq. 4.12)}$$

$$A_{c2} = 0.16\exp\left(-0.1\,(0.16)^{-0.3}\sqrt{7}\right)\left[\text{sech}\left(3\frac{-59°}{90°}\right)\right]^{0.83\exp\left(-0.15\sqrt{7}\right)} \approx 0.07$$

$$a_{c2} = A_{c2}h = 0.07\cdot 30 = 2.1\,\text{m}.$$

The second wave crest celerity at the dam is

$$\frac{c_{c2}}{\sqrt{gh}} = 0.7\sqrt{1+A_{c2}} = 0.7\sqrt{1+0.07} \approx 0.72 \qquad \text{(Eq. 4.16)}$$

$$c_{c2} = \frac{c_{c2}}{\sqrt{gh}}\sqrt{gh} = 0.72\sqrt{9.81\cdot 30} \approx 12\,\text{m/s}.$$

The computational example yields key wave characteristics, which act as input parameters for a subsequent assessment of the wave runup (e.g. Su and Mirie 1980, Synolakis 1987, Müller 1995, Fuchs and Hager 2015, Pujara *et al.* 2015, and Hafsteinsson *et al.* 2017), hydrodynamic forces (e.g. Ramsden 1996 and Pujara *et al.* 2015), or overtopping volumes (e.g. Müller 1995, Kobel *et al.* 2017, and Huber *et al.* 2017) at dam structures. Except for the increased relative bulk slide density $D = \rho_s/\rho_w = 1.7$, all derived dimensionless quantities are in the range of Table 3.2. However, D is in the parameter range of the impulse product parameter P and its corresponding 2D experiments (Heller 2008 and Heller and Hager 2010). The rounding errors introduced after each step of the computational example, are less than 5% with regard to the wave amplitudes at the dam.

5.6 Case study: Chehalis Lake

On 4 December 2007, a debris avalanche detached at the northwestern shore of Chehalis Lake, BC, Canada, and generated impulse waves, which caused extensive damage to

the shoreline as well as the lower Chehalis River (Roberts *et al.* 2013). The lake has an elongated form with a length of approximately 7.5 km and a width between 500 m and 1,000 m. The debris avalanche occurred in the lake section north of the Skwellepil Creek inlet (Figure 5.3). This part of the lake was subject to runup heights up to almost 40 m (Roberts *et al.* 2013). As is typical for impulse wave events at this scale, no information on wave magnitudes within the lake surface area is available. Only runup heights along the shoreline may be measured in the aftermath of the event. The purpose of this case study is to validate the equations of Chapter 4, based on an event at prototype scale. Therefore, two runup height equations by Synolakis (1987) and Fuchs and Hager (2015) are applied, which include the computed wave crest amplitudes as input parameters.

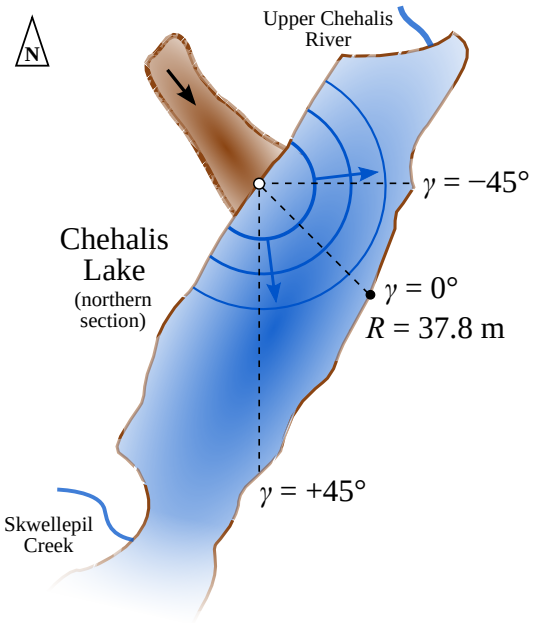

Fig. 5.3 Position plan of northern section of Chehalis Lake (not to scale)

The governing parameters as well as their dimensionless quantities are listed in Table 5.4. Except for the relative bulk slide volume V and the relative bulk slide density D , all dimensionless quantities are in the range of Table 3.2. As for the computational example, V and D are covered by the range of the impulse product parameter (Heller 2008 and Heller and Hager 2010). Run up height data and their corresponding wave propagation distances and angles are extracted from Roberts *et al.* (2013). Only runup locations in the northern section of Chehalis Lake are considered. Furthermore, runup locations subject to edge waves along the sliding plane and within the Upper Chehalis River inlet are ecluded. The wave propagation angle $\gamma = 0°$ is defined in direction to the point where the maximum runup height $R = 37.8$ m was measured. Referenced to true north, $\gamma = 0°$, which has the same orientation as the slide propagation angle at impact, was estimated to 135°.

Table 5.4 Governing parameters for Chehalis Lake case study

Symbol	Unit	Description	Value	Data origin
V_s	[m/s]	Slide impact velocity	60	Wang *et al.* (2015)
~~V_s~~	[m^3]	Bulk slide volume	3,000,000	Roberts *et al.* (2013)
ρ_s	[kg/m^3]	Bulk slide density	1,650	Bregoli *et al.* (2017)
s	[m]	Slide thickness	40	Wang *et al.* (2015)
b	[m]	Slide width	210	Roberts *et al.* (2013)
α	[°]	Slide impact angle	30	Bregoli *et al.* (2017)
h	[m]	Still water depth	120	Wang *et al.* (2015)
r	[m]	Radial wave propagation distances	750 - 1500	Roberts *et al.* (2013)
γ	[°]	Wave propagation angles	$-78°$ - 73°	Roberts *et al.* (2013)
β	[°]	Wave runup angle	30°	-
F	[-]	Slide Froude number	1.75	-
V	[-]	Relative bulk slide volume	0.99	-
D	[-]	Relative bulk slide density	1.65	-
S	[-]	Relative slide thickness	0.33	-
P	[-]	Impulse product parameter	1.08	-
B	[-]	Relative slide width	1.75	-
r/h	[-]	Rel. radial wave prop. distances	6.25 - 12.5	-

The runup heights R are computed with Eq. (5.1) by Synolakis (1987) as well as Eq. (5.2) by Fuchs and Hager (2015). Both equations are based upon experimental data of solitary wave runup on an impermeable beach of constant inclination. The governing parameters are the runup angle β, the relative wave crest amplitude $\varepsilon = a/h$, and the still water depth h:

$$R = 2.831\,(\cot\beta)^{0.5}\,\varepsilon^{1.25}h \tag{5.1}$$

$$R = 3\,(\tan\beta)^{-0.05}\,\varepsilon h. \tag{5.2}$$

The wave runup angle β is roughly approximated with 30° for all runup locations based on the surrounding topography of Chehalis Lake. The relative wave crest amplitudes $\varepsilon = a_{c1}/h$ and $\varepsilon = a_{c2}/h$ are computed with Eqs. (4.8) and (4.12). In Heller *et al.* (2009), the radial wave propagation distance r for the computation of the wave amplitudes relevant for runup is located at the submerged base point at the bottom of the runup plane. For a still water depth $h = 120$ m and a runup angle β, the base point lies at a horizontal distance of 208 m to the shore. Within short propagation distances and for small runup angles, this distance accounts for a substantial portion of the overall wave propagation distance. Since wave amplitudes are larger at the base point than at the shore when shoaling is neglected, this approach may be regarded as conservative. However, the wave amplitude decay process continues after a wave crest has passed the base point. To take this effect

into account, the wave crest amplitudes a_{c1} and a_{c2} were computed both for the base point and for the shore.

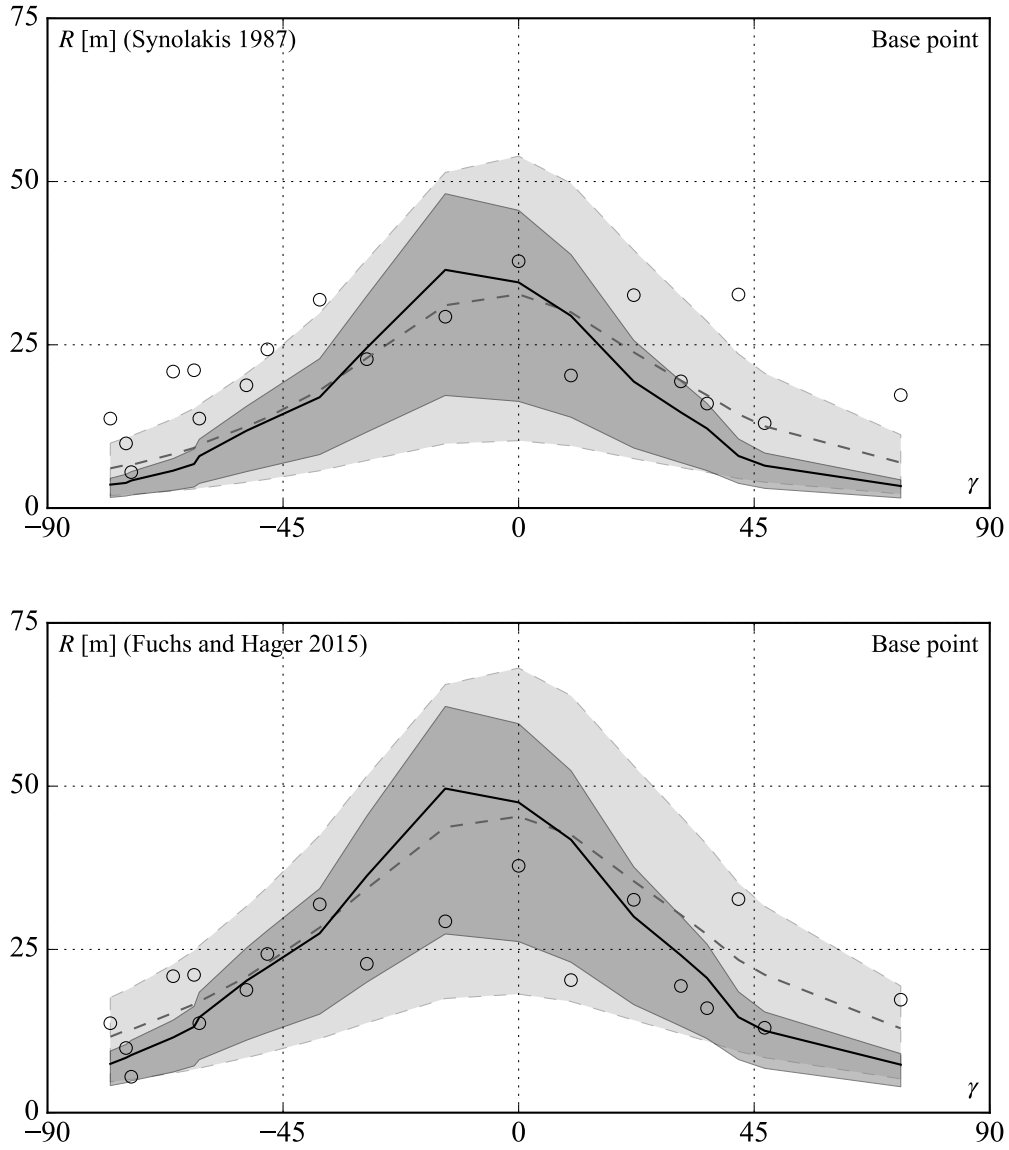

Fig. 5.4 Runup heights R at Chehalis Lake computed with Eqs. 5.1 and 5.2 for a_{c1} (—) with −45% and +25% band and a_{c2} (− −) with −60% and +50% band at base point, measured (○) by Roberts *et al.* (2013) over wave propagation angle γ

Figure 5.4 shows the computed runup heights for the wave amplitudes at the base point. The bandwidths refer to the ranges of the wave crest amplitudes a_{c1} (Eq. 4.8) and a_{c2} (Eq. 4.12) including 90% of the data points (see Section 4.3.5). Note that the scatter ranges are directly accounted for in the wave amplitudes before the runup heights are computed. For wave propagation angles γ within $\pm 30°$, Eq. (5.1) predicts the measured runup heights well. Beyond this range, R tends to be underestimated. Inverse observations apply for Eq.

(5.2). As expected, all computed runup heights in Figure 5.5 are lower than in Figure 5.4. Eq. (5.1) tends to underestimate the measurements at almost all runup locations. As to Eq. (5.2), all runup measurements scatter within the bandwidths related to a_{c1} and a_{c2} with a tendency to be more conservative around $\gamma = 0°$.

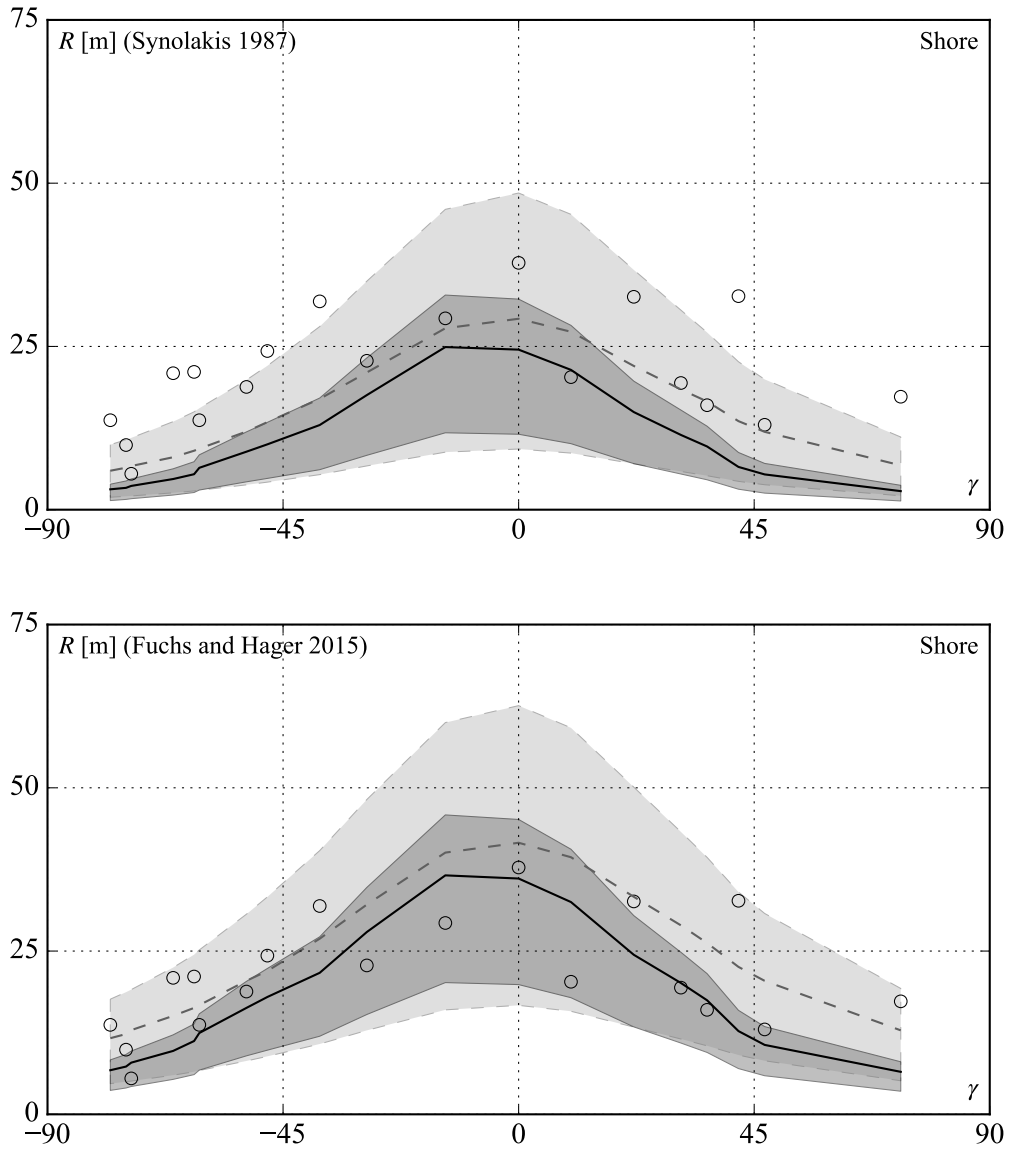

Fig. 5.5 Runup heights R at Chehalis Lake computed with Eqs. 5.1 and 5.2 for a_{c1} (—) with −45% and +25% bands and a_{c2} (− −) with −60% and +50% bands at shore, measured (○) by Roberts *et al.* (2013) over wave propagation angle γ

The combination of the shore as the reference location for the determination of the wave amplitudes and the runup equation by Fuchs and Hager (2015) yields the most favorable predictions, which are as close to the actual measurements as possible. Note that the

measurements themselves are subject to large scatter. The maximum computed wave amplitudes for $\gamma = 0°$ at an impact radius $r_0 = 343$ m are $a_{c1} = 37.0$ m and $a_{c2} = 19.2$ m.

5.7 Summary

The results from Chapter 4 are discussed and the presented equations applied to a prototype-scaled impulse wave event at Chehalis Lake. The impulse product parameter P, originally derived from 2D experiments with granular material, was found to adequately quantify both 2D and 3D impulse wave experiments with mesh-packed slides. The limitations of the wave basin experiments were specified both based on the experimental parameter ranges as well as a comparison with 2D wave propagation as the extreme case. The advantages and technical limitations regarding the application of the videometric measurement system were also discussed, highlighting its capabilities especially for tracking wave processes close to the impact zone. A computational example demonstrates the applicability of the derived equations to a fictitious prototype case. The final section validates, that the equations are capable of predicting wave heights at the correct order of magnitude, by back calculation of the 2007 Chehalis Lake event.

6 Conclusions

6.1 Summary

6.1.1 General

- Spatial impulse waves generated by subaerial landslides were investigated in a 3D wave basin with a length of 8 m and a width of 4.5 m (Section 3.4).
- Mesh-packed slides were applied in 74 experiments under the systematic variation of the slide impact velocity V_s, the slide thickness s, the slide width b, the slide mass m_s, the slide impact angle α, and the still water depth h (Sections 3.2.2 and 3.3).
- The application of a videometric measurement system yielded a quasi-continuous representation of the water surface with up to 6,000 measurements points at an acquisition rate of 24 Hz (Section 3.4.2.2).
- The first wave crest amplitude a_{c1}, the first wave trough amplitude a_{t1}, the first wave height H_1, the first wave crest celerity c_{c1}, and the first wave period T_1, as well as the second wave crest amplitude a_{c2} and the second wave crest celerityc_{c2} of the generated wave train were derived from the water surface contours and empirically described with novel approximations in a polar coordinate system (Sections 3.4.3 and 4.3).
- The impact radius r_0 was introduced as the boundary between the slide impact zone and the wave propagation zone (Section 4.3.4.1).
- The equations describing the spatial impulse wave propagation combine both the maximum wave amplitudes as well as their decay in an integrated expression (Sections 4.3.4 and 4.3.5).

6.1.2 Governing parameters

- The 2D impulse product parameter P including the slide Froude number F, the relative slide thickness S, the relative slide mass M, and the slide impact angle α was found to be a relevant parameter also in the 3D setup (Sections 4.3.4 and 4.3.5).
- In addition to P describing the 2D momentum transfer from the slide to the water column per slide unit width, the relative slide thickness B and again the slide impact angle α were identified as major governing parameters for quantifying 3D wave propagation (Sections 4.3.4 and 4.3.5).
- An increase of B creates larger initial wave amplitudes even if the slide mass m_s is kept constant and M decreases consequently (Sections 2.3.2, 4.3.4, and 4.3.5).
- Both the initial wave amplitudes as well as the shape of the initial wave crests and trough are influenced by α: an increase of α in 3D leads to a stronger decrease of the initial wave crests and trough than in 2D for the wave propagation angle $\gamma = 0°$, while their shapes become flatter, i.e. the ratio between the amplitudes for $\gamma = 0°$

and 90° increases (Sections 4.3.2, 4.3.4, and 4.3.5).
- The governing parameters confirm the application of the Froude similitude also for spatial impulse wave generation and propagation (Section 3.2.1).

6.1.3 Slide impact zone

- The impact radius r_0 delimits the slide impact zone featuring strong turbulence due to the impact crater collapse from the wave propagation zone where wave amplitudes and further characteristics become quantifiable (Section 4.3.4.1).
- The extent of r_0 is described by an elliptic function for γ between 0° and 90° based on the governing parameters P, B, and α (Section 4.3.4.1).
- The initial wave amplitudes of the first wave crest $a_{0,c1}$, the first wave trough $a_{0,t1}$, and the second wave crest $a_{0,c2}$ share r_0 as their common radial coordinate (Sections 4.3.4 and 4.3.5).
- The shape of the initial wave crests and troughs are described with a hyperbolic secant function for wave propagation angles γ between 0° and 90° (Sections 4.3.4.2 and 4.3.5).

6.1.4 Wave propagation zone

- Beyond the impact radius r_0, the spatial wave propagation is described by the surrogate propagation radius $r^* = r - r_0$ serving as radial coordinate (Section 4.3.4.1).
- An exponential function applied to the initial wave amplitudes describes the wave amplitude decay for $\gamma = 0°$ along r^* with its decay rate governed by the initial amplitude (Section 4.3.5).
- Lateral spreading of the wave crests and the wave troughs during propagation is accounted for in the hyperbolic secant function with an exponent including the impact angle α and r^* as governing parameters (Sections 4.3.2 and 4.3.5)
- Based on $a_{0,c1}$, $a_{0,t1}$, and $a_{0,c2}$, the first wave height H_1, the first wave period T_1, and the first and second wave crest celerities c_{c1} and c_{c2} are described (Section 4.3.5).
- While c_{c1} accounts for approximately 95% of the solitary wave celerity, c_{c2} accounts only for about 70%, leading to a constant increase of T_1 during wave propagation (Section 4.3.5).
- Edge waves were not accounted for, i.e. only features of undisturbed outgoing waves were investigated and no continuous shoreline extending the sliding plane was represented in the experimental setup (Section 3.4).

6.1.5 Mesh-packed slides

- Mesh-packed slides were applied in a 2D wave channel as an alternative wave generation method allowing for deformation after impact onto the water surface similar to free granular slides, while offering the advantages of rigid slide bodies regarding experimental handling (Section 3.3.1).

- The measured magnitudes and experimental scatter ranges for the maximum wave amplitude a_M and height H_M as well as the wave amplitudes a_{2D}, the wave heights H_{2D}, and the mean wave celerity c_{am} correspond to those of the experiments with free granular slides by Heller (2008) (Section 4.2).
- While free granular slides are subject to higher velocities at their front than at their centroid before impact, these velocities are equal for mesh-packed slides (Section 2.3.1).

6.1.6 Videometric measurement system

- The application of a videometric measurement system yields a quasi-continuous representation of the water surface allowing for unprecedented insights into spatial impulse wave propagation patterns (Section 4.3.2).
- The videometric measurement approach allows for adaptively tracking the location of the impact radius r_0 (Section 4.3.4.1).

6.1.7 Benchmarking

- For the prediction of measured wave characteristics, a comparative study identified the limitations of existing equations regarding their experimental setup, the slide model, or a fixed parameter set (Section 4.3.3).
- The novel equations were applied to the prototype-scaled event at Chehalis Lake in 2007; the magnitude of the measured prototype runup heights were predicted with a good overall agreement (Section 5.6).

6.1.8 Parameter limitations

General:

- The dimensionless parameters of the experiments are within the order of magnitude of prototype impulse wave events (Sections 2.3.4, 4.2.1, and 4.3.1).
- Compared to the 2D experiments evaluated by Heller (2008) with $0.17 \leq \mathsf{P} \leq 8.13$, the present values of the impulse product parameter $0.13 \leq \mathsf{P} \leq 2.08$ cover the lower range corresponding to selected prototype dimensions $0.03 \leq \mathsf{P} \leq 3.37$ (Section 2.3.4).

The dimensionless parameter limitations are as follows:

- Slide Froude number: $0.40 \leq \mathsf{F} \leq 3.40$
- Relative bulk slide volume: $0.187 \leq V \leq 0.750$
- Relative bulk slide density: $D = 1.338$
- Relative bulk slide mass: $0.25 \leq M \leq 1.00$
- Relative slide thickness: $0.15 \leq S \leq 0.60$
- Impulse product parameter: $0.13 \leq \mathsf{P} \leq 2.08$
- Relative slide width: $0.83 \leq B \leq 5.00$

- Slide impact angle: $30° \leq \alpha \leq 90°$
- Relative radial wave propagation distance: $1.1 \leq r/h \leq 16.3$
- Wave propagation angle: $0° \leq \gamma \leq 90°$

The experimental parameter limitations follow:

- Slide impact velocity: $0.72\ \mathrm{m/s} \leq V_s \leq 4.76\ \mathrm{m/s}$
- Bulk slide volume: $0.0075\ \mathrm{m}^3 \leq V_s \leq 0.0299\ \mathrm{m}^3$
- Bulk slide density: $\rho_s = 1{,}338\ \mathrm{kg/m}^3$
- Bulk slide mass: $10\ \mathrm{kg} \leq m_s \leq 40\ \mathrm{kg}$
- Slide thickness: $0.06\ \mathrm{m} \leq s \leq 0.12\ \mathrm{m}$
- Slide width: $0.25\ \mathrm{m} \leq b \leq 1.00\ \mathrm{m}$
- Slide impact angle: $30° \leq \alpha \leq 90°$
- Still water depth: $0.2\ \mathrm{m} \leq h \leq 0.4\ \mathrm{m}$
- Water density: $\rho_w = 1{,}000\ \mathrm{kg/m}^3$
- Radial wave propagation distance: $0.45\ \mathrm{m} \leq r \leq 3.26\ \mathrm{m}$
- Wave propagation angle: $0° \leq \gamma \leq 90°$

6.2 Outlook

- The experiments conducted in this research are limited to a single bulk slide density ρ_s; although the impulse product parameter P includes in 2D also slides with densities lighter than water, the experimental validation of the density effect of P is pending for 3D.
- Impulse waves generated by subaerial slides were the exclusive focus of this study. However, also partly submerged or submarine landslides may generate tsunami-like waves making further investigations on different failure modes necessary.
- The outgoing impulse wave train was not subject to any shoreline boundaries. By installing and systematically varying common shoreline layouts in the wave basin, prediction equations may be derived for the prediction of wave characteristics in extremely confined water bodies.
- The videometric measurement approach is applicable to various research topics in hydraulic experimentation, where the 3D deformation of the water surface is of particular interest; e.g. the initial dipole deformation of the still water surface caused by submarine landslides or the water surface during spatial dike breaching as demonstrated by Frank (2016).
- Data sets with a high spatial resolution of the 3D impulse wave generation and propagation process were produced from 74 experiments allowing for the validation of numerical models against a broad range of slide parameters especially in the near field of the slide impact zone (Evers 2018).

Bibliography

Abelson, H. I. (1970). Pressure measurements in the water-entry cavity. *Journal of Fluid Mechanics*, 44(01): 129. http://dx.doi.org/10.1017/s0022112070001738.

Achterberg, D.; Gotzmer, J. W.; Spath, R.; Tseng, M.; Woodward, D. E.; Miller, N.; Shipman, S. A. (1998). Federal guidelines for dam safety: selecting and accommodating inflow design floods for dams. Dept. of Homeland Security, Federal Emergency Management Agency, Washington D.C..

Ataie-Ashtiani, B.; Nik-Khah, A. (2008). Impulsive waves caused by subaerial landslides. *Environmental Fluid Mechanics*, 8(3): 263–280. http://dx.doi.org/10.1007/s10652-008-9074-7.

Blown, I.; Church, M. (1985). Catastrophic lake drainage within the Homathko River basin, British Columbia. *Canadian Geotechnical Journal*, 22(4): 551–563. http://dx.doi.org/10.1139/t85-075.

Bornhold, B. D.; Harper, J. R.; McLaren, D.; Thomson, R. E. (2007). Destruction of the first nations village of Kwalate by a rock avalanche-generated tsunami. *Atmosphere-Ocean*, 45(2): 123–128. 0705-5900. http://dx.doi.org/10.3137/ao.450205.

Bregoli, F.; Bateman, A.; Medina, V. (2017). Tsunamis generated by fast granular landslides: 3D experiments and empirical predictors. *Journal of Hydraulic Research*, 55(6): 743–758. http://dx.doi.org/10.1080/00221686.2017.1289259.

Buckingham, E. (1914). On Physically Similar Systems; Illustrations of the Use of Dimensional Equations. *Physical Review*, 4(4): 345–376. http://dx.doi.org/10.1103/physrev.4.345.

Canassy, P Dalban; Bauder, A; Dost, M; Fäh, R; Funk, M; Margreth, S; Müller, B; Sugiyama, S (2011). Hazard assessment investigations due to recent changes in Triftgletscher, Bernese Alps, Switzerland. *Natural Hazards and Earth System Sciences*, 11(8): 2149. http://dx.doi.org/10.5194/nhess-11-2149-2011.

Carey, M. (2008). Chap. Disasters, Development, and Glacial Lake Control in Twentieth-Century Peru: 181–196. In: E. Wiegandt (ed.) Mountains: Sources of Water, Sources of Knowledge. *Springer Netherlands*. http://dx.doi.org/10.1007/978-1-4020-6748-8_11.

Chadwick, A.; Morfett, J.; Borthwick, M. (2013). Hydraulics in Civil and Environmental Engineering. *Taylor & Francis Ltd*. http://dx.doi.org/10.4324/9780203235454.

Chaudhry, M. H.; Mercer, A. G.; Cass, D. (1983). Modeling of Slide-Generated Waves in a Reservoir. *Journal of Hydraulic Engineering*, 109(11): 1505–1520. http://dx.doi.org/10.1061/(asce)0733-9429(1983)109:11(1505).

Chen, Y. Y.; Kharif, C.; Yang, J. H.; Hsu, H. C.; Touboul, J.; Chambarel, J. (2015). An experimental study of steep solitary wave reflection at a vertical wall. *European Journal of Mechanics - B/Fluids*, 49: 20–28. http://dx.doi.org/10.1016/j.euromechflu.2014.07.003.

Clague, J. J.; Evans, S. G. (2000). A review of catastrophic drainage of moraine-dammed lakes in British Columbia. *Quaternary Science Reviews*, 19(17-18): 1763–1783. http://dx.doi.org/10.1016/s0277-3791(00)00090-1.

Cobelli, P. J.; Maurel, A.; Pagneux, V.; Petitjeans, P. (2009). Global measurement of water waves by Fourier transform profilometry. *Experiments in Fluids*, 46(6): 1037–1047. http://dx.doi.org/10.1007/s00348-009-0611-z.

Collins, B. D.; Jibson, R. W. (2015). Assessment of existing and potential landslide hazards resulting from the April 25, 2015 Gorkha, Nepal earthquake sequence. USGS Report 2015-1142. http://dx.doi.org/10.3133/ofr20151142.

Crosta, G. B.; Imposimato, S.; Roddeman, D. G. (2003). Numerical modelling of large landslides stability and runout. *Natural Hazards and Earth System Science*, 3(6): 523–538. http://dx.doi.org/10.5194/nhess-3-523-2003.

Dahl-Jensen, T.; Larsen, L. M.; Pedersen, S. A. S.; Pedersen, J.; Jepsen, H. F.; Pedersen, G.; Nielsen, T.; Pedersen, A. K.; von Platen-Hallermund, F.; Weng, W. (2004). Landslide and Tsunami 21 November 2000 in Paatuut, West Greenland. *Natural Hazards*, 31(1): 277–287. http://dx.doi.org/10.1023/B:NHAZ.0000020264.70048.95.

Davidson, D. D.; McCartney, B. L. (1975). Water waves generated by landslides in reservoirs. *Journal of the Hydraulics Division*, 101(12): 1489–1501.

Dean, R. G.; Dalrymple, R. A. (1991). Water Wave Mechanics for Engineers and Scientists. *World Scientific Publishing Company*. http://dx.doi.org/10.1142/9789812385512.

Di Risio, M.; De Girolamo, P.; Bellotti, G.; Panizzo, A.; Aristodemo, F.; Molfetta, M. G.; Petrillo, A. F. (2009). Landslide-generated tsunamis runup at the coast of a conical island: New physical model experiments. *Journal of Geophysical Research*, 114(C1). http://dx.doi.org/10.1029/2008jc004858.

Di Risio, M.; De Girolamo, P.; Beltrani, G. M. (2011). Chap. Forecasting Landslide Generated Tsunamis: a Review: 81–106. In: N.-A. Mörner (ed.) The Tsunami Threat - Research and Technology. *InTech*. http://dx.doi.org/10.5772/13767.

Erismann, T. H.; Abele, G. (2001). Dynamics of Rockslides and Rockfalls. *Springer Nature*. http://dx.doi.org/10.1007/978-3-662-04639-5.

Evans, S. G. (1989). The 1946 Mount Colonel Foster rock avalanche and associated displacement wave, Vancouver Island, British Columbia. *Canadian Geotechnical Journal*, 26(3): 447–452. http://dx.doi.org/10.1139/t89-057.

Evers, F. M. (2017). Spatial impulse wave. Zenodo. http://dx.doi.org/10.5281/zenodo.580446.

Evers, F. M. (2018). Hydraulic scale model experiments on spatial propagation of landslide generated impulse waves. Zenodo. http://dx.doi.org/10.5281/zenodo.1069078.

Evers, F. M.; Hager, W. H. (2015a). Impulse Wave Generation: Comparison of Free Granular with Mesh-Packed Slides. *Journal of Marine Science and Engineering*, 3(1): 100–110. http://dx.doi.org/10.3390/jmse3010100.

Evers, F. M.; Hager, W. H. (2015b). Videometric water surface tracking: towards investigating spatial impulse waves. *Proc. 36th IAHR World Congress*. http://dx.doi.org/10.3929/ethz-a-010630706.

Evers, F. M.; Hager, W. H. (2016a). Generation and spatial propagation of landslide generated impulse wave. *Proc. Coastal Engineering 2016. American Society of Civil Engineers*. http://dx.doi.org/10.9753/icce.v35.currents.13.

Evers, F. M.; Hager, W. H. (2016b). Spatial impulse waves: wave height decay experiments at laboratory scale. *Landslides*, 13(6): 1395–1403. http://dx.doi.org/10.1007/s10346-016-0719-1.

Frank, P.-J. (2016). Hydraulics of Spatial Dike Breaches. *VAW-Mitteilung 236* (R. Boes, ed.). Zurich, Switzerland.

Frank, P.-J.; Hager, W. H. (2014). Spatial dike breach: Accuracy of photogrammetric measurement system. *Proc. Proceedings River Flow 2014*. http://dx.doi.org/10.1201/b17133-219.

Fritz, H. M. (2002). Initial phase of landslide generated impulse waves. *VAW-Mitteilung 178* (H.-E. Minor, ed.). Zurich, Switzerland.

Fritz, H. M.; Hager, W. H.; Minor, H.-E. (2003). Landslide generated impulse waves. 2. Hydrodynamic impact craters. *Experiments in Fluids*, 35(6): 520–532. http://dx.doi.org/10.1007/s00348-003-0660-7.

Fritz, H. M.; Moser, P. (2003). Pneumatic Landslide Generator. *International Journal of Fluid Power*, 4(1): 49–57. http://dx.doi.org/10.1080/14399776.2003.10781155.

Fuchs, H. (2013). Solitary impulse wave run-up and overland flow. *VAW-Mitteilung 221* (R.M. Boes, ed.). Zurich, Switzerland.

Fuchs, H.; Boes, R. (2010). Berechnung felsrutschinduzierter Impulswellen im Vierwaldstättersee ('Computation of rock slide-induced impulse waves in Lake Lucerne'). *Wasser Energie Luft*, 102(3): 215–221 (in German).

Fuchs, H.; Boes, R. M.; Pfister, M. (2011). Impulse waves at Kühtai reservoir generated by avalanches and landslides. *Proc. Dams and Reservoirs under Changing Challenges. CRC Press (A.S. Schleiss; R.M. Boes, eds.)*: 701–708. http://dx.doi.org/10.1201/b11669-88.

Fuchs, H.; Hager, W. H. (2015). Solitary Impulse Wave Transformation to Overland Flow. *Journal of Waterway, Port, Coastal, and Ocean Engineering*, 141(5): 04015004. http://dx.doi.org/10.1061/(asce)ww.1943-5460.0000294.

Genevois, R.; Ghirotti, M. (2005). The 1963 Vaiont Landslide. *Giornale di Geologia Applicata*, (1): 41–52. http://dx.doi.org/10.1474/GGA.2005-01.0-05.0005.

Gylfadóttir, S. S.; Kim, J.; Helgason, J. K.; Brynjólfsson, S.; Höskuldsson, Á.; Jóhannesson, T.; Harbitz, C. B.; Løvholt, F. (2017). The 2014 Lake Askja rockslide-induced tsunami: Optimization of numerical tsunami model using observed data. *Journal of Geophysical Research: Oceans*. http://dx.doi.org/10.1002/2016jc012496.

Hafsteinsson, H. J.; Evers, F. M.; Hager, W. H. (2017). Solitary wave run-up: wave breaking and bore propagation. *Journal of Hydraulic Research*, 55(6): 787–798. http://dx.doi.org/10.1080/00221686.2017.1356756.

Heller, V. (2008). Landslide generated impulse waves: Prediction of near field characteristics. *VAW-Mitteilung 204* (H.-E. Minor, ed.). Zurich, Switzerland.

Heller, V. (2011). Scale effects in physical hydraulic engineering models. *Journal of Hydraulic Research*, 49(3): 293–306. http://dx.doi.org/10.1080/00221686.2011.578914.

Heller, V.; Hager, W. H. (2010). Impulse Product Parameter in Landslide Generated Impulse Waves. *Journal of Waterway, Port, Coastal, and Ocean Engineering*, 136(3): 145–155. http://dx.doi.org/10.1061/(asce)ww.1943-5460.0000037.

Heller, V.; Hager, W. H. (2011). Wave types of landslide generated impulse waves. *Ocean Engineering*, 38(4): 630–640. http://dx.doi.org/10.1016/j.oceaneng.2010.12.010.

Heller, V.; Hager, W. H.; Minor, H.-E. (2008). Scale effects in subaerial landslide generated impulse waves. *Experiments in Fluids*, 44(5): 691–703. http://dx.doi.org/10.1007/s00348-007-0427-7.

Heller, V.; Hager, W. H.; Minor, H.-E. (2009). Landslide generated impulse waves in reservoirs: Basics and computation. *VAW-Mitteilung 211* (R. Boes, ed.). Zurich, Switzerland.

Heller, V.; Moalemi, M.; Kinnear, R. D.; Adams, R. A. (2012). Geometrical Effects on Landslide-Generated Tsunamis. *Journal of Waterway, Port, Coastal, and Ocean Engineering*, 138(4): 286–298. http://dx.doi.org/10.1061/(ASCE)WW.1943-5460.0000130.

Heller, V.; Spinneken, J. (2013). Improved landslide-tsunami prediction: Effects of block model parameters and slide model. *Journal of Geophysical Research: Oceans*, 118(3): 1489–1507. http://dx.doi.org/10.1002/jgrc.20099.

Heller, V.; Spinneken, J. (2015). On the effect of the water body geometry on landslide–tsunamis: Physical insight from laboratory tests and 2D to 3D wave parameter transformation. *Coastal Engineering*, 104: 113–134. http://dx.doi.org/10.1016/j.coastaleng.2015.06.006.

Huang, B.; Yin, Y.; Liu, G.; Wang, S.; Chen, X.; Huo, Z. (2012). Analysis of waves generated by Gongjiafang landslide in Wu Gorge, three Gorges reservoir, on November 23, 2008. *Landslides*, 9(3): 395–405. http://dx.doi.org/10.1007/s10346-012-0331-y.

Huang, B.; Yin, Y.; Wang, S.; Chen, X.; Liu, G.; Jiang, Z.; Liu, J. (2014). A physical similarity model of an impulsive wave generated by Gongjiafang landslide in Three Gorges Reservoir, China. *Landslides*, 11(3): 513–525. http://dx.doi.org/10.1007/s10346-013-0453-x.

Huang, B.; Yueping, Y.; Xiaoting, C.; Guangning, L.; Sichang, W.; Zhibing, J. (2013). Experimental modeling of tsunamis generated by subaerial landslides: two case studies of the Three Gorges Reservoir, China. *Environmental Earth Sciences*, 71(9): 3813–3825. http://dx.doi.org/10.1007/s12665-013-2765-5.

Huber, A. (1980). Schwallwellen in Seen als Folge von Felsstürzen ('Impulse waves in lakes resulting from rockfalls'). *VAW-Mitteilung 47* (D. Vischer, ed.). Zurich, Switzerland (in German).

Huber, A. (1982). Felsbewegungen und Uferabbrüche an Schweizer Seen, ihre Ursachen und Auswirkungen ('Rock movements and bank break-offs at Swiss lakes, their causes and effects'). *Eclogae Geol. Helv.*, 75(3): 563–578 (in German).

Huber, A.; Hager, W.H. (1997). Forecasting impulse waves in reservoirs. *Proc. 19th Congrès des Grands Barrages, Florence,*. ICOLD, Paris: 993–1005.

Huber, L. E.; Evers, F. M.; Hager, W. H. (2017). Solitary wave overtopping at granular dams. *Journal of Hydraulic Research*, 55(6): 799–812. http://dx.doi.org/10.1080/00221686.2017.1356757.

Hughes, S. A. (1993). Physical Models and Laboratory Technique. *Advanced Series on Ocean Engineering 7* (P. L. F. Liu, ed.). World Scientific Publishing, Singapore. http://dx.doi.org/10.1142/9789812795939.

Hungr, O.; Leroueil, S.; Picarelli, L. (2013). The Varnes classification of landslide types, an update. *Landslides*, 11(2): 167–194. http://dx.doi.org/10.1007/s10346-013-0436-y.

Johnson, J. W.; Bermel, K. J. (1949). Impulsive waves in shallow water as generated by falling weights. *Transactions, American Geophysical Union*, 30(2): 223. http://dx.doi.org/10.1029/tr030i002p00223.

Kamphuis, J. W.; Bowering, R. J. (1970). Impulse Waves Generated by Landslides. *Proc. Coastal Engineering 1970. American Society of Civil Engineers (ASCE)*. http://dx.doi.org/10.1061/9780872620285.035.

Klimeš, J.; Novotný, J.; Novotná, I.; de Urries, B. Jordán; Vilímek, V.; Emmer, A.; Strozzi, T.; Kusák, M.; Rapre, A. Cochachin; Hartvich, F.; Frey, H. (2016). Landslides in moraines as triggers of glacial lake outburst floods: example from Palcacocha Lake (Cordillera Blanca, Peru). *Landslides*, 13(6): 1461–1477. http://dx.doi.org/10.1007/s10346-016-0724-4.

Kobel, J.; Evers, F. M.; Hager, W. H. (2017). Impulse Wave Overtopping at Rigid Dam Structures. *Journal of Hydraulic Engineering*: 04017002. http://dx.doi.org/10.1061/(asce)hy.1943-7900.0001271.

Kobus, H.; Koschitzky, H.-P. (1991). Chap. Local surface aeration at hydraulic structures: 29–53. In: Ian R. Wood (ed.) Air entrainment in free-surface flows. *Balkema*. http://dx.doi.org/10.18419/opus-551.

Lindstrøm, E. K. (2016). Waves generated by subaerial slides with various porosities. *Coastal Engineering*, 116: 170–179. http://dx.doi.org/10.1016/j.coastaleng.2016.07.001.

Lindstrøm, E. K.; Pedersen, G. K.; Jensen, A.; Glimsdal, S. (2014). Experiments on slide generated waves in a 1:500 scale fjord model. *Coastal Engineering*, 92: 12–23. http://dx.doi.org/10.1016/j.coastaleng.2014.06.010.

Loew, S.; Gschwind, S.; Gischig, V.; Keller-Signer, A.; Valenti, G. (2017). Monitoring and early warning of the 2012 Preonzo catastrophic rockslope failure. *Landslides*, 14(1): 141–154. http://dx.doi.org/10.1007/s10346-016-0701-y.

Lynett, P. J.; Weiss, R.; Mattox, A.; Skanavis, V.; Ayca, A.; Tang, H.; Higman, B. M.; Stark, C. P.; Keen, A. (2016). The Tsunami Generated by the October 17th, 2015 Taan Fjord landslide. *Proc. Abstract NH51D-05 presented at 2016 Fall Meeting. AGU, San Francisco, Calif., 11-15 Dec.*.

Miller, D. J. (1960). The Alaska earthquake of July 10, 1958: giant wave in Lituya Bay. *Bulletin of the Seismological Society of America*, 50(2): 253–266.

Miller, G. S.; Take, W. A.; Mulligan, R. P.; McDougall, S. (2017). Tsunamis generated by long and thin granular landslides in a large flume. *Journal of Geophysical Research: Oceans*, 122(1): 653–668. http://dx.doi.org/10.1002/2016jc012177.

Miller, R. L (1970). Prediction Curves for Waves Near the Source of an Impulse. *Proc. Coastal Engineering 1970. American Society of Civil Engineers*. http://dx.doi.org/10.1061/9780872620285.037.

Mohammed, F.; Fritz, H. M. (2012). Physical modeling of tsunamis generated by three-dimensional deformable granular landslides. *Journal of Geophysical Research: Oceans*, 117(C11): 1–20. http://dx.doi.org/10.1029/2011jc007850.

Müller, D. R. (1995). Auflaufen und Überschwappen von Impulswellen an Talsperren ('Run-up and overtopping of impulse waves at dams'). *VAW-Mitteilung 137* (D. Vischer, ed.). Zurich, Switzerland (in German).

Noda, E. (1970). Water waves generated by landslides. *Journal of the Waterways, Harbors and Coastal Engineering Division*, 96(4): 835–855.

Novak, P.; Guinot, V.; Jeffrey, A.; Reeve, D. E. (2010). Hydraulic Modelling - An Introduction: Principles, Methods and Applications. *CRC PR INC*. http://dx.doi.org/10.1080/00221686.2010.492104.

Panizzo, A.; De Girolamo, P.; Petaccia, A. (2005). Forecasting impulse waves generated by subaerial landslides. *Journal of Geophysical Research*, 110(C12). http://dx.doi.org/10.1029/2004jc002778.

Plafker, G.; Eyzaguirre, V. R. (1979). Rock Avalanche and Wave at Chungar, Peru. *Developments in Geotechnical Engineering 14B* (B. Voight, ed.). 269–279. http://dx.doi.org/10.1016/b978-0-444-41508-0.50015-6.

Pougatsch, H.; Ammann, E.; Hauenstein, W.; Loosli, D.; Mouvet, L.; Müller, R. W.; Rechsteiner, G. (2002). Sicherheit der Stauanlagen. Basisdokument zur konstruktiven Sicherheit [Dam safety. Base document on structural safety]. Federal Office for Water and Geology, Biel, Switzerland (in German).

Przadka, A.; Cabane, B.; Pagneux, V.; Maurel, A.; Petitjeans, P. (2012). Fourier transform profilometry for water waves: how to achieve clean water attenuation with diffusive reflection at the water surface? *Experiments in Fluids*, 52(2): 519–527. http://dx.doi.org/10.1007/s00348-011-1240-x.

Pujara, N.; Liu, P. L.-F.; Yeh, H. (2015). The swash of solitary waves on a plane beach: flow evolution, bed shear stress and run-up. *Journal of Fluid Mechanics*, 779: 556–597. http://dx.doi.org/10.1017/jfm.2015.435.

Ramsden, J. D. (1996). Forces on a Vertical Wall due to Long Waves, Bores, and Dry-Bed Surges. *Journal of Waterway, Port, Coastal, and Ocean Engineering*, 122(3): 134–141. http://dx.doi.org/10.1061/(asce)0733-950x(1996)122:3(134).

Roberts, N. J.; McKillop, R.; Hermanns, R. L.; Clague, J. J.; Oppikofer, T. (2014). Preliminary Global Catalogue of Displacement Waves from Subaerial Landslides. *Landslide Science for a Safer Geoenvironment 3* (K. Sassa; P. Canuti; Y. Yin, eds.). 687–692. http://dx.doi.org/10.1007/978-3-319-04996-0_104.

Roberts, N. J.; McKillop, R. J.; Lawrence, M. S.; Psutka, J. F.; Clague, J. J.; Brideau, M.-A.; Ward, B. C. (2013). Impacts of the 2007 Landslide-Generated Tsunami in Chehalis Lake, Canada. *Landslide Science and Practice 6* (C. Margottini; P. Canuti; K. Sassa, eds.). 133–140. http://dx.doi.org/10.1007/978-3-642-31319-6_19.

Romano, A.; Di Risio, M.; Bellotti, G.; Molfetta, M. G.; Damiani, L.; De Girolamo, P. (2016). Tsunamis generated by landslides at the coast of conical islands: experimental benchmark dataset for mathematical model validation. *Landslides*, 13(6): 1379–1393. http://dx.doi.org/10.1007/s10346-016-0696-4.

Russell, J. S. (1844). Report on waves. Report of the Fourteenth Meeting of the British Association for the Advancement of Science. *Richard and John E. Taylor*.

Sælevik, G.; Jensen, A.; Pedersen, G. (2009). Experimental investigation of impact generated tsunami: related to a potential rock slide, Western Norway. *Coastal Engineering*, 56(9): 897–906. http://dx.doi.org/10.1016/j.coastaleng.2009.04.007.

Sander, J. (1990). Weakly nonlinear unidirectional shallow water waves generated by a moving boundary. *VAW-Mitteilung 105* (D. Vischer, ed.). Zurich, Switzerland.

Sepúlveda, S. A.; Serey, A.; Lara, M.; Pavez, A.; Rebolledo, S. (2010). Landslides induced by the April 2007 Aysén Fjord earthquake, Chilean Patagonia. *Landslides*, 7(4): 483–492. http://dx.doi.org/10.1007/s10346-010-0203-2.

Slingerland, R. L.; Voight, B. (1979). Occurrences, Properties, and Predictive Models of Landslide-Generated Water Waves. *Developments in Geotechnical Engineering 14B*

(B. Voight, ed.). 317–394. http://dx.doi.org/10.1016/b978-0-444-41508-0.50017-x.

Su, C. H.; Mirie, R. M. (1980). On head-on collisions between two solitary waves. *Journal of Fluid Mechanics*, 98(03): 509–525. http://dx.doi.org/10.1017/s0022112080000262.

Synolakis, C. E. (1987). The runup of solitary waves. *Journal of Fluid Mechanics*, 185: 523–545. http://dx.doi.org/10.1017/s002211208700329x.

Synolakis, C. E. (1989). Are Solitary Waves the Limiting Waves in Long Wave Runup? *Proc. Coastal Engineering 1988. American Society of Civil Engineers*. http://dx.doi.org/10.1061/9780872626874.015.

Tsubaki, R.; Fujita, I. (2005). Stereoscopic measurement of a fluctuating free surface with discontinuities. *Measurement Science and Technology*, 16(10): 1894–1902. http://dx.doi.org/10.1088/0957-0233/16/10/003.

VAW (1972). Stausee Mauvosin ('Lac de Mauvoisin'). *Technical Report 601*, Laboratory of Hydraulics, Hydrology and Glaciology (VAW), ETH Zurich (in German).

VAW (1973). Ausgleichsbecken Ferden ('Ferden compensating basin'). *Technical Report 621*, Laboratory of Hydraulics, Hydrology and Glaciology (VAW), ETH Zurich (in German).

VAW (1974). Felssturz bei Amden ('Rock fall near Amden'). *Technical Report 627*, Laboratory of Hydraulics, Hydrology and Glaciology (VAW), ETH Zurich (in German).

Viroulet, S.; Sauret, A.; Kimmoun, O. (2014). Tsunami generated by a granular collapse down a rough inclined plane. *EPL (Europhysics Letters)*, 105(3): 34004. http://dx.doi.org/10.1209/0295-5075/105/34004.

Volkart, P. (1974). Modellversuche über die durch Lawinen verursachten Wellenbewegungen im Ausgleichbecken Ferden im Lötschental ('Model tests on the wave movements caused by avalanches in the Ferden compensation basin in the Lötschental'). *Wasser- und Energiewirtschaft*, 66(8/9): 286–292 (in German).

Vuichard, D.; Zimmermann, M. (1987). The 1985 Catastrophic Drainage of a Moraine-Dammed Lake, Khumbu Himal, Nepal: Cause and Consequences. *Mountain Research and Development*, 7(2): 91–110. http://dx.doi.org/10.2307/3673305.

Walder, J. S.; Watts, P.; Sorensen, O. E.; Janssen, K. (2003). Tsunamis generated by subaerial mass flows. *Journal of Geophysical Research: Solid Earth*, 108(B5). http://dx.doi.org/10.1029/2001jb000707.

Walters, R. C. S. (1971). Dam geology. *Butterworth*.

Wang, J.; Ward, S. N.; Xiao, L. (2015). Numerical simulation of the December 4, 2007 landslide-generated tsunami in Chehalis Lake, Canada. *Geophysical Journal International*, 201(1): 372–376. http://dx.doi.org/10.1093/gji/ggv026.

Yavari-Ramshe, S.; Ataie-Ashtiani, B. (2016). Numerical modeling of subaerial and submarine landslide-generated tsunami waves—recent advances and future challenges. *Landslides*, 13(6): 1325–1368. http://dx.doi.org/10.1007/s10346-016-0734-2.

Zweifel, A. (2004). Impulswellen: Effekte der Rutschdichte und der Wassertiefe ('Impulse waves: Effects of slide density and water depth'). *VAW-Mitteilung 186* (H.-E. Minor, ed.). Zurich, Switzerland (in German).

Zweifel, A.; Hager, W. H.; Minor, H.-E. (2006). Plane Impulse Waves in Reservoirs. *Journal of Waterway, Port, Coastal, and Ocean Engineering*, 132(5): 358–368. http://dx.doi.org/10.1061/(asce)0733-950x(2006)132:5(358).

Notation

Roman Symbols

A_M	Relative maximum wave amplitude (2D)	[-]
a_M	Maximum wave amplitude (2D)	[m]
$A_{0,c1}$	Relative initial first wave crest amplitude	[-]
$a_{0,c1}$	Initial first wave crest amplitude	[m]
$A_{0,c2}$	Relative initial second wave crest amplitude	[-]
$a_{0,c2}$	Initial second wave crest amplitude	[m]
$A_{0,t1}$	Relative initial first wave trough amplitude	[-]
$a_{0,t1}$	Initial first wave trough amplitude	[m]
A_{2D}	Relative wave amplitude (2D)	[-]
a_{2D}	Wave amplitude (2D)	[-]
A_{c1}	Relative first wave crest amplitude	[-]
a_{c1}	First wave crest amplitude	[m]
A_{c2}	Relative second wave crest amplitude	[-]
a_{c2}	Second wave crest amplitude	[m]
a_m	Mean wave amplitude (2D)	[m]
A_{t1}	Relative first wave trough amplitude	[-]
a_{t1}	First wave trough amplitude	[m]
A_w^*	Dimensionless slide front surface	[-]
b	Slide width	[m]
c	Celerity of shallow-water waves $c = \sqrt{gh}$	[m/s]
C	Cauchy number	[-]
c_{am}	Mean wave celerity (2D)	[m]
c_{c1}	First wave crest celerity	[m/s]
c_{c2}	Second wave crest celerity	[m/s]
D	Relative bulk slide density	[-]
d_g	Grain diameter	[mm]
F	Force	[kg m/s^2]

f	Slide release box form	
F	Slide Froude number	[-]
F_f	Slide front Froude number	[-]
F	Function F	[-]
f	Function f	[-]
f_γ	3D angle decay function	[-]
g	Gravitational acceleration	[m/s^2]
h	Still water depth	[m]
H_1	First wave height	[m]
H_M	Maximum wave height (2D)	[m]
$H_{2\mathrm{D}}$	Wave height (2D)	[-]
i	Number of dimensionless quantities	[-]
k	Number of fundamental dimensions	[-]
k_{ac1}	First wave crest generation function	[-]
k_{ac2}	Second wave crest generation function	[-]
k_{at1}	First wave trough generation function	[-]
L	Length	[m]
L	Length dimension	[m]
l_s	Slide length	[m]
M	Relative slide mass	[-]
M	Mass dimension	[kg]
m_s	Slide mass	[kg]
n	Number of quantities/entities	[-]
n_{ac1}	First wave crest decay function	[-]
n_{ac2}	Second wave crest decay function	[-]
n_{at1}	First wave trough decay function	[-]
P	Impulse product parameter	[-]
Q	Quantity	
R	Runup height	[m]
r	Radial wave propagation distance	[m]

R	Reynolds number	[-]
R^*	Relative surrogate radial wave propagation distance	[-]
r^*	Surrogate radial wave propagation distance	[m]
R^2	Coefficient of determination	[-]
R_0	Relative impact radius	[-]
r_0	Impact radius	[m]
S	Relative slide thickness	[-]
s	Slide thickness	[m]
T	Relative time	[-]
t	Time	[s]
T	Time dimension	[s]
T_1	First wave period	[s]
t_r	Residence time of a solitary wave at a vertical wall	[s]
t_s	Time of the landslide underwater motion	[-]
t_s^*	Dimensionless time of the landslide underwater motion	[-]
U	Velocity	[m/s]
V	Relative bulk slide volume	[-]
$\cancel{V}_s$	Bulk slide volume	[m^3]
V_f	Slide front velocity	[m/s]
V_s	Slide centroid velocity	[m/s]
W	Weber number	[-]
X	Relative streamwise distance (2D)	[-]
x	x-coordinate	[m]
X_M	Relative streamwise distance of maximum wave amplitude a_M (2D)	[-]
x_M	Streamwise distance of maximum wave amplitude a_M (2D)	[m]
y	y-coordinate	[m]
Y_1	Relative first wave height	[-]
Y_M	Relative maximum wave height (2D)	[-]
Y_{2D}	Relative wave height (2D)	[-]
z	z-coordinate	[m]

Greek Symbols

α	Slide impact angle	[°]
α_{eff}	Effective slide impact angle, $\alpha_{\text{eff}} = (6/7)\alpha$	[°]
β	Wave runup angle	[°]
Δx	Spacing between two adjacent CWG	[m]
Δx_1	Spacing between CWG_1 and impounded sliding plane	[m]
ε	Relative wave amplitude	[-]
η	Water surface displacement	[m]
γ	Wave propagation angle	[°]
κ_w	Water compressibility	$[\text{m}^2/\text{N}]$
λ	Ratio	[-]
ν_w	Kinematic fluid viscosity of water	$[\text{m}^2/\text{s}]$
ρ_g	Grain density	$[\text{kg}/\text{m}^3]$
ρ_s	Bulk slide density	$[\text{kg}/\text{m}^3]$
ρ_w	Water density	$[\text{kg}/\text{m}^3]$
σ_w	Water surface tension	[N/s]
θ	Basin side angle	[°]
τ	Dimensionless time	[-]
Π	Dimensionless quantity	[-]
υ	Exponent variable	[-]
φ	Exponent variable	[-]
ω	Exponent variable	[-]

Subscripts

0°	Wave propagation angle $\gamma = 0°$
90°	Wave propagation angle $\gamma = 90°$
F	Force
G	General
g	Grain
L	Length
M	Model scale

P	Prototype scale
U	Velocity
meas	Measured
pred	Predicted

Abbreviations

2D	Two-dimensional
3D	Three-dimensional
$BaSO_4$	Barium sulfate
CWG	Capacitance Wave Gauge
DI	Deionized
ETH	Eidgenössische Technische Hochschule (Swiss Federal Institute of Technology)
LDS	Laser Distance Sensor
LLB	Laser Light Barrier
PIV	Particle Image Velocimetry
PP	Polypropylene
PVC	PolyVinyl Chloride
SPH	Smoothed-particle hydrodynamics
SWL	Still water level
TiO_2	Titanium dioxide
VAW	Versuchsanstalt für Wasserbau, Hydrologie und Glaziologie (Laboratory of Hydraulics, Hydrology and Glaciology)